

AD-A268 269

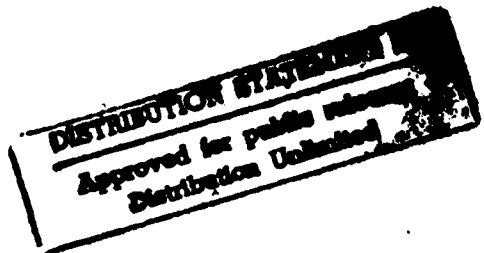


Semi-Annual Report

Interface Properties of Wide Bandgap Semiconductor Structures

Office of Naval Research
Supported under Grant #N00014-92-J-1477
Report for the period 1/1/93-6/30/93

Robert F. Davis, Salah Bedair,* Jerry Bernholc,**
Jeffrey T. Glass and R. J. Nemanich**
c/o Materials Science and Engineering Department
*Electrical and Computer Engineering Department
and **Department of Physics
North Carolina State University
Campus Box 7907
Raleigh, NC 27695-7907



June, 1993

DTIC
SELECTED
AUG 16 1993
S B D

93-18820

93 8 13 070



REPORT DOCUMENTATION PAGE

*Form Approved
OMB No. 0704-0188*

Public reporting burden for this collection of information is estimated to average 1 hour per response, including the time for reviewing instructions, searching existing data sources, gathering and maintaining the data needed, and completing and reviewing the collection of information. Send comments regarding this burden estimate or any other aspect of this collection of information, including suggestions for reducing this burden, to Washington Headquarters Services, Directorate for Information Operations and Reports, 1215 Jefferson Davis Highway, Suite 1204, Arlington, VA 22202-4302, and to the Office of Management and Budget Paperwork Reduction Project (0704-0188), Washington, DC 20503.

1. AGENCY USE ONLY (Leave blank)			2. REPORT DATE		3. REPORT TYPE AND DATES COVERED		
			June, 1993		Semi-Annual 1/1/93-6/30/93		
4. TITLE AND SUBTITLE			5. FUNDING NUMBERS				
Interface Properties of Wide Bandgap Semiconductor Structures			uri41114a-01 1114SS N00179 N66005 4B855				
6. AUTHOR(S)							
Robert F. Davis and R. J. Nemanich							
7. PERFORMING ORGANIZATION NAME(S) AND ADDRESS(ES)			8. PERFORMING ORGANIZATION REPORT NUMBER				
North Carolina State University Hillsborough Street Raleigh, NC 27695			N00014-92-J-1477				
9. SPONSORING/MONITORING AGENCY NAMES(S) AND ADDRESS(ES)			10. SPONSORING/MONITORING AGENCY REPORT NUMBER				
Sponsoring: ONR, 800 N. Quincy, Arlington, VA 22217-5000 Monitoring: Office of Naval Research Resider The Ohio State University Research Center 1960 Kenny Road Columbus, OH 43210-1063							
11. SUPPLEMENTARY NOTES							
12a. DISTRIBUTION/AVAILABILITY STATEMENT			12b. DISTRIBUTION CODE				
Approved for Public Release; Distribution Unlimited							
13. ABSTRACT (Maximum 200 words)							
Theoretical studies have involved calculations of the electronic states of hydrogenated surfaces and the properties of defect and impurities in GaN. Infrared studies on diamond films have indicated SiC at the interface and the lack of C-H bonding in the films. To investigate SiC growth, two chambers have been integrated into the surface science facility. Studies of the interdiffusion of SiC-AlN have indicated new results concerning SiC-AlN phase diagrams. The use of ALE for SiC deposited on patterned substrates has been initiated. Low temperature (LT) GaP and InGaP films produced by gas source MBE proved the first demonstration of high resistivity, semi-insulating properties. Using an ALE reactor, layer-by-layer growth of GaN has been demonstrated. The CVD deposition of AlN nitride has been demonstrated on various substrates. A combined photo/cathodo-luminescence system is being assembled. The effects of hydrogen and oxygen on the Schottky barrier of Ni/diamond has been studied, and negative electron affinity effects are observed. The Schottky barrier properties of various metals on clean n-type 6H-SiC have been measured. Approaches have been developed for contacts on GaN and AlN. A reactive ion etching system has been configured for patterning of GaN and AlN films.							
14. SUBJECT TERMS					15. NUMBER OF PAGES		
molecular dynamics, thin films, diamond surface, atomic layer epitaxy, AlN, GaN, SiC, oxy-acetylene torch, MBE, pseudomorphic heterostructures, Schottky contacts, SiGe alloys					131		
					16. PRICE CODE		
17. SECURITY CLASSIFICATION OF REPORT		18. SECURITY CLASSIFICATION OF THIS PAGE		19. SECURITY CLASSIFICATION OF ABSTRACT		20. LIMITATION OF ABSTRACT	
UNCLAS		UNCLAS		UNCLAS		SAR	

Table of Contents

I. Introduction	1
Theoretical Studies	
II. Theoretical Studies of Wide Bandgap Materials <i>(J. Bernholc)</i>	3
Thin Film Growth and Characterization of Carbon-based Materials	
III. Infrared Investigations of Diamond Thin Films <i>(P. W. Morrison, Jr., D. A. Tucker, and J. T. Glass)</i>	13
IV. Characterization of 6H-SiC Surface by RHEED and HRTEM <i>(S. Tanaka and R. F. Davis)</i>	24
V. Integrated Surface Science System for Studies of the ALE of SiC <i>(S. King and R. F. Davis)</i>	30
Thin Film Growth and Characterization of Solid Solutions and Multilayer Heterostructures from Silicon Carbide and III-V Nitrides	
VI. Determination of the Diffusivity of Si, C, Al and N at the Interface of the SiC-AlN Diffusion Couple <i>(R. Patterson and R. F. Davis)</i>	35
VII. Interface Properties of Wide Bandgap Semiconductor Structures <i>(J. J. Sumakeris and R. F. Davis)</i>	44
Thin Film Growth and Characterization of III-V Materials	
VIII. High Resistivity LT GaP and InGaP Films Grown by Gas Source Molecular Beam Epitaxy (GSMBE) <i>(Y. He and S. Bedair)</i>	50
IX. Layer-by-Layer Deposition of III-V Nitrides Using an Atomic Layer Epitaxy Reactor Design <i>(W. Weeks and R. F. Davis)</i>	65
X. Deposition of Aluminum Nitride Films Via Decomposition of $\text{AlCl}_3 \times \text{NH}_3$ Complex <i>(C. Balkas and R. F. Davis)</i>	73
XI. Development of a Combined Photo- and Cathodo-Luminescence System for Characterization of Wide Bandgap Semiconductor Thin Films <i>(W. Perry and R. F. Davis)</i>	81
Metal Contacts	
XII. The Influence of Interfacial Hydrogen and Oxygen on the Schottky Barrier of Nickel on (111) and (100) Diamond Surfaces <i>(J. van der Weide and R. J. Nemanich)</i>	84
XIII. Ohmic and Schottky Contacts to n-type Alpha (6H) Silicon Carbide <i>(L. Porter and R. F. Davis)</i>	107
XIV. Contact Formation in GaN and AlN <i>(L. Smith and R. F. Davis)</i>	117
Etching and Patterning	
XV. Reactive Ion Etching of GaN and AlN <i>(K. Gruss and R. F. Davis)</i>	124
XVI. Distribution List	131

PTIC QUALITY INSPECTED 8

$$|A^{-1}|$$

I. Introduction

Heteroepitaxy is the growth of a crystal (or a film) on a foreign crystalline substrate that determines its orientation. Such oriented growth requires that lattice planes in both materials have similar structure. In general, an epitaxial relationship is probable whenever the orientation of the substrate and overgrowth produces an interface with a highly coincident atomic structure having low interfacial energy relative to a random arrangement.

During the past decade, non-equilibrium techniques have been developed for the growth of epitaxial semiconductors, superconductors, insulators and metals which have led to new classes of artificially-structured materials. In many cases, the films were deposited on substrates having a different chemistry from that of the film and heteroepitaxy was achieved. Moreover, layered structures with a periodicity of a few atomic layers have also been produced by the sequential heteroepitaxial deposition of a film of one type on another. Metastable structures can be generated which possess important properties not present in equilibrium systems. A consideration of the materials under consideration for next generation electronic and optoelectronic devices, e.g., the III-V nitrides show that only a few of them can currently be grown in bulk, single crystal form having a cross-sectional area of $>3\text{cm}^2$. Thus, other commercially available substrates must be used. This introduces a new set of challenges for the successful growth of device-quality films which are not present in homoepitaxial growth and which must be surmounted if these materials are to be utilized in device structures.

In addition to providing structures which do not exist in nature, applications of advanced heteroepitaxial techniques permit the growth of extremely high-quality heterostructures involving semiconductors, metals and insulators. These heterostructures offer the opportunity to study relationships between the atomic structure and the electrical properties of both the film itself and the interface between the two dissimilar materials. They also allow the study of epitaxial growth between materials exhibiting very different types of bonding (ionic, covalent, or metallic).

While the potential of heteroepitaxial deposition has been demonstrated, significant advances in theoretical understanding, experimental growth and control of this growth, and characterization are required to exploit the capabilities of this process route. It is particularly important to understand and control the principal processes which control heteroepitaxy at the atomic level. It is this type of research, as well as the chemistry of dry etching via laser and plasma processing, which forms the basis of the research in this grant.

The materials of concern in this grant are classified as wide bandgap semiconductors and include diamond, the III-V nitrides, SiC, GaP and AlP. The extremes in electronic and thermal properties of diamond and SiC allow the types and numbers of current and conceivable applications of these materials to be substantial. However, a principal driving

force for the interest in the III-V nitrides and GaP and AlP is their potential for solid-state optoelectronic devices for light emission and detection from the visible through the far ultraviolet range of the spectrum.

The principal objectives of this research program are the determination of (1) the fundamental physical and chemical processes ongoing at the substrate surface and substrate/film interface during the heteroepitaxial deposition of both monocrystalline films of the materials noted above as well as metal contacts on these materials, (2) the mode of nucleation and growth of the materials noted in (1) on selected substrates and on each other in the fabrication of multilayer heterostructures, (3) the resulting properties of the individual films and the layered structures and the effect of interfacial defects on these properties, (4) the development and use of theoretical concepts relevant to the research in objectives (1-3) to assist in the fabrication of improved films and structures and (5) the determination of process chemistry which leads to the laser-assisted and plasma etching of these wide bandgap compound semiconductors.

This is the second bi-annual report since the initiation of the project. The following sections introduce each topic, detail the experimental approaches, report the latest results and provide a discussion and conclusion for each subject. Each major section is self-contained with its own figures, tables and references.

II. Theoretical Studies of Wide Bandgap Materials

Study of Hydrogenated Diamond Surface Structures and Electron Affinity

A. Introduction

Diamond surfaces have received considerable attention in the last decade due to advances in thin film growth by chemical vapor deposition methods and the potential device applications [1]. Our recent research is concentrated on the structures and the properties of hydrogenated diamond surfaces.

B. Computational Methodology and Discussion of Results

Structure and Energetics of Hydrogenated Diamond Surfaces (100), (110), (111). We have studied the surfaces C(111):H, C(110):H, C(100)(1×1):2H, and C(100)(2×1):H using the LDA-pseudopotential method. These surfaces were modeled by slabs separated by a few angstroms of vacuum in the supercell scheme. Ground state geometry was obtained by using the steepest descents or fast-relaxationion method.

The calculations for the C(111):H and C(110):H surfaces were done using eight- and six-layer carbon slabs respectively and a 26 Rydberg plane-wave cutoff. Since all of the surface dangling bonds are saturated, no strong reconstruction results on these surfaces, see Figs. 1 and 2.

The (100) surface is a CVD epitaxial growth surface [3]. According to experimental results, a 1×1 LEED pattern appears when C(100) surface is heated from 500 to 700 K and at temperatures above 1300 K, a 2×1 LEED pattern is observed. It is believed that a 2×1 reconstructed monohydride or bare surface is responsible the 2×1 LEED pattern. While no consensus has been reached on the observed 1×1 LEED pattern, the surface has been

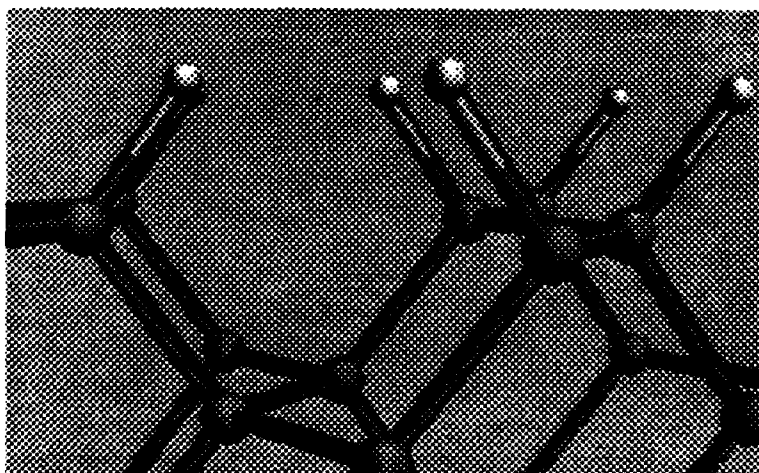


Figure 1. (110) hydrogenated diamond surface.

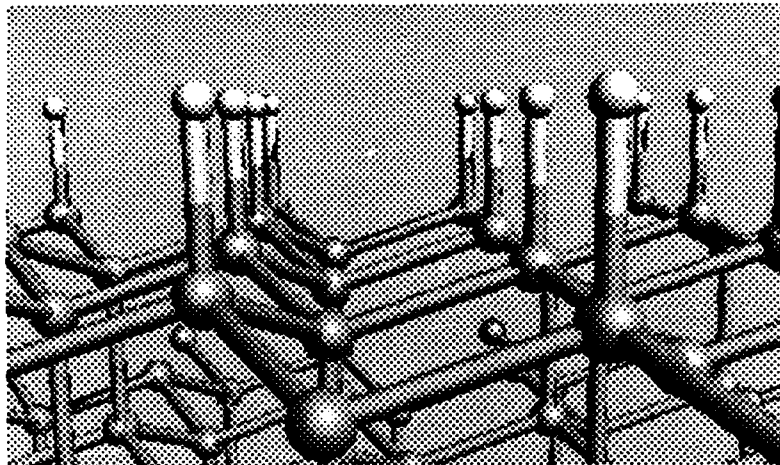


Figure 2. (111) hydrogenated diamond surface.

suggested as a dihydride (Fig. 3) or a disordered phase consists of patches of $(2n+1) \times 1$ structures [5, 6]. Previous theoretical studies on these surfaces have used empirical or semiempirical methods [7] and disagreement still exists. The purpose of our *ab initio* calculations is to resolve these issues.

The monohydride surface was modeled by a six-layer slab with the same surface on both sides, see Fig. 3. We started by minimizing the total energy from a surface geometry where the dimer length is equal to the typical C=C double bond (1.38 Å) length and C-H (1.09 Å) bond and angles (54.74° from surface normal) were set equal to that of CH₄. The relaxed surface is a 2×1 reconstructed one. The C-H bond tilted only 20° from surface normal due to the repulsion between H atoms on the neighboring dimers. This surface is very stable with a large energy bandgap in the electronic structure. No surface states were found inside the bandgap. This is consistent with other theoretical results [6, 7].

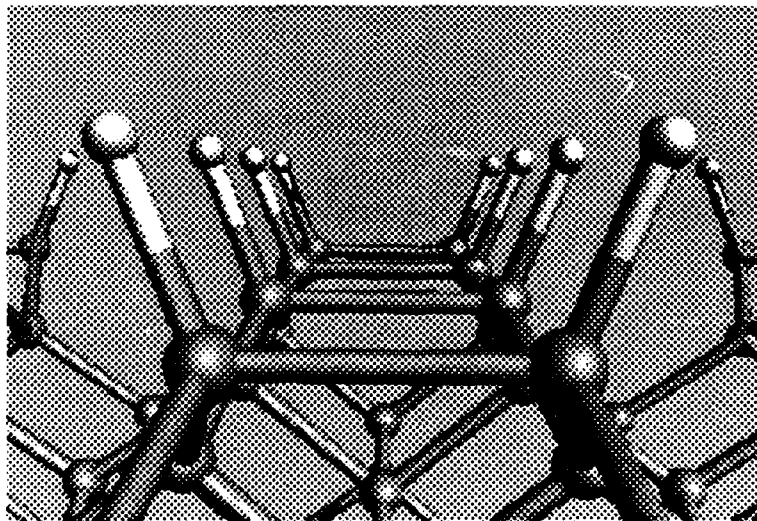


Figure 3. Monohydride (100) surface.

The calculations for the dihydride surface were done using slabs of both six layers and ten layers thick with about 10Å of vacuum spacing. The results of both calculations are qualitatively the same. Strong steric repulsion exists between the hydrogen atoms. The angle between the two C-H bonds of a surface C atom is 89°, in contrast to the starting ideal tetrahedral angle (109.47°). Nevertheless the surface does relax to a minimum energy structure (Fig. 4) in both the six and ten layer calculations. The stability of such a surface is now being studied by using simulated annealing, an important feature of the Car-Parrinello quantum molecular dynamics method.

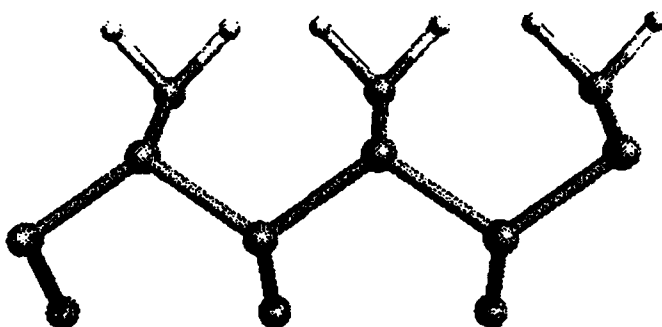


Figure 4. Dihydride (100) surface.

Surface Electronic States and Electron Affinity. Electron states at the surface often play important roles in determining the properties of a material. Certain diamond surfaces (hydrogenated (111) for example) may exhibit negative electron affinities, so that electrons at the conduction band edge can be emitted into vacuum. This effect could potentially make diamond useful in applications such as cold cathode emitters and detectors.

Information about electronic states are directly available from our *ab initio* calculations. Figures 5 and 6 show the analysis of wavefunctions for the hydrogenated (111) surface. The electron state corresponds to the bulk valence band maximum E_V is determined by its wavefunction being mainly inside the slab. A surface state could be identified if the wavefunction is concentrated on the surface region, see Fig. 6. For C(111):H we find that the highest occupied state is still the valence band top E_V , in other words there is no occupied surface state inside the bandgap. The C-H bonding surface state was found some 0.8 eV below E_V , which is consistent with the experimental results [8]. Similar results have been obtained for the (100) monohydride surface. For the dihydride surface, detailed electronic structure analysis is still underway.

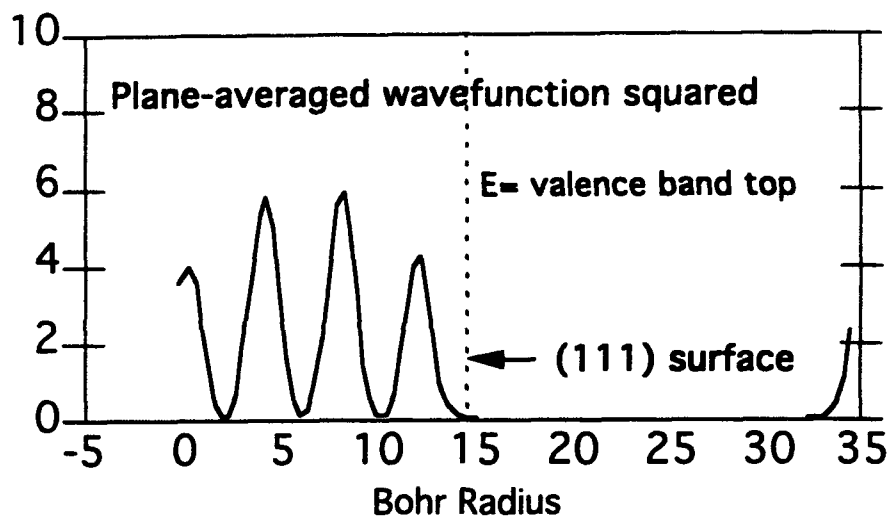


Figure 5. Plot of (111) valence band state.

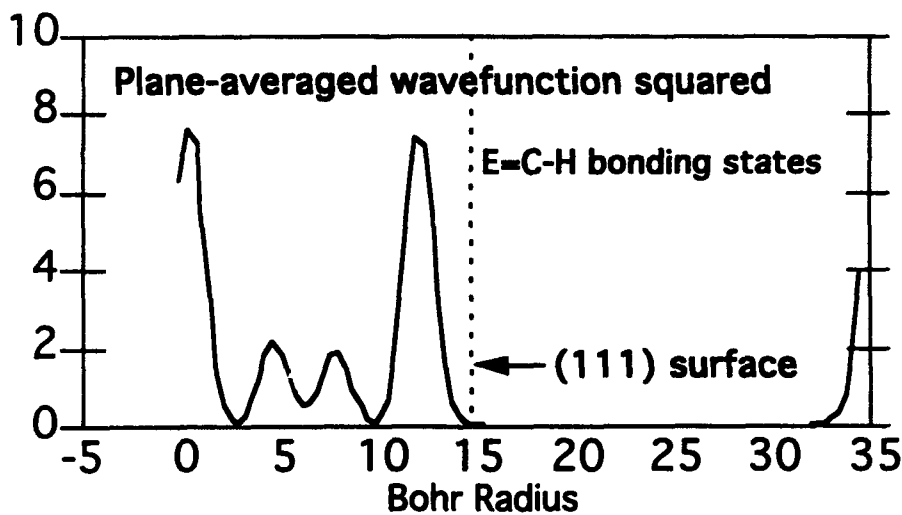


Figure 6. Plot of the (111) surface state.

Electron affinity is the distance from the conduction band minimum to the vacuum level. In order to determine the position of the vacuum level relative to the electron states of the system, we plot the plane-averaged, self-consistent potential versus the distance normal to the surfaces, see Fig. 7. Note that in pseudopotential calculations, the zero point of the energy eigenvalues is usually arbitrary. As one can see from Fig. 7, the effective potential has flattened out in the vacuum region, indicating that we have enough vacuum spacing between the slabs in the calculation. Since the LDA only gives good information about the occupied states, such as E_V to the vacuum level (3.91 eV), we have used the experimental value of 5.47eV for the bandgap. The conduction band is 1.56eV above the vacuum level for the

C(111):H surface, giving a negative electron affinity. A similar analysis shows the C(100)(2×1):H also has a negative electron affinity of -0.62eV. This agrees well with the photoemission studies on these surfaces by van der Weide and Nemanich [9].

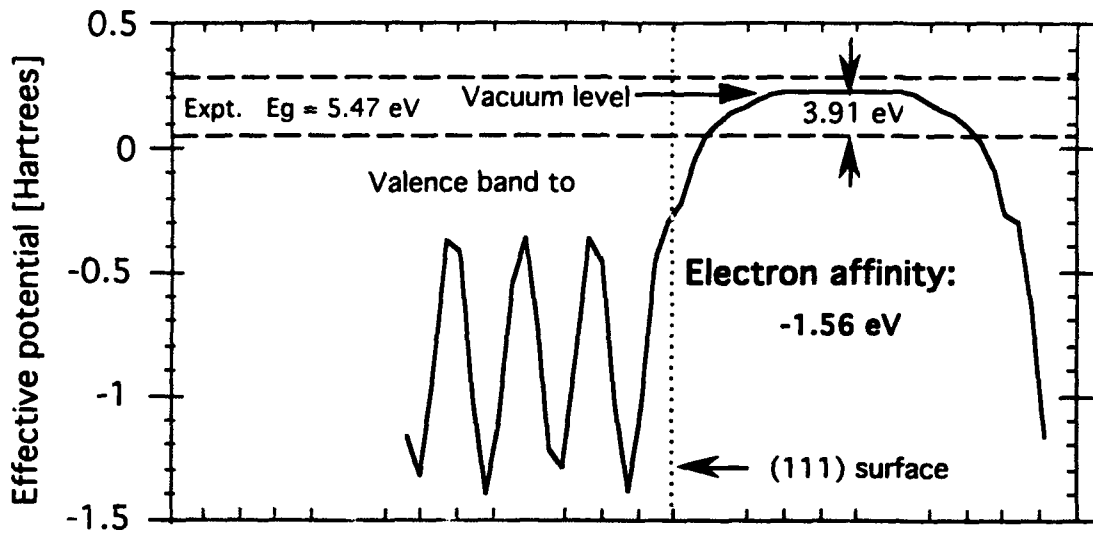


Figure 7. Plot of the plane-averaged potential of the (111) hydrogenated diamond surface.

C. References

1. New Diamond Science and Technology
2. R. Car and M. Parrinello, Phys. Rev. Lett. **55**, 2471 (1985).
3. T. Tsuno, T. Imai, et al, Japanese Journal of Applied Physics **30**(5), May, 1991.
4. A. V. Hamza, G. D. Kubiak, and R. H Stulen, Surf. Sci. **237**, 35 (1990).
5. C. Cheng, and J. G. Yates, Phys. Rev. B **43**, 4041 (1991).
6. Sang Yang, private communications.
7. S. P. Mehandru and A. B. Anderson, Surface Sci. **248**, 369 (1991).
8. J. van der Weide and R. J. Nemanich, private communications.
9. J. van der Weide and R. J. Nemanich, to appear in Appl. Phys. Lett.

Defects in GaN

A. Introduction and Computational Methodology

In our study of defects in GaN, we focus our attention on two defects. The first one is the substitutional C. The importance of this impurity stems from the fact that carbon atoms are always incorporated in nitrides during the process of growth because of the growth technique. Our results show that the formation energies are about 3 eV, i.e. relatively small for both the substitution on the cation and on the anion site. Therefore, the C impurity may be the amphoteric, i.e., the dopant site may depend on the conditions of growth. In consequence, the C atom belonging to Group IV of the Periodic Table may act as a donor in the Ga site, or as an acceptor on the N site. We also note the possibility of the self-compensation. The second defect studied was the N vacancy. According to the current viewpoint, this defect determines the predominant n-type character observed in most of the GaN samples. (Note that the p-type GaN has been obtained only very recently.)

In our calculations we address two questions relevant for the experiment, namely the formation energies of point defects and their electronic structure. The calculations provide the defect formation energies obtained as a function of the Fermi level position, i.e., as a function of type of dopants (donors or acceptors) and of their concentration. Similarly to surface problems, the computations were performed using the quantum molecular dynamics. We also use the large unit cell method. In this approach, the impurities are repeated periodically in the host crystal, and the considered unit cells contain 72 atoms. The energy cutoff for the plane wave basis is 30 Ry.

The first stage of calculations consisted in finding the equilibrium lattice parameters for the hexagonal GaN crystal. The obtained lattice constant is smaller than the experimental one by about 2%. The internal distortion (i.e., the relative shift of cation and anion sublattices driven by the hexagonal symmetry of the crystal) is about 1 per cent, in agreement with experiment. The optical bandgap is 2.5 eV, which is smaller than the experimental value by about 1 eV. These are typical errors associated with the usage of the local density approximation. The wave functions of electrons and holes are displayed in Figs. 1a and 2a, respectively. Both wave functions are built up mainly from the anion orbitals, which is a feature characteristic for ionic compounds.

B. Substitutional C

Electronic Structure of Substitutional C. C_{Ga} is a shallow donor, with the energy level located at about 0.2 eV below the bottom of the conduction band. The shallow character of this state is confirmed by the spatial extension of its wave function, see Fig. 1b. Further analysis reveals that the substitutional C_{Ga} also introduces a second impurity-related state,

wave functions

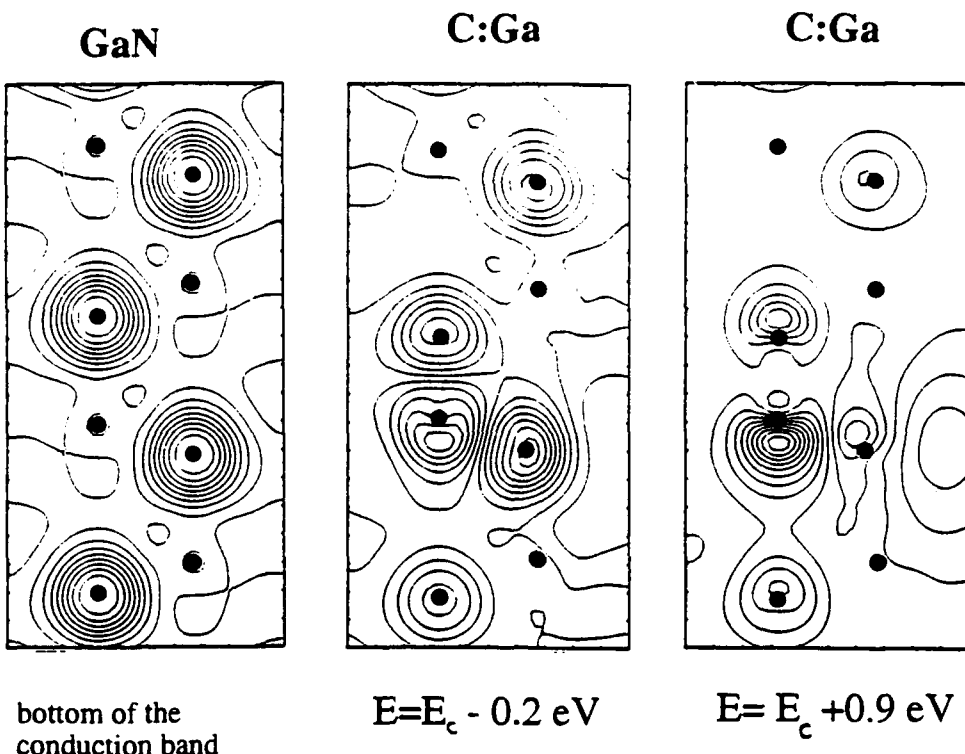


Figure 1.

namely a resonant state degenerate with the conduction band continuum. The energy of the resonance is 0.9 eV relative to the bottom of the conduction band, and its wave function shown in Fig. 1c. The fairly localized character of this state, clearly visible in Fig. 1c, is quantitatively confirmed by the Mulliken-type projection of the wave function onto atomic orbitals. From our analysis it follows that the contribution of C orbitals to the resonant state is 4 times larger than that for the shallow state.

C_N introduces a shallow acceptor level at about 0.2 eV above the valence band top. As in the case of C_{Ga} , the shallow character of this state follows not only from the energy value, but also from the delocalized character of its wave function, which is shown in Fig. 2b.

Finally, we observe that both $C:\text{Ga}$ and $C:\text{N}$, the energies of impurity levels are predicted with a relatively poor accuracy, which is of the order of the binding energy itself. This is due to the fact that the wave functions of shallow states are smeared out over the whole unit cell, and thus the impurity-impurity interaction is relatively large. We estimate the corresponding error to be of the order of 0.5 eV. However, we stress that the shallow character of these states is a feature that will persist in more accurate calculations.

wave functions

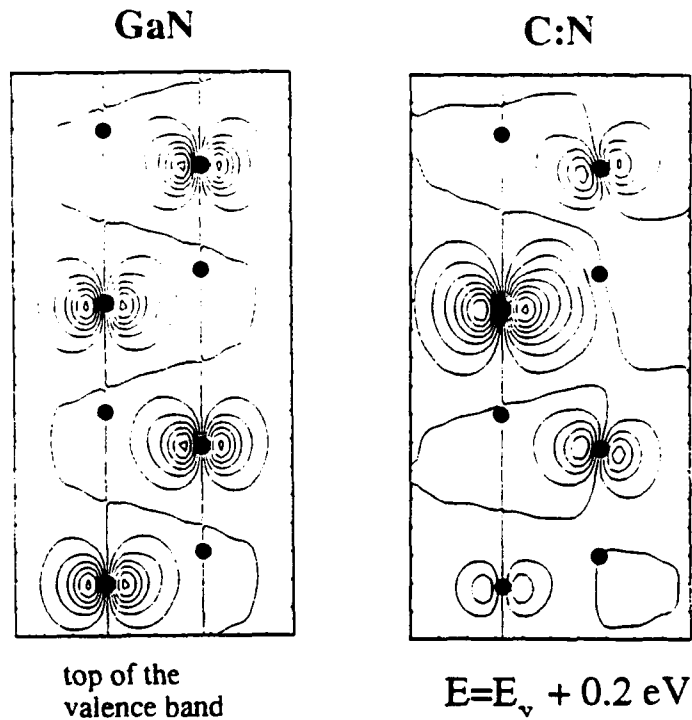


Figure 2.

Formation Energies of Substitutional C—Neutral Impurities. The formation energy of a substitutional C impurity in the neutral charge state is given by

$$E_{\text{form}}^0 = E[\text{GaN:C}_X] - E[\text{GaN}] + \mu(X) - \mu(C), \quad (1)$$

where E is the total energy, μ is the chemical potential, and $X=\text{Ga}$ or N . Chemical potentials depend on the source of atoms involved in the process and, therefore, on the actual experimental situation. We have assumed that the chemical potentials are those of solid C and Ga, and of the N_2 molecule, and used the experimental values of the cohesive energies. The corresponding values are $E_{\text{form}}^0(\text{C}_\text{Ga})=4.1 \text{ eV}$, and $E_{\text{form}}^0(\text{C}_\text{N})=2.2 \text{ eV}$.

Formation Energies of Substitutional C—Charged Impurities. Formation energy of charged states depends linearly on the position of the Fermi level μ_{el} ,

$$E_{\text{form}} = E_{\text{form}}^0 - \mu_{\text{el}} \Delta N, \quad (2)$$

where E_{form}^0 is given by Eq. 1 assuming the Fermi level at the valence band top, and ΔN is the change of the number of electrons occupying the impurity states. In our case of shallow donor and acceptor states, the dependence of E_{form} on the Fermi level is particularly simple,

since we may neglect the electron-electron interaction energy to a very good approximation, and obtain

$$E_{\text{form}} = E_{\text{form}}^0 - (\mu_{\text{cl}} - E_{\text{imp}}) \Delta N, \quad (3)$$

where E_{imp} is the energy of the impurity level. Equation 3 implies in particular that E_{form} of the positively charged donor C_{Ga} in p-type samples is reduced approximately by the value of the bandgap, i.e., from 4.1 eV to about 0.5 eV (assuming the experimental value of the bandgap). The same effect occurs for the negatively charged C_{N} acceptor in n-type samples, reducing the formation energy from 2.2 eV to -1.2 eV.

We observe that the calculated formation energies for both substitutional sites are relatively small. Therefore, the incorporation of C during growth is very likely. In fact, one may expect that C will be incorporated on both sites during a given growth process, which would result in a self-compensation.

Formation Energies of Substitutional C—Effects of Atomic Relaxation. In the calculations all atoms around the impurity were allowed to relax. The inclusion of this effect is important for obtaining correct results, especially for C_{Ga} . In this case, the atomic relaxation lowers the energy by as much as 1.63 eV, due to a large difference of atomic radii between C and Ga atoms. The relaxation preserves the hexagonal symmetry of the surrounding ("breathing" mode), and consists in the reduction of C-N bond lengths by about 17%. The relaxation-induced energy shifts of impurity state is about 0.8 eV. In the case of C_{N} , the relaxation energy is 0.12 eV, and the corresponding energy shift of impurity states is 0.1 eV.

C. The Nitrogen Vacancy

Electronic Structure. N-vacancy is a shallow donor, the single occupied donor level is located at 0.35 eV above the nominal position of the bottom of the conduction band. As we have already indicated, our method predicts the positions of extended states rather poorly, the estimated error being 0.5 eV. The shallow character of this state is again confirmed by both the direct inspection of the wave function, presented in Fig. 3a, and by the Mulliken-type analysis. From Fig. 3a it follows that this state is built up predominantly from s orbitals of N distant neighbors, and is very similar to the bottom of the conduction band in pure GaN displayed in Fig. 1a. The position of the vacancy is denoted by the diamond. One may notice the lack of the corresponding s(N) orbital. Further, the contribution of dangling bonds of the first shell of Ga atoms around the vacancy is negligible. In fact, the dangling bonds of the first neighbors of vacancy form a triplet situated at about 0.7 eV above the bottom of the conduction band. This triplet is split into singlet and doublet by the hexagonal crystal field, the splitting energy being 0.42 eV. The wave function of the singlet is shown in Fig. 3b. This state is dominated by the contribution due to the dangling bond of the lower Ga atom of the

first shell, and it contains also the p-like orbitals of N atoms from the second shell. The obtained energy level scheme of V_N agrees qualitatively with previous model calculations [1].

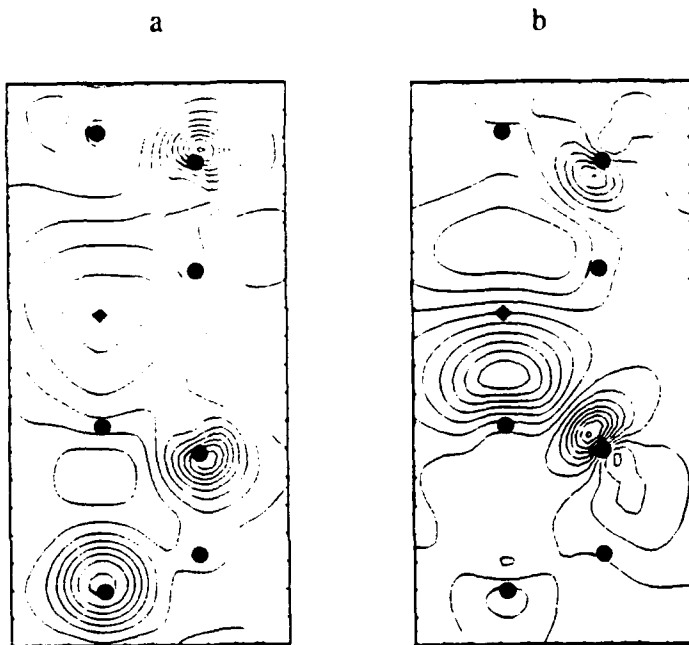


Figure 3.

Formation energies. The calculated formation energy for V_N is 5.8 eV for the neutral vacancy. This value is relatively high, and reduces to 2.3 eV in p-type samples according to Eq. 3. The energy of the atomic relaxation around the vacancy is 0.4 eV. In the equilibrium configuration the first shell of Ga is moved outwards the vacancy. However, the displacement of one Ga (the lower Ga in Fig. 3) is 0.2 Å, and that of the remaining three Ga (one of which is displayed in Fig. 3, the two others are out of plane) is 0.063 Å. This large non-equivalence corresponds well with the large hexagonal split of the vacancy-induced triplet, which was discussed above.

D. Reference

1. D. W. Jenkins and J. D. Dow, Phys. Rev. B **39**, 3317 (1989).

III. Infrared Investigations of Diamond Thin Films

A. Introduction

Infrared (IR) spectroscopy is a useful way to probe the bonding structure of diamond thin films. The positions of the various absorption features in the spectrum indicate the type of bond (C-H, Si-C, Si-H, etc.) and the amplitudes of the absorptions are a rough measure of the quantity of bonds. In addition, one can interpret the interference fringes found in IR reflection and transmission spectra to determine the thickness of the film.

This report contains preliminary IR measurements of diamond films using two different measurement techniques: attenuated total reflectance (ATR) and specular reflectance at an angle of 30°. ATR spectroscopy should be the more sensitive of the two techniques but is slightly more complicated and yields no information on film thickness. The specular reflectance complements the ATR measurements because quantitative analysis of the spectrum is possible to determine the optical constants and thickness of the film.

B. Experimental Procedure

Sample Preparation. Most of the work discussed below involves two samples of oriented diamond deposited on silicon using biased enhanced nucleation [1, 2]. The deposition process involves heating Si(100) wafer in microwave plasma of 2% CH₄ in H₂ to 720 °C and at 15 Torr. The substrate is then biased negative for 45–75 minutes before depositing diamond under standard growth conditions of 1% CH₄ in H₂, 15 Torr, substrate temperature = 720 °C, microwave power = 900 W, and 30 minutes. Under these deposition conditions, diamond films grow at a rate of about 0.1 μm/hr. We have made preliminary measurements on two samples: 1) Sample SW81 is biased at -225 volts for 74 minutes before diamond growth and 2) Sample SW80 is biased at -260 volts for 47 minutes before growth.

A third diamond sample is a randomly-oriented film on silicon grown by combustion chemical vapor deposition (CVD). The flame deposition system consists of an atmospheric torch burning C₂H₂ with O₂ in a stainless steel chamber. To prevent any secondary air from the atmosphere entering the flame, the chamber is backfilled with Ar prior to deposition. Sample #930426A is grown on scratched Si(100) using a two-step process [3-6]. The first step is a pretreatment in a fuel-rich flame of R = O₂/C₂H₂ = 0.89 for 5 minutes at a temperature of < 550 °C; the substrate is located approximately 20 mm from the inner cone. Following the pretreatment, we deposit for 15 minutes at a substrate temperature of 750–800 °C, distance of 1–2 mm, and R = 0.95. Optical microscopy of the film shows a well-faceted, densely nucleated film. No other analysis has been completed at this time.

In addition to the above samples, we have also made IR measurements on a bare silicon wafer. The silicon is single crystal with only a single side polished. The IR transmittance

through the wafer is zero, so reflectance measurements correspond to a single-surface reflectance not a double-surface reflectance.

Infrared Apparatus and Analysis Techniques. The infrared spectrometer for these measurements is a Fourier transform infrared (FTIR) instrument made by Analect (Model FX6260). The FX6260 scans the region between $4398\text{-}500\text{ cm}^{-1}$ (2.27-20 μm) at roughly 4 cm^{-1} resolution (the resolution varies slightly across the spectrum).

Two kinds of IR measurements have been made: specular reflectance and attenuated total reflectance (ATR). We use a 30° specular reflectance accessory from Pike Technologies for measurements of diamond on dielectrics like silicon. Since we use a mask on the sample surface to restrict the beam size, we must calculate the true sample reflectance (ρ_s) from the apparent reflectance using the equation

$$\frac{\rho_s}{\rho_{\text{mirror}}} = \frac{R_s - R_{\text{mask}}}{1 - R_{\text{mask}}} \quad (1)$$

where ρ_{mirror} = true reflectance of the reference mirror (~ 1), R_s = measured single beam reflectance of a sample divided by the measured single beam reflectance of the reference mirror, and R_{mask} = reflectance of the mask alone (referenced to the mirror).

The ATR measurements use total internal reflection to probe the surface of a sample pressed onto a high index of refraction material [7]. As long as the sample has an index less than the internal reflection element, the internally reflected light has an evanescent wave which extends into the sample about 1 wavelength. If the sample is absorbing at some wavelengths, the evanescent wave will be attenuated at those wavelengths, and a spectrum results. We use Ge as the internal reflection element because its refractive index is large enough ($n = 4$) that the evanescent wave will probe both silicon ($n = 3.4$) as well as diamond ($n = 2.41$). The crystal is a 60° parallelogram with the dimensions 25 mm long \times 10 wide \times 3 mm high. This geometry results in roughly 4-5 reflections total on both sides of Ge crystal. In the measurements discussed below, we press a sample onto only one side of the Ge crystal, so only two internal reflections probe the sample. The ATR spectra are referenced to the spectrum of the bare Ge crystal. The ATR spectra do not extend below 600 cm^{-1} because the Ge crystal absorbs too strongly below 600 cm^{-1} .

C. Results

Measurements using Attenuated Total Reflectance. Thus far, preliminary measurements with the ATR technique have been inconclusive. Figure 1 shows the ATR spectrum of the sample pressed onto the Ge crystal compared to the ATR spectrum calculated from two Ge reference spectra. Both spectra appear as absorbance spectra ($-\log[\text{sample}/\text{reference}]$). The

top spectrum shows that small misalignments in placing the Ge crystal produce features that dominate the spectra. The lower spectrum of the diamond on Si(100) shows the same Ge features, and there are no obvious carbon, silicon, or SiC features. Subtracting the two spectra also fails to reveal any features other than the Ge crystal features. Future work will try to overcome this problem.

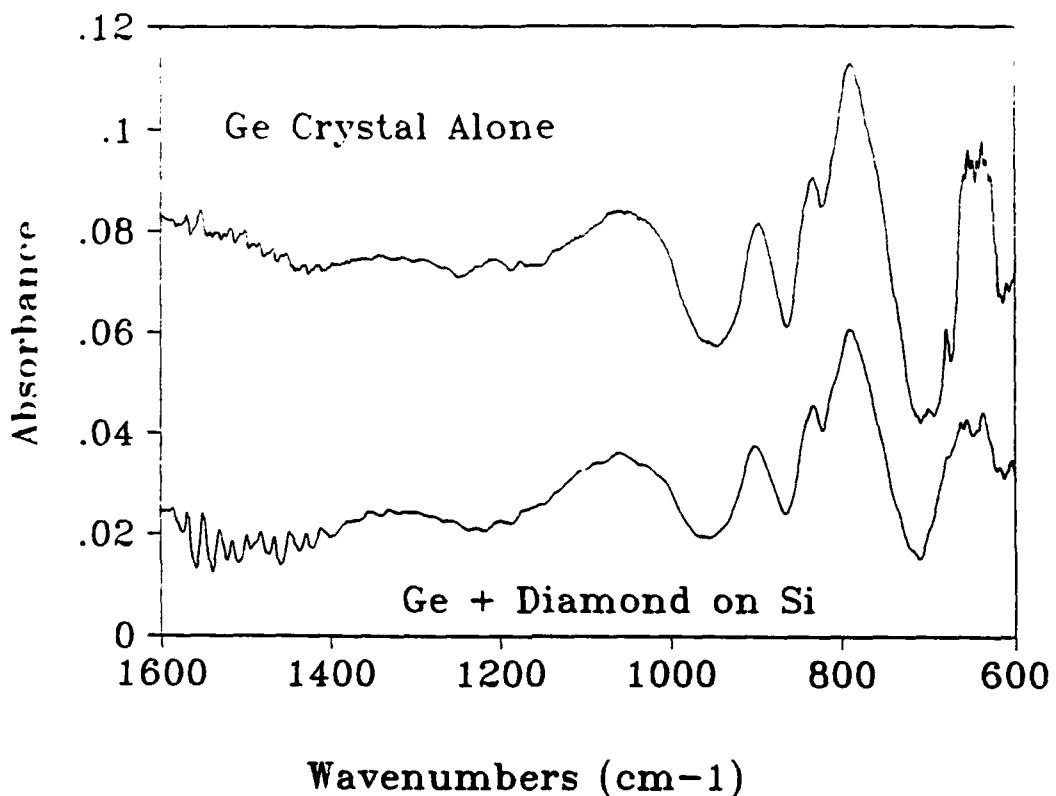


Figure 1. Attenuated total reflectance measurements of the Ge internal reflection crystal and a diamond film on silicon pressed onto the Ge internal reflection crystal.

Measurements using Specular Reflectance. Preliminary measurements using specular reflectance have been much more successful. Figure 2 compares the specular reflectance of a diamond film on Si(100) to the reflectance of a bare silicon wafer; both spectra are corrected for the mask spectrum using Eq. 1. Each spectrum contains sharp features in the regions $3900\text{--}3500\text{ cm}^{-1}$ and $1900\text{--}1350\text{ cm}^{-1}$ due to atmospheric water and another set in the region $2400\text{--}2300\text{ cm}^{-1}$ due to atmospheric CO_2 . The diamond film spectrum (Figure 2a) is qualitatively similar to the silicon spectrum (Figure 2b) except for the sloping baseline between $4000\text{--}1000\text{ cm}^{-1}$ due to the interference fringe of the film. In this form, these spectra are not very useful because they still contain features due to the FTIR's instrument response function (e.g. the oscillations between 2400 and 1500 cm^{-1} and the broad feature near

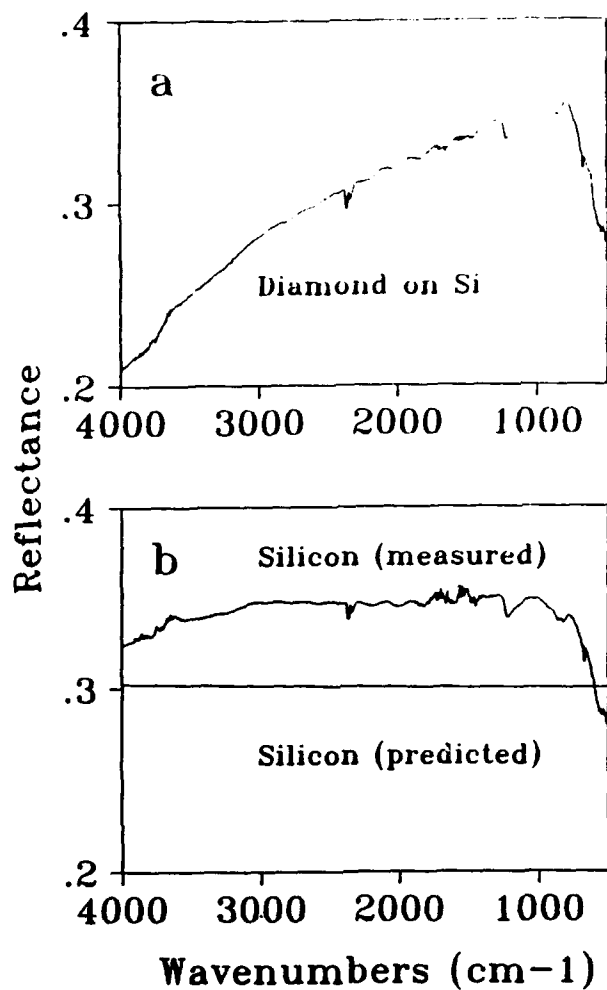


Figure 2. Mask corrected specular reflectance spectra. (a) Measured reflectance of a diamond film on Si(100); (b) Measured reflectance of a bare silicon wafer compared to the predicted reflectance for silicon.

1200 cm^{-1}). Under most circumstances, the process of taking the ratio of the single beam spectrum of the sample relative to the single beam spectrum of the reference mirror should have completely removed the instrument response function (IRF) from the reflectance spectrum. One case in which this process does not work is when the response of the IR detector (volts per watt of IR) is not the same for the sample spectrum and the reference spectrum. In the present case, the response of HgCdTe detector is slightly lower at the high intensity reflected from the reference mirror than the response at the low intensity reflected from the film or silicon. Consequently, the measured reflectance is slightly too high and some of the features of the instrument response function still remain in the reflectance spectrum. As a result, the reflectance of the silicon is higher than expected ($\rho_{\text{Si}} = 0.305$) and has unexpected features in it (Figure 2b).

We can compensate for this difficulty by referencing the film reflectance to the reflectance of the silicon. Since the film reflectance and the silicon reflectance are similar in magnitude, the IR intensity striking the detector in each measurement is nearly the same. Thus the detector response is nearly equivalent in each measurement, and the spurious features of the IRF are removed. Figure 3 shows the reflectance of the film in Figure 2a relative to silicon (Figure 2b). Note that the spectrum has the curving baseline due to the interference fringe of the film thickness and the expected feature near 800 cm^{-1} due to the silicon carbide peak. None of the features from the mirror reference appear. The spectrum also has no features due to the silicon reference since the reflectance of silicon is nearly constant across the mid IR (see the simulated spectrum in Figure 2b). All the analyses discussed below will use the silicon "mirror" as the reference.

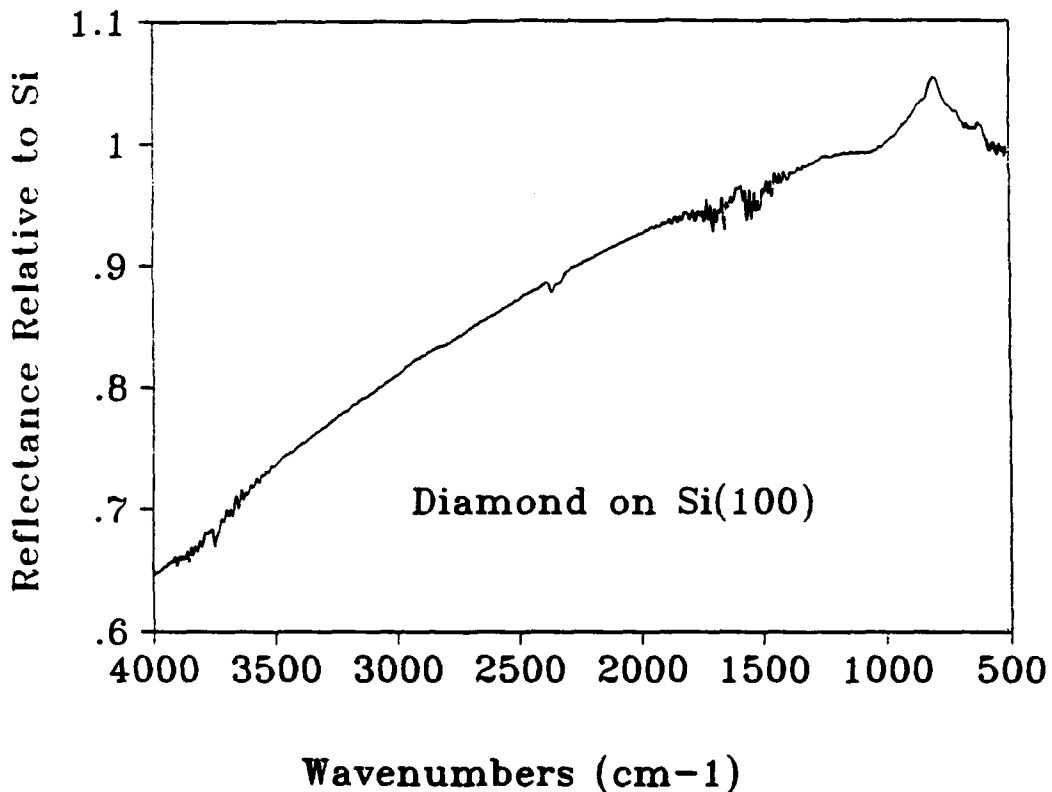


Figure 3. Specular reflectance of a diamond film referenced to the reflectance of a bare silicon wafer.

We have made several measurements of the two diamond films Samples SW81 and SW80. Figure 4 contains the relative reflectance of the center of Sample SW18 while Figure 5 shows the relative reflectance of the thicker edge of Sample SW81; Figure 6 displays the relative reflectance of the edge of Sample SW80. We have quantitatively analyzed these spectra to determine the thickness and optical constants of the films

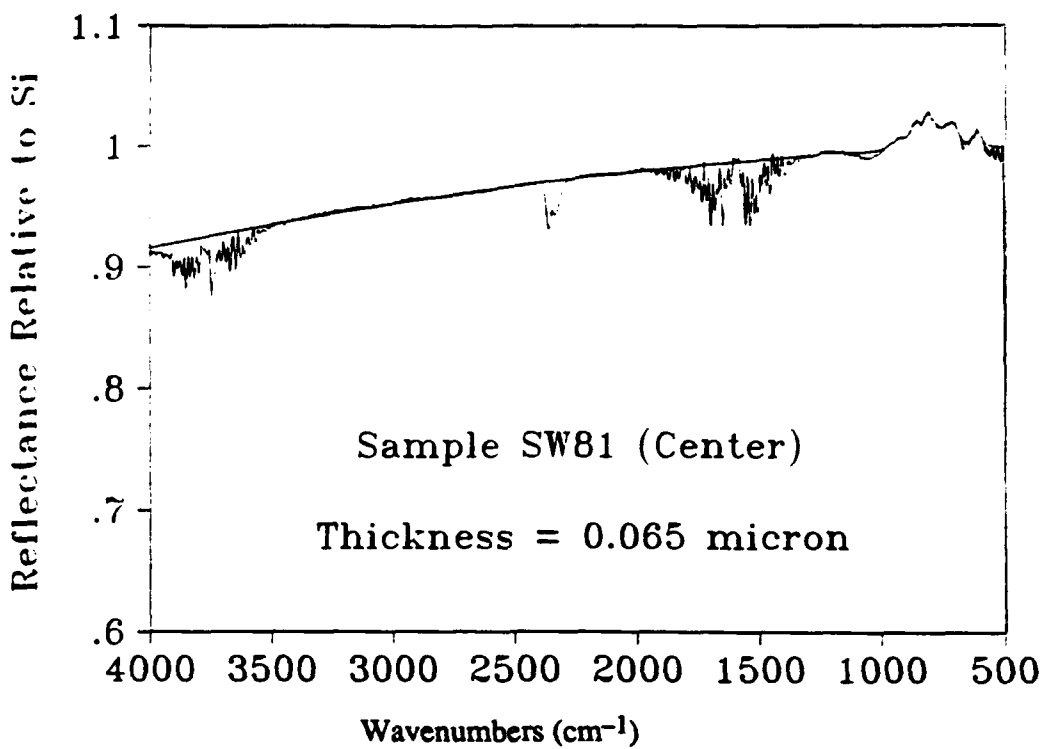


Figure 4. Specular reflectance of the center of Sample SW81 referenced to a silicon wafer. Also shown is a model fit using the thickness shown and the optical constants appearing in Figure 7.

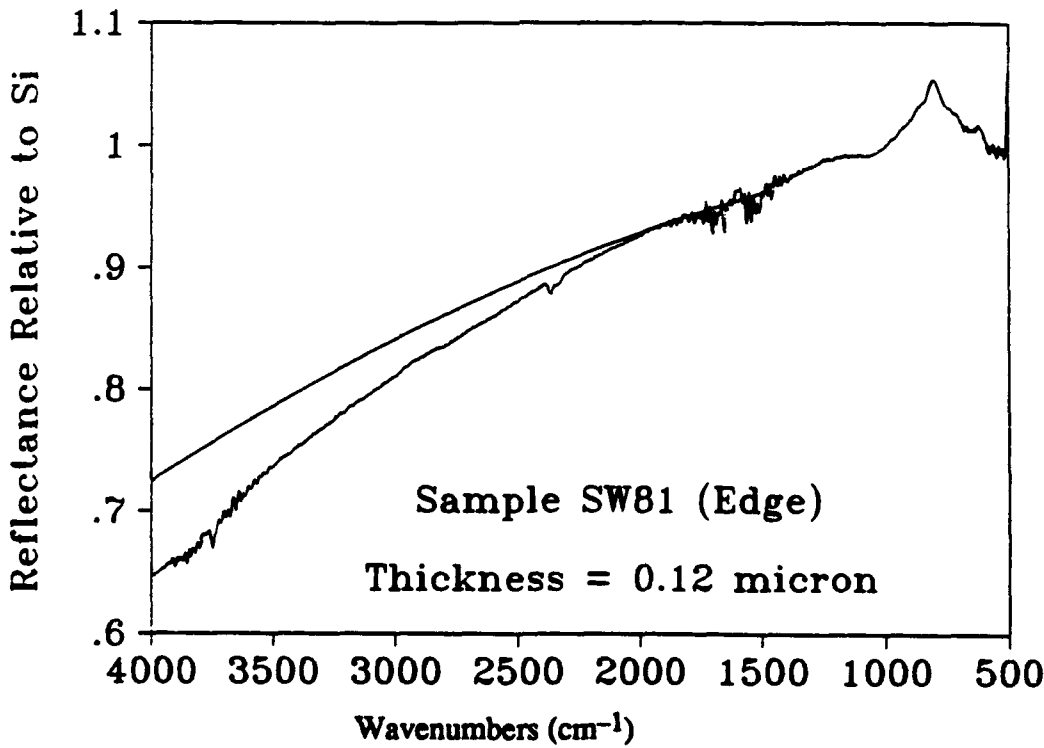


Figure 5. Specular reflectance of the edge of Sample SW81 referenced to a silicon wafer. Also shown is a model fit using the thickness shown and the optical constants appearing in Figure 7.

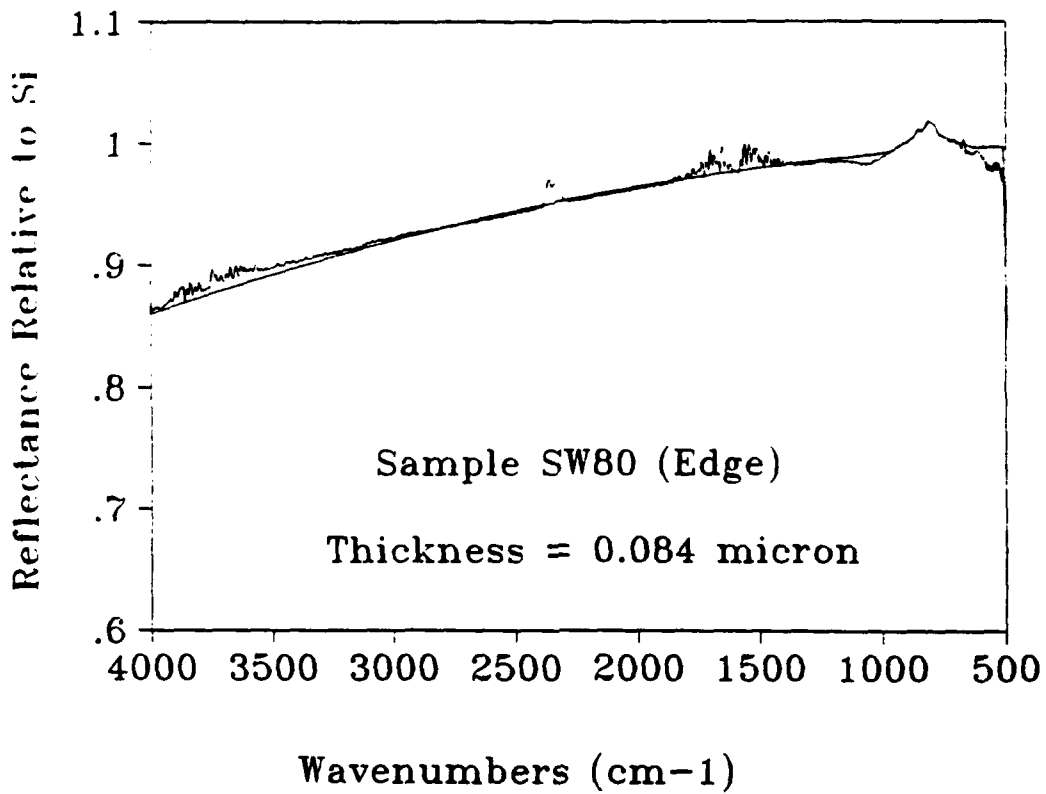


Figure 6. Specular reflectance of the edge of Sample SW80 referenced to a silicon wafer. Also shown is a model fit using the thickness shown and the optical constants appearing in Figure 7.

employing the following method. First, we assume there is only a single film on the silicon substrate. Using the optical constants of silicon and assuming the film has the same index of refraction as diamond (2.41), we simulate the reflectance of a single film on silicon with a trial value of the film thickness [8]. We then vary the film thickness manually until the predicted spectrum fits the interference fringe observed between $4000\text{-}1500\text{ cm}^{-1}$. We then calculate the complex dielectric function of the film for the entire spectrum by modeling the dielectric function as a sum of harmonic oscillators [9]. Using a set of 67 oscillators 30 cm^{-1} wide and spaced evenly between 1500 cm^{-1} and 500 cm^{-1} , we use trial values for the strengths of the oscillators and then sum the oscillators to calculate the complex dielectric function; this step also uses the assumed index of refraction. From the trial dielectric function and film thickness, we simulate the reflectance of the film and then compare it to the measured reflectance. We continue to vary the oscillator strengths until we achieve a good fit to the reflectance data. The resulting fits appear in Figures 4–6 and their corresponding optical constants appear in Figure 7.

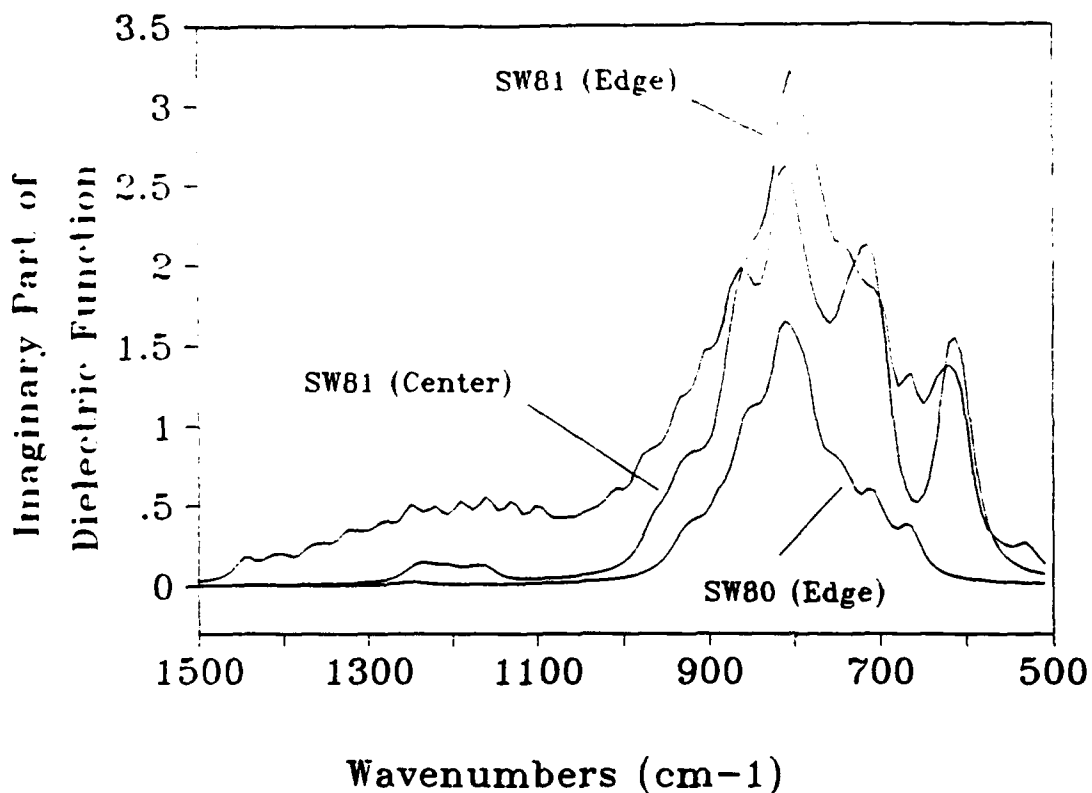


Figure 7. Imaginary (absorption) part of the complex dielectric function corresponding to the diamond films shown in Figures 4–6.

Figure 8 contains the spectrum of the diamond film deposited by a combustion flame. Please note that this spectrum has not been referenced to a silicon “mirror” so the interpretation is limited to film thickness only. Because the surface of this film is quite rough, scattering attenuates the observed fringes at high wavenumbers (Figure 8a). Nonetheless, we can estimate the film thickness by matching the maxima and minima with a simulated film on silicon. As shown in Figure 8b, a simulation using a thickness of 2.5 μm matches the maxima and minima below 2000 cm^{-1} .

D. Discussion

This discussion will concentrate exclusively on the interpretation of the spectra of the oriented diamond films (Figures 4–7). In the case of the two thinnest films (Figure 4 and 6), the fits to the interference fringe are quite good across the entire region between 4000–1500 cm^{-1} . For these spectra, the confidence limit on the fitted thicknesses is $\pm 0.001 \mu\text{m}$. The fit for the thicker film in Figure 5 is not as good, however, because scattering at the higher wavenumbers gives the measured fringe more curvature than expected. Using a slightly greater thickness than 0.12 μm does not compensate for this effect (the simulated fringe will cross the measured fringe). For this reason, we have chosen the thickness 0.12 μm

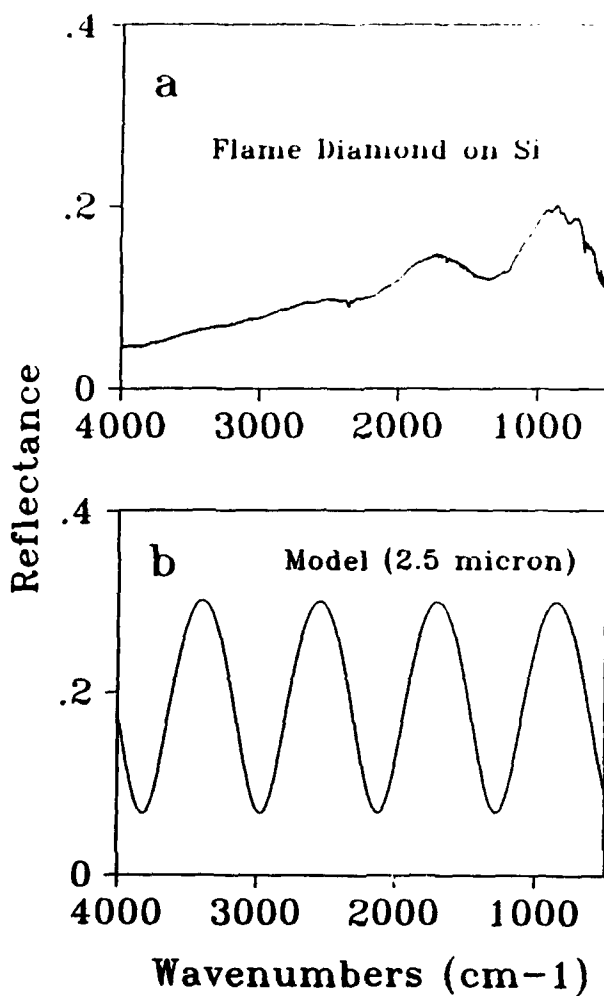


Figure 8. Specular reflectance of a diamond film deposited by a combustion flame onto Si(100). (a) Sample #930426A; (b) Simulated diamond film on silicon with a thickness of 2.5 μm .

because it produces a good fit in the region below 2000 cm^{-1} where scattering should not be a factor. The confidence limit in this fit, however, is $\pm 0.01 \mu\text{m}$. All of these thicknesses are consistent with the deposition rate of $\sim 0.1 \mu\text{m}/\text{hr}$ observed in the microwave CVD system.

The optical constants of the three films show interesting features (Figure 7). This figure contains only the imaginary part of the dielectric function because it contains all the absorption information of the film. In all the films, the dominant feature is the peak near 800 cm^{-1} corresponding to the Si-C stretch. This peak is fairly broad which is typical of amorphous SiC or amorphous hydrogenated silicon carbide (a-Si:C:H) [10]. The width of β -SiC films on silicon typically have widths between $10\text{--}30 \text{ cm}^{-1}$ [11]. Rubel *et al.* [12] note that for a-Si:C:H films, the SiC stretching mode is close to 730 cm^{-1} for silicon rich films but shifts to 800 cm^{-1} as the film becomes carbon rich. Such an observation would explain the appearance of the feature near 715 cm^{-1} as a silicon rich carbide peak near the substrate and

the 800 cm^{-1} peak as the carbon rich silicon carbide near the film (see Sample SW81(center), for example). The size of the peak also depends on the deposition conditions and the film thickness.

The shoulders at 920 and 860 cm^{-1} could be due to $\text{Si}-\text{CH}_x$ wagging, but the peak positions are significantly lower than the 1000 cm^{-1} other researchers have seen [10, 12]. Another possible assignment is the 920 cm^{-1} band is due to SiH_2 bending and the 860 cm^{-1} band is due to SiH_3 bending although this interpretation requires the peaks to be slightly higher ($20\text{--}30\text{ cm}^{-1}$) than reported for amorphous hydrogenated silicon (a-Si:H) films [13]. The bands at 660 cm^{-1} and 610 cm^{-1} are also consistent with SiH_x groups wagging. Again the band positions are slightly higher than observed for a-Si:H [13] but are in the range of a-Si:C:H [12]. Interestingly, none of the films show any sign of CH_x stretches at $2800\text{--}3000\text{ cm}^{-1}$ [10, 12] nor SiH_x stretches at $2000\text{--}2100\text{ cm}^{-1}$ [10, 12, 13]. All of these peaks are fairly narrow compared to their amorphous counterparts which would be consistent with a more ordered or crystalline film structure. More investigations will clarify the IR assignments.

E. Conclusions

We have performed preliminary infrared measurements of several diamond films using attenuated total reflectance (ATR) and specular reflectance. To date, the ATR measurements have been inconclusive because of alignment difficulties, but several routes to improve the sensitivity of the method have been identified. These options include more careful alignment, sandwiching the Ge crystal between two samples to minimize the effect of alignment errors, and using thinner crystals to increase the number of bounces through the sample.

IR specular reflectance of oriented diamond films shows that a silicon carbide layer exists at the interface of the film and the substrate as expected. In addition, the IR spectra contain features consistent with the bending and wagging modes of SiH_x groups. There is no IR evidence of CH_x in the spectra. Measurements of the thickness of these films and the combustion CVD films is also possible.

F. Future Work

Future work will focus on improvements to the ATR measurement methods and using the specular reflectance to study systematically the evolution of the diamond-silicon interface during biasing. We will also begin preliminary IR measurements of the growth of diamond on nickel substrates. These measurements will use specular reflectance at an angle of incidence of 80° to enhance absorptions of the film in the spectrum.

G. Acknowledgments

The authors gratefully acknowledge the assistance of Trey Simendinger in acquiring the IR spectra.

H. References

1. B. R. Stoner and J. T. Glass, *Appl. Phys. Lett.* **60**, 698 (1992).
2. B. R. Stoner, G.-H. M. Ma, S. D. Wolter, and J. T. Glass, *Phys. Rev. B* **45**, 11067 (1992).
3. J. A. von Windheim and J. T. Glass, *J. Mater. Res.* **7**, 2144 (1992).
4. M. T. McClure, J. A. von Windheim, J. T. Glass, and J. T. Prater, in *Materials Research Society Symposium Proceedings: Novel Forms of Carbon*, edited by C. L. Renschler, J. J. Pouch, and D. M. Cox (Materials Research Society, Pittsburgh, PA, 1992), Vol. 270, p. 323.
5. J. A. von Windheim, F. Sivazlian, M. T. McClure, and J. T. Glass, *Dia. Related Mater.* **2**, 438 (1993).
6. M. T. McClure, J. A. von Windheim, J. T. Glass, and J. Prater, *Dia. Related Mater.* submitted (1993).
7. N. J. Harrick, *Internal Reflection Spectroscopy* (Interscience Publishers, New York, 1967).
8. T. Buffeteau and B. Desbat, *Appl. Spectrosc.* **43**, 1027 (1989).
9. P. W. Morrison Jr. and R. M. Carangelo, in preparation (1993).
10. E. Gat, M. A. El Khakani, M. Chaker, A. Jean, S. Boily, H. Pepin, J. C. Kieffer, J. Durand, B. Cros, F. Rousseaux, and S. Gujrathi, *J. Mater. Res.* **7**, 2478 (1992).
11. C. J. Mogab, *J. Electrochem. Soc.* **120**, 932 (1973).
12. H. Rubel, B. Schroder, W. Fuhs, J. Krauskopf, T. Rupp, and K. Bethge, *Phys. Stat. Sol. B* **139**, 131 (1987).
13. M. H. Brodsky, M. Cardona, and J. J. Cuomo, *Phys. Rev. B* **16**, 3556 (1977).
14. P. C. Yang, W. Zhu, and J. T. Glass, *J. Mater. Res.* accepted (1993).

IV. Characterization of 6H-SiC Surface by RHEED and HRTEM

A. Introduction

In recent years several attempts have been made to understand the structure and chemistry of SiC surfaces with spectroscopic techniques. Auger electron spectroscopy (AES) and x-ray and ultraviolet photoemission spectroscopy (XPS and UPS) have been utilized [1,2] for the determination of surface composition, contamination and chemical bonding. For structural studies, low energy electron diffraction (LEED) [1,3], medium energy ion scattering (MEIS) [4], and reflection high energy electron diffraction (RHEED) [5] are commonly used. RHEED is now recognized to be one of the most powerful methods not only for surface structural studies but for the study of growth mechanisms in many systems using RHEED oscillation during growth [6–8]. In addition, recent progress in high resolution transmission electron microscopy (HRTEM) allows the direct observation of surface structures [9].

In this study, RHEED and HRTEM were used to investigate the SiC surface and the effects of the cleaning procedure and heat treatments on the surface structure such as step and terrace features. The future research will be included to establish the growth mechanisms of SiC polytypes (2H, 3C, 6H, etc.), AlN and AlN-SiC solid solutions through RHEED oscillation, HRTEM and spectroscopic techniques.

B. Experimental Procedure

The substrates used in this research were vicinal 6H-SiC (0001) oriented 3–4° towards <11̄20> (Si face) produced by Cree Research, Inc. As-received SiC substrates typically had an epitaxial SiC layer which was protected by an oxide layer. The following four samples were examined to understand the effects of the cleaning procedure and the heat treatments on the surface structure. Note that both procedures are usually required before growth to remove the surface oxide and contamination.

- i) as-received substrate (with epitaxial and oxide layers on the top)
- ii) chemically-cleaned substrate, using a 10% HF solution at room temperature for 10 min.
- iii) heat-treated substrate (after chemical cleaning) at 1050 °C for 30 min. in the UHV chamber (Ultra High Vacuum: base pressure 10^{-10} torr).
- iv) heat-treated substrate (after chemical cleaning) at 1200 °C for 30 min. in the UHV chamber.

RHEED and HRTEM were then used to investigate the surface structures of each sample. Samples were prepared for cross sectional TEM using standard techniques [10]. A Topcon EM-OO2B high resolution transmission electron microscope are used at 200kV to analyze the surface structures. The zone axes, <2110> and <1100>, used in the TEM observation in conjunction with surface geometry of the substrate were schematically illustrated in Fig. 1.

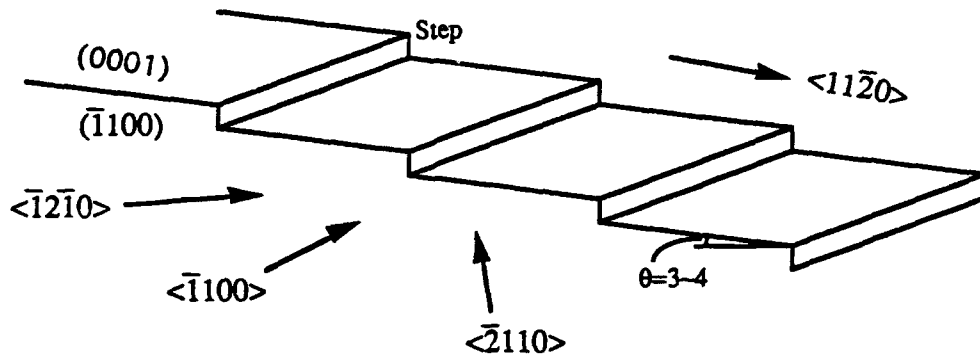


Figure 1. SiC surface features.

C. Results

i) *As-received substrate (with epitaxial and oxide layers on the top).* Figure 2 shows the cross sectional HRTEM image at the surface. Since the zone axis used here was $\langle\bar{1}100\rangle$, which was perpendicular to vicinal orientation $\langle 11\bar{2}0 \rangle$, the steps and the terraces of the surface can be directly observed. It is clearly seen that each step (indicated by arrows) represents bi-atomic heights and is distributed periodically, on the average every 40 Å. Figure 3 illustrates the schematic feature of a step.

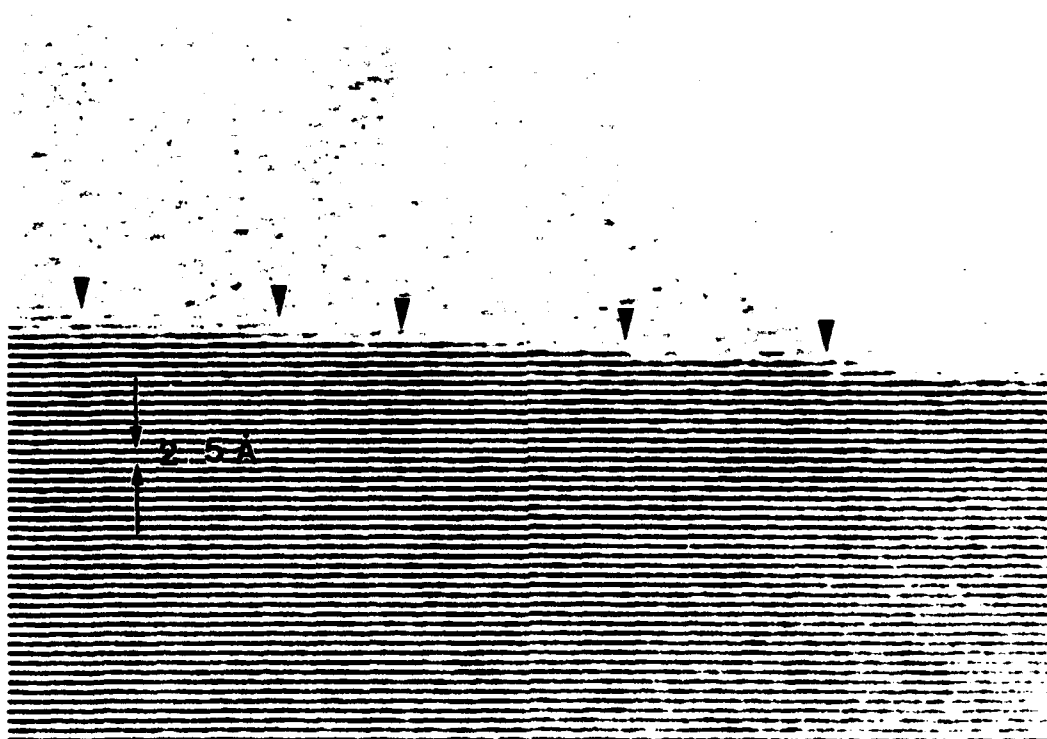


Figure 2. HRTEM image of the surface (as received substrate). $Z=\langle\bar{1}100\rangle$

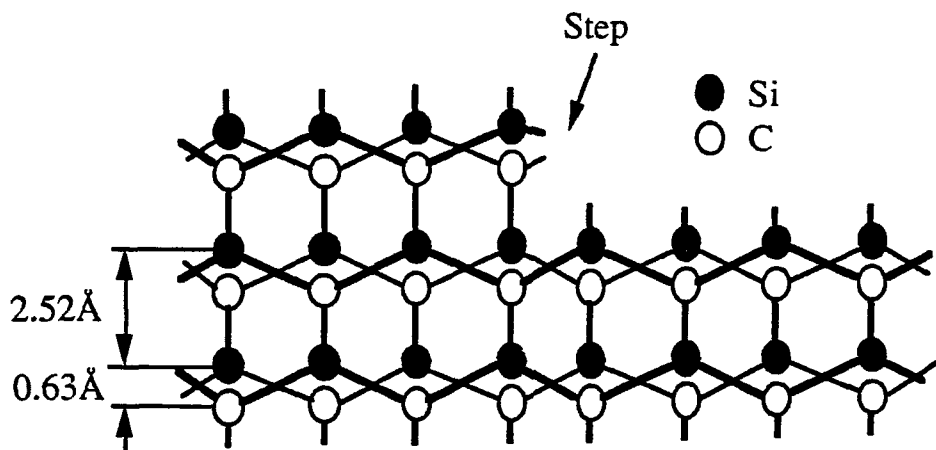


Figure 3. Schematic figure of a step (bi-atomic heights). $Z=\langle\bar{1}100\rangle$

ii) *Chemically-cleaned substrate, using a 10% HF solution at room temperature for 10 minutes.* The effect of the HF dip on the surface structure was investigated using HRTEM. After cleaning by the HF solution, the sample was examined in a similar manner as described in the previous paragraph. In Fig. 4, it is clearly seen that each step shows bi-atomic heights and the distance between the steps (terrace width) is $\sim 40\text{\AA}$. This implies that no significant structural change occurred after the HF dip, compared with the results of i) discussed above.

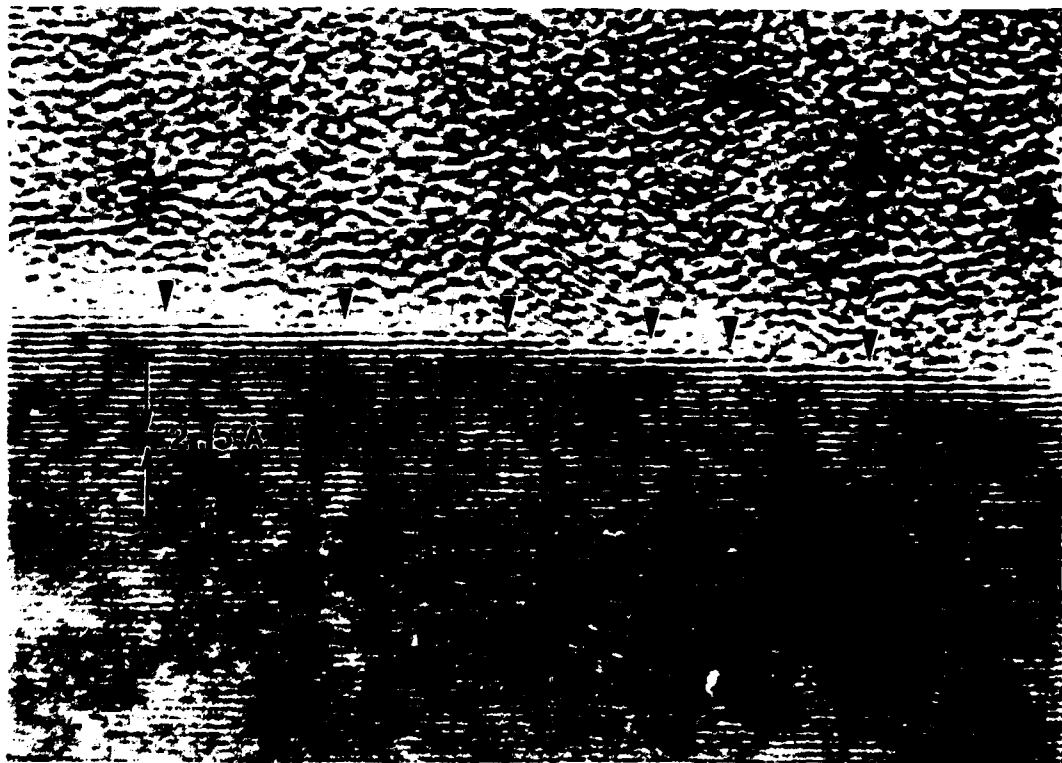


Figure 4. HRTEM image of the surface after HF treatment. $Z=\langle\bar{1}100\rangle$.

iii), iv) Heat-treated substrate (after chemical cleaning) in the UHV chamber. The effect of heat treatments in the UHV environment on the surface structure was investigated using RHEED and HRTEM. The samples were heated at 1050°C and 1200°C for 30 min. in the UHV chamber after they had been chemically cleaned. During the heat treatment RHEED analysis was performed to monitor the dynamic structural change of the surface.

At 1050°C, the RHEED pattern taken from $Z=\langle\bar{2}110\rangle$ appeared to be unchanged. The sample was subsequently prepared for HRTEM and the surface structure was observed. Figure 5 shows a HRTEM image of the surface ($Z=\langle\bar{2}110\rangle$). It might be seen that the step height and the terrace width varied during the heat treatment as indicated by the arrows and the numbers which correspond to the number of bi-atomic layers.

Similar results were obtained at 1200°C. Although the RHEED analysis showed no significant change in the pattern, the features of steps and terraces were obviously changed at this temperature, as seen in Fig. 6, indicating step bunching. Two to four bi-atomic steps (indicated by arrows) and wider terraces (~60~70Å) can be observed. However, it should be noted that the observing area was rather small. Thus, further investigations by RHEED and REM (Reflection Electron Microscope) would be desired.



Figure 5. HRTEM image of the surface after heat treatment at 1050°C.



Figure 6. HRTEM image of the surface after heat treatment at 1200°C.

D. Discussion

Understanding the surface structure and chemistry is of importance not only for the SiC substrates but subsequent film growth of SiC. Preliminary experiments implied that the surface structure of substrates may affect crystal structure of films. The different polytypes of SiC films such as 2H- and 3C-SiC have been obtained under the same growth conditions with only the heat treatment temperatures before growth differing. It can be inferred that the surface of the SiC substrate may structurally or chemically change in a certain temperature range. The results reported reveal this to be possible. Structural transition (step bunching) seen in the SiC surface which was heat treated at elevated temperatures may have occurred due to minimization of surface free energy. Thus it should be expected that the growth of different polytypes of SiC can be controlled by utilizing surface structural transition.

E. Conclusions

The surface structure of 6H-SiC substrates has been studied using RHEED and HRTEM. The effects on the surface structure due to the two major substrate cleaning procedures were investigated. The chemical cleaning procedure of 10% HF dipping was found not to introduce significant change in steps and terraces of the surface. On the other hand, the HRTEM results from the heat treatment experiments in the UHV environment at 1050°C and 1200°C might indicate some change in the surface structure (step bunching).

F. Future Research Plans

On the basis of present results, the growth of SiC films will be conducted on different surface structures. SiC films are expected to grow as different crystallographic structures, polytypes, because of the difference in surface free energy of the substrate which usually plays the role of a template of subsequent film.

G. References

1. A. J. Van Bommel, J. E. Crombeen, and A. Van Tooren, *Surf. Sci.* **48**, 463(1975).
2. L. Muehlhoff, W. J. Choyke, M. J. Bozack, and J. T. Yates, Jr., *J. Appl. Phys.* **60**, 2842 (1986).
3. R. Kaplan and T. M. Parrill, *Surf. Sci.* **165**, L45 (1986).
4. S. Hara, W. F. J. Slijkerman, J. F. van der Veen, I. Ohdomari, S. Misawa, E. Sakuma, and S. Yoshida, *Surf. Sci.* **231**, L196 (1990).
5. T. Yoshinobu, I. Izumikawa, H. Mitsui, T. Fuyuki, and H. Matsunami, *Appl. Phys. Lett.* **59**, 2844 (1991).
6. J. H. Neave, B. A. Joyce, P. J. Dobson, and N. Norton, *Appl. Phys. A-31*, 1 (1983).
7. T. Sakamoto, N. J. Kawai, T. Nakagawa, K. Ohta, and T. Kojima, *Appl. Phys. Lett.* **47**, 617 (1985).
8. T. Yao, H. Takeda, M. Funaki, *Jpn. J. Appl. Phys.* **25**, L952 (1986).
9. K. Yagi, H. Sato, K. Kobayashi, Y. Nishiyama, and Y. Tanaka, *Proc. 50th Ann. Meeting of Electron Microscopy of America (EMSA)*, 280 (1992).
10. J. C. Bravman and R. Sinclair, *J. Electron Microsc. Tech.* **1**, 53 (1987).

V. Integrated Surface Science System for Studies of the ALE of SiC

A. Introduction

In this report period, a concentrated effort has been made at completing assembly and construction of both an AES/XPS UHV analytical system and an associated ALE growth system. Much effort has also been spent in integrating these two systems into a much larger surface science system here at NCSU which has such capabilities as AES, AR-UPS, LEED, MBE, *in-situ* Raman, and Hydrogen Plasma Cleaning. Integration of all these separate systems will allow a very thorough study and characterization of both the initial nucleation of SiC (i.e. first few reaction cycles) and the overall ALE growth process of SiC.

B. Results

AES/XPS system. Completion of the construction and assembly of the AES/XPS UHV analytical system has been completed. The UHV system is capable of pressures in the 10^{-10} torr regime with the aid of both a 220 l/s ion pump and a Titanium sublimation pump. The AES/XPS system is composed of a VG LEG 62 electron gun, a VG XR3E2 x-ray source, and a VG CLAM-II hemispherical electron energy analyzer. Preliminary testing of the system has been performed on Au, Cu, and SiC samples with reasonably satisfactory spectrums being obtained in all cases indicating that the system is in good operational order. In order to perform both angle resolved AES and XPS, a manipulator with 5 degrees of freedom has been constructed. Two of the degrees of freedom (i.e. the necessary theta and phi rotations) were designed to be controlled by stepper motors. Control of these stepper motors has been achieved through the use of a special card purchased from Keithley-Metabyte Asyst and has also been tested.

ALE Growth Studies System. Completion of the growth system for the ALE of SiC has also just recently been completed. This system is actually a combined growth and analysis system with capabilities of performing adsorption kinetic studies, temperature programmed desorption (TPD), sub-monolayer gas dosing, and thick film growth (>20 nm). The growth studies system contains a Hiden Analytical Quadrupole Mass Spectrometer (HAL 201) and associated Hiden TPD hardware and software which allows the QMS to be used in remote operation by a computer for both TPD and gas adsorption studies. The QMS is currently operational and the integration of the TPD hardware and software with the sample heating system is currently in the debugging stage. Two gas dosers have also just recently been installed on this system with each doser being dedicated to a separate gas. The dosers are of the same design as the molecular beam dosers used by Dr. Yates at the University of Pittsburgh. [1] After much consideration, the gases which have been selected for use in these studies are Si_2Cl_6 and C_2H_2 . Selection of these gases was based primarily on the excellent

results of both Dr. Gates (IBM Watson) [2] with regards to Si₂Cl₆ and Dr. Yates (U. Pittsburgh) [3] with regards to C₂H₂. The Si₂Cl₆ has just recently been purchased and received from Cambridge Isotopes. The C₂H₂ will be obtained from the purification system currently in place on the separate SiC ALE reactor here at NCSU. The molecular beam dosers that are a part of this growth studies system will be used for both sub monolayer experiments and thick film growth. Sub monolayer exposures will be achieved via these dosers by restricting gas flow to occur through a laser drilled micron-sized orifice in a blank VCR gasket as with Dr. Yates' dosers. In order to achieve thicker film growth within a reasonable period time, the VCR gaskets with the micron sized orifices will be replaced with VCR gaskets which have a much larger orifice drilled in them (i.e. 0.1–5 mm). These gaskets are easily interchanged without having to bring the entire system up to atmospheric pressure as Nupro valves have been placed on both system side of the gasket and the gas line side of the gasket. The vacuum in this system should also not be jeopardized due to the resulting higher gas loads from the larger gaskets as the system has been equipped with a 500 l/s Varian ion pump, 400 l/s Leybold turbo pump, and a titanium sublimation pump. Currently this system has reached the high 10⁻⁹ torr regime with no bake out and is expected that 10⁻¹⁰ torr will be easily reached after bake out.

NCSU Surface Science System. The two previously mentioned UHV systems have been integrated with one another by connecting them to the larger NCSU Surface Science System. The NCSU Integrated Surface Science System brings together a variety of independent surface science systems (with support from both different ONR and other on-going programs) and is under the direction of Dr. R. J. Nemanich. Previously, the NCSU ISSS consisted of separate systems with the following capabilities: AR-UPS, AES/LEED, MBE, *in-situ* Raman, and Hydrogen Plasma Cleaning. The crux of this system is the long UHV transfer line (approximately 30 ft.) to which a variety of separate UHV systems are connected via ports perpendicular to the longitudinal axis of the transfer line (Fig. 1). This setup allows each UHV system to easily access all the other UHV systems with transfer times normally less than five minutes. As the pressure in the transfer line is currently nominally in the 10⁻⁹ region, this setup allows a variety of different experiments to be done *in-vacuo* eliminating contamination of samples by ambient conditions.

C. Discussion

The aim of the future research will be to utilize the newly completed AES/XPS and ALE growth systems to study the initial steps of a SiC ALE process (i.e. first few monolayers of growth). Advantage will also be taken of the analytical and cleaning techniques available as a result of being a part of the larger NCSU Surface Science System (i.e. UPS, LEED, and

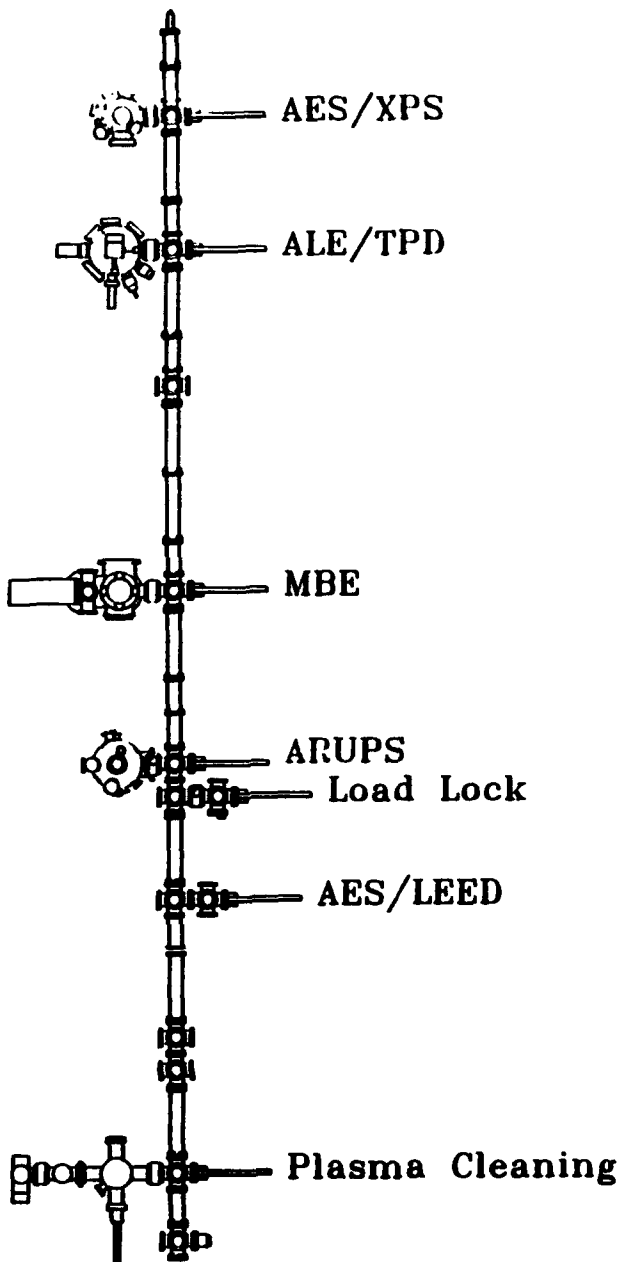


Figure 1. NCSU integrated surface science system.

Plasma Cleaning). All of these available analytical techniques will be used to study each step (and fraction of steps) of the ALE of SiC and the information gained from each technique will be combined with those from others to paint a sort of mosaic picture of the ALE of SiC.

Before any experiments are done which are directly pertinent to the ALE of SiC some initial experiments will be done to try and find the best *ex-situ* and *in-situ* methods of cleaning Si and SiC which are compatible with our setup. In order to characterize the cleanliness of the wafer's surface, both the AES/XPS and AES/LEED systems will be used and possibly the UPS. These three systems should characterize our cleaning process by identifying surface contaminants (AES/XPS/UPS), assessing surface order (LEED), and

determining the chemical nature of the surface carbon (XPS). TPD may also be used to determine the nature of any adsorbed contaminants as well as to see if the cleaning process has left a hydrogen terminated surface or residual hydrogen in the bulk of the crystal. These studies will be important for two reasons. First, in order to study in detail the underlying processes of ALE of SiC, one must have a well defined starting point with which one can consistently return and make reference to. Obviously, a clean Si or Si terminated SiC surface is the best reference point for these studies. Secondly, the above experiments will serve as a means of fine-tuning and calibrating the newer analytical techniques (i.e. AES, XPS and TPD).

Once suitable methods are obtained for cleaning Si and SiC which are reproducible and well characterized by the available analytical techniques, the focus of the research will quickly turn toward looking at the adsorption of Si_2Cl_6 on both Si and Si terminated SiC (001). The first experiments performed will be kinetic uptake measurements similar to those of Yates [3]. Ideally, these experiments would be followed by LEED, AES, XPS, UPS, and finally TPD. The logistics of the ISSS transfer system may suggest a different sequencing of these experiments, however, the ultimate combination of all these techniques will provide such information on:

- The temperature range over which chemically self terminating monolayers of Si_2Cl_6 can be adsorbed to Si and SiC.
- How the Si_2Cl_6 adsorbs (i.e. molecularly or dissociatively)
- The sites at which Si_2Cl_6 might adsorb
- The amount of Chlorine that remains on the surface.

In short, these sets of experiments should provide vital information on the first step of an SiC ALE process where Si_2Cl_6 is the process gas.

On completion of the Si_2Cl_6 adsorption studies, more ALE type studies will be performed in which C_2H_2 will be brought in to interact with adsorbed monolayers of Si_2Cl_6 . These studies will be performed in exactly the same fashion as those for Si_2Cl_6 except instead of starting with a clean Si or Si terminated SiC surface a surface pre-exposed to Si_2Cl_6 will be used.

D. Conclusions

Both an AES/XPS and ALE growth system have been established for the studies of the ALE of SiC. These two systems have been fully integrated with the NCSU Integrated Surface Science System allowing for a wide variety of analytical techniques to be employed on a single problem. This capability will enable a much better picture of the epitaxial growth of SiC (by ALE, MBE, etc.) to be painted, thus allowing the improvement of SiC epitaxial processes.

E. Future Research Plans and Goals

1. Characterize the *in-situ* and *ex-situ* cleaning process for SiC wafers.
2. Perform adsorption, TPD, AES-XPS, UPS, and LEED studies on the initial adsorption of Si_2Cl_6 on both Si and SiC (001).
3. Study the interaction of C_2H_2 with adsorbed Si_2Cl_6 monolayers.

F. References

1. M. J. Bozack, L. Muehlhoff, J. N. Russel, W. J. Choyke, J. T. Yates, *J. Vac. Sci. Technol. A* **5**, 1 (1987).
2. D. D. Koleske, S. M. Gates, and D. B. Beach, *Thin Solid Films* **225**, 173 (1993).
3. C. C. Cheng, R. M. Wallace, P. A. Taylor, W. J. Choyke, J. T. Yates, *J. Appl. Phys.* **67**, 3693 (1990).

VI. Determination of the Diffusivity of Si, C, Al and N at the Interface of the SiC-AlN Diffusion Couple

A. Introduction

Silicon carbide has long been of interest because of its superior structural, thermal and electrical properties. High temperature and/or erosion- and corrosion-resistant wear parts, as well as optoelectronic and microelectronic semiconductor devices are representative applications. Control of the physical and chemical properties of SiC via microstructural changes achieved by using different processing routes has been extensively studied for many years. The microstructural variables most frequently changed include the amount and the morphology of the various polytypes in the processed material, intentionally introduced second and additional phases and additions of sintering aids which may or may not form a grain boundary phase. The processing temperature, impurity content, and sintering (or annealing) atmosphere affect the resultant microstructure. However, the primary material remains SiC. Another approach to property engineering involves the alloying of SiC with other ceramic compounds to alter, e. g., the band gap. This approach has also been of interest for several years.

One compound which has been reportedly alloyed with α (6H)-SiC ($a_0 = 3.08\text{\AA}$) is AlN ($a_0 = 3.11\text{\AA}$) due to the similarities in the atomic and covalent radii and the crystal structures. Diverse processing routes have been employed to achieve partial or complete solid solutions from these two compounds including reactive sintering or hot pressing of powder mixtures and thin film deposition from the vapor phase [2–5,8,16–20,22,23]. There exists, however, a difference in opinion among investigators regarding the occurrence and the extent of solid solutions in the SiC-AlN system at temperatures $< 2100^\circ\text{C}$.

Schneider [1] concluded that the formation of $(\text{AlN})_x(\text{SiC})_{1-x}$ solid solutions were not favorable within the temperature range of his study of the AlN-Al₄C₃-SiC-Si₃N₄ system. He found two phase mixtures rather than $(\text{AlN})_x(\text{SiC})_{1-x}$ solid solutions when equal molar ratios of either SiC and AlN or Si₃N₄ and Al₄C₃ were hot pressed at 1760°C–1860°C for 45 and 30 minutes, respectively. Subsequently, Zangvil and Ruh [4] prepared sintered samples of varying compositions by cold pressing powdered mixtures of SiC and 10–50 wt % AlN and subsequently hot-pressing them in vacuum. Microstructures of the samples hot-pressed within the range 1850–1950°C revealed partially sintered AlN grains and β -SiC grains of unusually large size. Ruh [2,19,26] using dry mixtures of SiC and AlN powders, hot-pressed in vacuum under the conditions of 35 MPa and 1700–2300°C obtained no SiC-AlN solid solution for temperatures $\leq 2100^\circ\text{C}$ and concentrations of ~35 to 100 mol % AlN. In contrast, Rafaniello [8] reported solid solutions as indicated by X-ray diffraction in samples only hot-pressed at 1950°C–2300°C and 70 MPa for ~3 h in Ar. However, he subsequently showed [3] using a

more careful analysis of his X-ray diffraction data that the broadening of the SiC-AlN peak was caused by the existence of a two-phase region and not the 2H solid solution previously reported [8]. The initial confusion was caused by the closeness ($\approx 1\%$) in the lattice parameters of SiC and AlN. This was supported by optical microscopy of multiphase assemblages in the sintered samples for temperatures as high as 2300°C. Rafaniello [3] also revealed strong evidence of a miscibility gap by the precipitation of SiC-rich phase from 75 wt % AlN solid solution and precipitation of an AlN-rich phase from a 47 wt % AlN alloy, when hot-pressed samples were annealed at 1700°C for 90h. Modulated structures were found by Kuo [5] for samples with equimolar compositions below $\approx 1900^\circ\text{C}$ and in samples containing 25 mol % SiC – 5 mol % AlN annealed at 1700°C for 170 h. Likewise, Chen [22] hot-pressed a mixture of β -SiC and AlN powders in nitrogen at $\approx 2300^\circ\text{C}$ for 20 min to 3.5 h. Samples were then annealed in nitrogen (1 atm) over a range of temperatures between 1600°C–2000°C for up to 1145 h. Modulated structure development in samples of equimolar composition annealed at 2000°C and below indicated that 2000°C is below the coherent spinodal which would give further evidence of a miscibility gap as reported by Rafaniello [3], Kuo [5] and Sugahara [6].

Common to all the investigations described above was the use of AlN and β -SiC powders supplied by Herman Starck and the high concentrations of impurities contained in these materials. The concentration of oxygen and boron in starting powders [2–5,8,18–20,22,23] is significant. Xu and Zangvil [18] found small Al₂O₃ inclusions embedded in 2H grains of SiC-AlN samples uniaxially prepressed at room temperature to 35 MPa and subsequently hot-pressed at 2150°C at a pressure of 40 MPa in a flowing nitrogen atmosphere (1 atm.). The oxygen needed for the formation of the Al₂O₃ inclusions was beyond the 2% content reported in the analysis of the as-received AlN and, therefore, was probably introduced during processing. This is of considerable importance since Tajima [9] found that in the temperature range of 1800°C–2000°C the solid solubility of aluminum in SiC may be influenced by impurities and by the heating atmosphere; since, the defect structure of SiC would be affected by these factors. He also found conclusive evidence that aluminum atoms substitute for silicon in SiC. Furthermore, Zangvil [4] suggested that aluminum and nitrogen move as well as silicon and carbon as diffusion couples to ensure a local charge balance during mass transport. This process would be strongly impurity dependent and therefore control the solid solution formation. Oden [20] attempted to deal with the issue of impurities by preparing Al₄C₃ and SiC and comparing these with Hermann Starck- SiC and Cerac- AlN. The impurities of the latter materials were reported, however, those contained in Oden's materials were not. It was suggested by Oscroftt [21] that the oxygen content present in both materials was very high. Furthermore, the highly reducing nature of the graphite hot-pressing die may be the controlling factor in the oxygen content for both pure and impure materials [21]. Further evidence of the effects of oxygen was presented in a later study by Kuo [27] who found the existence of an

extensive, if incomplete, solid solution between AlN and Al₂OC at temperatures in excess of 1900°C. Below about 1800°C, the 2H solid solution was unstable and decomposed into two solid solutions of 2H crystal type as shown by the presence of extremely fine precipitates developed during cooling. The kinetics of solid solution formation were relatively rapid when compared with the SiC-AlN system, assuming such solutions actually occur in this latter system. This is of considerable importance when considering the high oxygen content in starting AlN materials. It should also be noted that two different phase diagrams have been presented for the SiC-AlN system Zangvil and Ruh [26] and Patience [30]. The most widely accepted was proposed by Zangvil and Ruh [26]. It is based on data obtained from numerous sintering experiments [2-4,8,19].

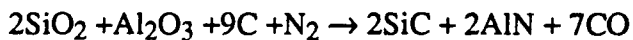
In contrast to the studies described above are reports of the formation of solid solutions between SiC and AlN at relatively low processing temperatures (i.e. within the proposed miscibility gap region). Cutler [7] formed solid solutions between SiC and AlN from 2 mol % to 100 mol % AlN with a single wurtzite type phase, as determined by X-ray diffraction. This was accomplished by the carbothermal reduction of fine amorphous silica ('cabosil'), precipitated aluminum hydroxide, and a carbon source of starch/sugar in a nitrogen atmosphere at 1400°C–1600°C. In subsequent work, by Rafaniello [8], intimate mixtures of SiO₂, Al₂O₃ and C were reacted at 1650°C for 4 h in flowing N₂. Solid solutions over the entire composition range were reported.

Processing conditions and impurities were shown to be factors affecting the solid solution formation by Czekj [24]. He prepared solid solutions of 2H-(AlN)_x(SiC)_{1-x} from rapid pyrolysis ("hot drop") of organometallics at temperatures < 1600°C. In contrast, slow pyrolysis of mixtures produced compositions rich in 2H-AlN and 3C-SiC at 1600°C which were later transformed to 2H-(AlN)_x(SiC)_{1-x} solid solutions after heating to 2000°C. Jenkins, *et al.* [16] reported the growth of solid solutions of (AlN)_x(SiC)_{1-x} by MOCVD over the entire composition range from 20 % to 90 % AlN in the temperature range of 1200°C–1250°C, as measured by Auger spectroscopy. Kern [17] reported growth of a high purity (AlN)_{0.3}(SiC)_{0.7} solid solution at 1050°C by plasma-assisted gas source molecular beam epitaxy.

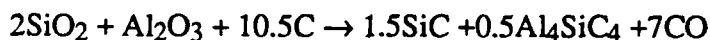
Theoretical calculations of the immiscibility region in the (AlN)_x(SiC)_{1-x} system were conducted by Sukhanek [28] using the dielectric theory of A^NB^{8-N} semiconductors. The theory relates changes in the band structure to the enthalpy of formation in semiconductors. He concluded that the formation of a continuous series of solid solutions of silicon carbide with aluminum nitride were possible above 1000°K. This was shown by Shimada [10] who hot pressed mixtures of SiC, Si₃N₄, AlN and Al₃C₄ powders at 1300°C–1900°C and 3.0 GPa for 1 h and reported the formation of solid solutions by X-ray diffraction. Tsukuma [11] also sintered mixtures of Si₃N₄ and Al₄C₃ in a gas autoclave at 1800°C and 10 MPa in argon. Solid solutions rich in AlN were produced. However, solutions in the SiC-rich region could not be

formed under the same conditions. Zangvil [12] suggested that this phase was a solid solution of $(\text{AlN})_x(\text{SiC})_{1-x}$ based on lattice parameters; however he also noted that he found no solid solution at 1900°C in vacuum and that Schneider [1] did not form solid solutions at 1860°C. It is interesting to note the short processing time < 1 h. Tsukuma's [11] findings are consistent with the proposed kinetics and reaction path described by Rafaevich [29] and Mitomo [15].

Rafaevich [29] used conditions similar to Zangvil [4] to determine the kinetics of the reaction between Si_3N_4 and Al_3C_4 . The purpose of his work was to determine the formation mechanism of the $(\text{AlN})_x(\text{SiC})_{1-x}$ solid solutions during sintering. Diffraction patterns after sintering for 0.5 h at 1950°C in 1 atm of nitrogen indicated that SiC had not completely formed and that Si_3N_4 was still present. Sintering for 1 h at 1950°C indicated that Si_3N_4 had completely transformed into SiC; however, solid solutions of SiC-AlN had not completely formed. Sintering for 1.5 h at 1950°C showed a complete, homogeneous $(\text{AlN})_x(\text{SiC})_{1-x}$ solid solution. Reaction paths studied by Mitomo [15] were determined by the formation of a uniformly dispersed composite powder of β -SiC and 2H-AlN using an alkoxide-derived SiO_2 - Al_2O_3 mixture. The total reaction was carried out at 1500°C and of the form:



The large amounts of carbon (3.7 time the normal amount) were needed to complete the reaction. Reactions observed at 1500°C were



Large weight loss after the reaction was attributed to the evaporation of SiO_2 as SiO . Mitomo [15] suggested that SiO_2 and Al_2O_3 reacted in sequence with carbon. This is of substantial use in the evaluation of the reported attempts to form solid solutions which have been previously published. The indication is that the formation of $(\text{AlN})_x(\text{SiC})_{1-x}$ solid solutions using SiO_2 and Al_2O_3 in a N_2 atmosphere is not favorable for short sintering times due to the complex reaction scheme.

Zangvil [4] has approximated the diffusion coefficients between SiC and AlN to be $10^{-12} \text{ cm}^2 \cdot \text{s}^{-1}$. The corresponding activation energy and pre-exponential term were estimated to be as high as 900 kJ·mol, and $10^{-8} \text{ cm}^2 \cdot \text{s}^{-1}$, respectively. Three reasons for these values were suggested by Zangvil [4]: (1) SiC penetration among AlN grains in the early stages of sintering (2) material transport by gaseous species, and (3) lattice diffusion of coupled SiC and AlN pairs.

The purpose of this investigation has been to determine the extent of solid solution formation within the temperature range of 1700°C–1850°C and to determine the diffusion

coefficients and the corresponding activation energies for the four elements Si, C, Al and N within this solution. It is clear that the atomic behavior and the extent of phase formation at relatively low temperatures for thin film deposition cannot be discerned from the research conducted previously. Likewise, the diffusivities of these species have not been studied for epitaxially deposited AlN on single crystal SiC.

B. Experimental Procedures

Sample Preparation. Samples were prepared in a modified Perkin-Elmer 430 molecular beam epitaxy (MBE) system. Aluminum (99.999%) was evaporated from a standard effusion cell. Activated nitrogen was achieved using an MBE compatible, electron cyclotron resonance plasma source. Single crystal AlN with very few planar defects was epitaxially deposited on vicinal α (6H)-SiC [0001] wafers manufactured by Cree Research, Inc. and cut off axis 3° - 4° toward [1120]. Growth conditions for the films are presented in Table I.

Table I. Growth Conditions for the 2H AlN films on α (6H)-SiC(0001) substrates

Nitrogen pressure	2×10^{-4} Torr
Nitrogen flow rate	4-5 sccm
ECR microwave power	50 W
Substrate temperature	650°C
Growth rate	$\approx 0.1\mu\text{m/hr}$
Total growth time	7-8 hrs.

Transmission electron microscopy (TEM) (Hitachi H-800) photos have been taken of the 2H-AlN (wurtzite) film on the α (6H)-SiC substrate before annealing and show a smooth and abrupt interface. Several different precautions were taken in order to prevent contamination of the samples and to minimize the loss of volatile components principally aluminum, and nitrogen. The samples were placed in a high density pyrolytic graphite crucible shown schematically in Fig. 1. The inside of the crucible was previously coated with SiC by heating a mixture of Si and β -SiC inside the holder to 2000°C. The diffusion samples were placed inside this holder with the α (6H)-SiC(0001) face against the SiC coating. Bulk AlN squares were then placed on top of the deposited AlN. The holder was then closed using a threaded lid and loaded into the furnace. The chamber was evacuated (2×10^{-6} torr) to prevent contamination during diffusion. N₂ gas (99.9995%), purified by a gettering furnace containing heated Cu chips (Centorr Furnace model 2B-2O) was then introduced into the chamber at a rate of

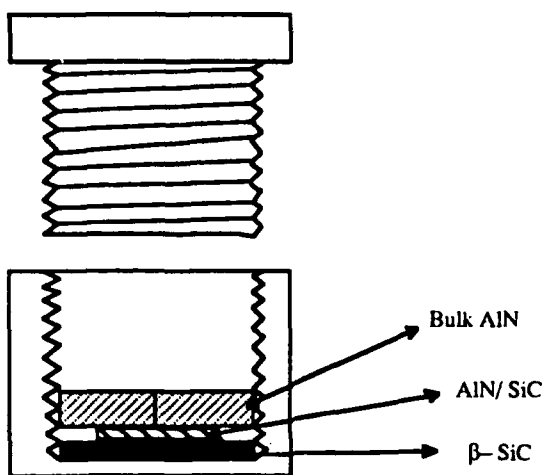


Figure 1. Schematic of a high density pyrolytic graphite crucible.

365 sccm. The chamber was brought to atmospheric pressure and a flowing N₂ environment maintained throughout each diffusion anneal. Diffusion temperatures were reached in ≈20 min (exact value for 1850°C). The samples were then removed for characterization. The N₂ gas, bulk AlN, and SiC coated crucible are not meant to aid in the diffusion. This was checked by a SiC-AlN standard which had not been annealed. The AlN as well as the SiC intensity in the standard were the same as AlN and SiC intensity outside of the diffused region. The samples were diffused for a temperature range of 1700°C to 1850°C for as wide a range of times as possible. A complete listing of temperatures and times are given in Table II.

Table II. Annealing conditions used to date for the AlN/SiC diffusion couples

<u>Sample #</u>	<u>Temperature (°C)</u>	<u>Time (hrs)</u>
32	1850	25
28	1850	21.5
21	1850	10
26	1800	30
31	1800	25
29	1800	20
27	1750	70
23	1750	50
18	1750	25
33	1700	70
19	1700	30

Characterization-Auger Spectroscopy. Scanning Auger microprobe (SAM) (JEOL JAMP-30) analysis was used to determine the concentration verses diffusion distance for all samples in Table II. Samples were tilted at a 60° angle in order to minimize charging effects. An argon ion sputtering unit attached to the SAM was used to sputter through the samples while data was being collected. Sputter rates were determined for the Ar ion beam in three different types of media namely, AlN, SiC and their solid solutions. This was accomplished by 5, 10 and 15 minute sputter rates on AlN and SiC then extrapolated for longer times in each medium. The depths were measured using a profilometer. The sputter rates for the solid solution region were determined by measuring the depth of different samples of different sputter times where the ion beam had sputtered through the entire diffused region and subtracting the sputter times for AlN and SiC. This rate was plotted and extrapolated for longer times. Knowing sputter rates for each material allowed for the conversion of sputter time to distance. Sputter rate standards also served as standards for the 100% intensity peaks for Al, N, Si, and C from which relative concentrations were obtained.

Characterization-Transmission Electron Microscopy. The samples was cut into 3 micron wide and 500 micron thick discs which were mechanically thinned to about 100 microns and dimpled at the SiC-AlN interface to a final thickness of 20 microns. Further thinning of the samples with an ion miller achieved an electron transparent area. An acceleration voltage of 6 kV for initial milling was used; it was decreased to 4 kV for the final milling. The milling angles of 15°, 12°, and 6° were used in sequence during the milling. TEM observations were subsequently conducted using Akashi EM-002B Ultra-High Resolution TEM at 200 kV. The TEM was conducted only on the longest runs to demonstrate microstructure.

C. Results

From Auger depth profiles it is apparent that diffusion has occurred and from the smoothness of the concentration verses distance profiles there is no indication of a two-phase region for samples annealed between 1700°C–1850°C. This indicates that complete solid solution formation over the entire composition range has been obtained. Using calculated sputter rates, values of concentration verses diffusion distance were determined. The Boltzmann-Matano diffusion equations were used to determine the diffusion coefficients for each element. It is possible that the α (6H)-SiC is transformed to the 2H-SiC polytype as a result of its initial contact with the AlN. If this is true, the calculated activation energy should be reduced by the amount of energy needed to transform the α (6H)-SiC to 2H-SiC. The solid solution subsequently occurs between the 2H-SiC and 2H-AlN via coupled diffusion in order to maintain local charge equilibrium. It should be noted that this is not the only means of forming the 2H solid solution. It is also possible that the diffusion of AlN into SiC causes the

transformation of SiC to the polytype 2H. In this case the reduction of the activation energy by the transformation energy may be incorrect.

In order to determine the diffusivities of the four components of the process the Boltzmann-Matano solution of the diffusivity, D, as a function of concentration, distance, and time (c, x, t) is being employed. At this writing, the Auger data is being carefully analyzed to ensure that diffusion has actually occurred between these two materials. The reason for this uncertainty is derived from the fact that in a parallel investigation of the apparent diffused region using electron energy loss (EELS) in cross-sectional TEM with a 15Å beam, the presence of Al and N as well as Si and C have not been observed in the SiC layer and the AlN film, respectively. Bright field TEM of the surface in cross section has revealed a stepped surface with very high steps. As such, it is important to make absolutely sure that the Auger electron beam is not detecting components from two different steps and thus giving an apparent diffusion profile rather than providing data of a real profile from the formation of solid solutions.

D. Future Research

Additional diffusion anneals will be conducted between 1750 and 2000°C using the same procedure described above. Special care will be used to ensure that a flat AlN surface is achieved after the diffusion experiments and prior to the Auger Depth profile studies. A quartz flat coupled with a He lamp will be used to check the flatness of the AlN surface. Light polishing with diamond paste will be used to produce the flat surface if it is not present after the diffusion anneals. Additional studies to be conducted in tandem with the diffusion runs include (1) the fabrication of solid solutions using MBE and the subsequent annealing at high temperatures to determine if either segregation of the AlN and SiC occurs or if the solid solution is maintained, thus proving that it is an equilibrium phase and (2) the additional use of EELS to determine if interdiffusion can be discerned at any temperature.

E. References

1. G. Schneider, L. J. Gauckler and G. Petzow, Material Science Monographs **6**, 399 (1980).
2. R. Ruh, A. Zangvil, J. Am. Ceram. Soc. **65** [5], 260 (1982).
3. W. Rafaniello, M. R. Plichta, A. V. Virkar, J. Am. Ceram. Soc. **66** [4], 272 (1983).
4. A. Zangvil, R. Ruh, J. Mat. Sci. and Eng. **71**, 159 (1985).
5. S. Kuo, A. V. Virkar, W. Rafaniello, J. Am. Ceram. Soc. **70** [6], C-125 (1987).
6. Y. Sugahara, K. Sugimoto, H. Takagi, K. Kuroda, C. Kato, J. Mat. Sci. Lett. **7**, 795 (1988).
7. I. B. Cutler, P. D. Miller, W. Rafaniello, H. K. Park, D. P. Thompson and K. H. Jack, Nature **275**, 434 (1978).
8. W. Rafaniello, K. Cho, A. V. Virkar, J. Mater. Sci. **16** [12], 3479 (1981).
9. Y. Tajima, W. D. Kingery, Am. Ceram. Soc. [2], C-27 (1982).

10. M. Shimada, K. Sasaki, M. Koizumi, Proc. of Inter. Sym. on Ceram. Components for Engines, (1983).
11. K. Tsukuma, M. Shimada, M. Koizumi, J. Mater. Sci. Lett. **1**, 9 (1982).
12. A. Zangvil, R. Ruh, J. Mater. Sci. Lett. **3**, 249 (1984).
13. K. A. Schwetz and A. Lipp, in *Am. Ceram. Soc.* 89th Annual meeting abstracts, The American Ceramic Society, Westerville, OH, p. 30, 1987.
14. R. A. Youngman, J. H. Harris, J. Am. Ceram. Soc., **73** [11], 3238-46 (1990).
15. M. Mitomo, M. Tsutsumi, Y. Kishi, J. Mat. Sci. Lett. **7**, 1151-1153 (1988) .
16. I. Jenkins, K. G. Irvine, M. G. Spencer, V. Dmitriev, N. Chen, J. Cry. Gro. **128** 375-378 (1993) .
17. R. S. Kern, L. B. Rowland, S. Tanaka, R. F. Davis, "Solid solutions of AlN and SiC grown by plasma-assisted, gas-source molecular beam epitaxy," J. Mat. Res.
18. Y. Xu, A. Zangvil, M. Landon, F. Thevenot, J. Am. Ceram. Soc. **75** [2], 325-333 (1992).
19. R. Ruh, A. Zangvil, J. Barlowe, Am. Ceram. Soc. Bull., **64** [10], 1368-1373 (1985).
20. L. L. Oden, R. A. McCune, J. Am. Ceram. Soc. **73** [6], 1529-1533 (1990).
21. R. J. Oscroft, D. P. Thompson, J. Am. Ceram. Soc. **74** [9], 2327-2328 (1991).
22. J. Chen, Q. Tian, A. V. Virkar, J. Am. Ceram. Soc. **75** [4], 809-821 (1992).
23. S. Y. Kuo, Z. C. Jou, A. V. Virkar, W. Rafaniello, J. Mat. Sci. **21**, 3019-3024 (1986).
24. C. L. Czekaj, M. Hackney, W. Hurley, L. Interrante, G. Sigel, P. Schields, G. Slack, J. Am. Ceram. Soc. **73** [2], 352-357 (1990).
25. A. Zangvil, R. Ruh, Silicon Carbide, 63-82 (1988).
26. A. Zangvil, R. Ruh, J. Am. Ceram. Soc. **71**[10], 884-890 (1988).
27. S. Kuo, A. V. Virkar, J. Am. Ceram. Soc. **72** [4], 540-550 (1989).
28. G. Sukhanek, Y. M. Tairov, V. F. Tsvetkov, Pis'ma Zh. Tekh. Fiz. **8** [12], 739-741 (1983).
29. N. B. Rafaevich, V. F. Tsvetkov, A. N. Komov, S. G. Losevskaya, Iz. Aka. Nauk SSSR, Neorg. Mater. **26** [5], 973-977, (1990).
30. M. M. Patience, P. J. England, D. P. Thompson , K. H. Jack, *Proc. of Inter. Sym. on Ceram. Components for Engine*, p. 473-479 (1983) Japan.

VII. Interface Properties of Wide Bandgap Semiconductor Structures

A. Introduction

All of the common polytypes of silicon carbide possess many physical properties that are very appealing to engineers of electronic devices. This material is well suited to high-power, -speed and -temperature applications because of its high junction breakdown electric field of 5×10^6 V/cm [1], high-saturated electron drift velocity of 2×10^7 cm/s for 6H [2], wide bandgap of 2.2 eV for 3C [3] and high thermal conductivity of 3.5 w/cm°C [4]. In addition to electronic applications, SiC enjoys potential in optoelectronics where blue light emitting devices are possible and have been constructed [5]. These features make SiC an appealing semiconductor material.

Integration of SiC into existing device manufacturing processes would be greatly facilitated by the development on a technology with the ability to deposit uniform layers of SiC on Si substrates. Although chemical vapor deposition, (CVD), has been employed for depositing SiC on Si substrates, deposition of good quality material involves an initial carbonization step and high growth temperatures. Both steps would be detrimental to device properties. Atomic layer epitaxy, (ALE), has been employed to deposit SiC films on Si without resorting to carbonization steps or extreme growth temperatures. In addition, ALE suggests the capability of depositing films over non-planar substrates with excellent uniformity and step coverage. Development of the ALE technique in reference to SiC deposition may encourage the incorporation of SiC's superior properties into the existing Si-based technology.

Determining the uniformity of deposited SiC films and developing reliable means to dope deposited films are important steps in developing the ALE technique. It is the objective of this research to determine the uniformity of ALE-deposited SiC films and to produce and characterize doped SiC films. The following subsections describe the equipment to be used in the research and plans developed to accomplish the stated objectives.

B. Experimental Procedure

A unique ALE reactor pictured in Fig. 1 will be employed to produce SiC films for analysis in this work. Within the reactor, substrates are alternately exposed to source gases to accomplish growth in a layer-by-layer-fashion. Many different source materials are available for deposition: disilane, ethylene, acetylene (cryogenically purified with the apparatus pictured in Fig. 2), ammonia and triethylaluminum. Hot tungsten filaments are located in the ammonia and hydrogen streams for cracking the ammonia or producing atomic hydrogen. Results of previous work done depositing SiC and GaN with this apparatus are published elsewhere [6,7].



Figure 1. Atomic layer epitaxy system.

Uniformity of Deposition. The immediate goal of this research will be to deposit SiC films on trenched Si substrates to assess the uniformity of the deposited film and the suitability of ALE for producing devices in trenches. The first step in accomplishing this first task will be production of the trenched substrates. Trenches of various widths will be produced in Si substrates to give a range of aspect ratios. These substrates will be produced in the microelectronics fabrication facility at N.C State University in the following manner (see Fig. 3).

Preparation of Trenched Wafers

Prepare all wafers.

1. RCA clean Si(100) substrates oriented 3° off axis toward <011>.
2. Dry-wet-dry oxidize substrates to form ~5000Å of SiO₂.

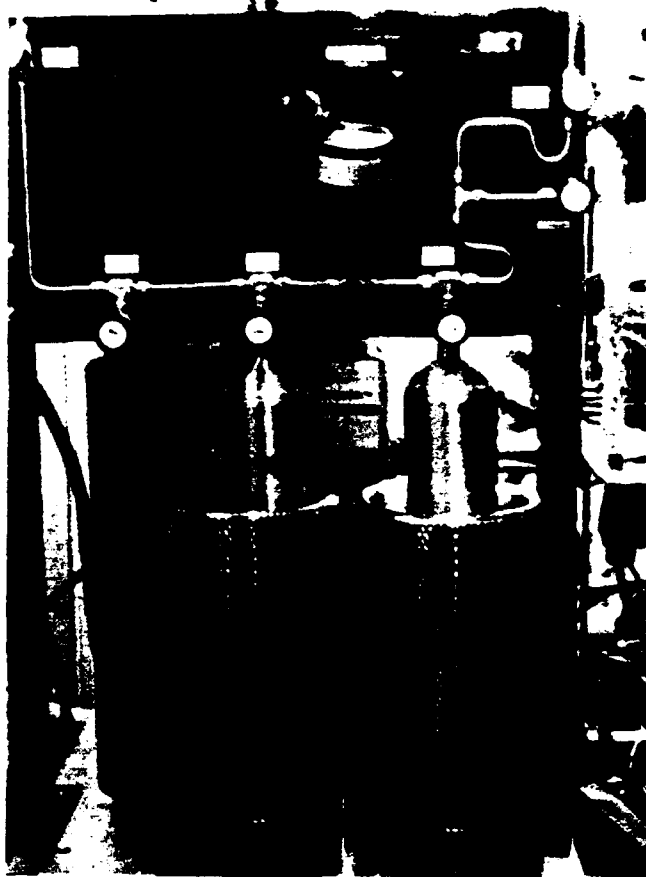


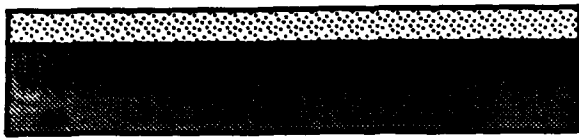
Figure 2. Cryogenic acetylene purifier.

Determine oxide etch rate.

3. Reactive Ion Etch, (RIE), oxidized Si wafer in SiF₄ and O₂ atmosphere to determine the oxide etch rate by measuring oxide thickness with ellipsometer before and after etch.
4. Spin photoresist onto remaining wafers.

Determine Si etch rate.

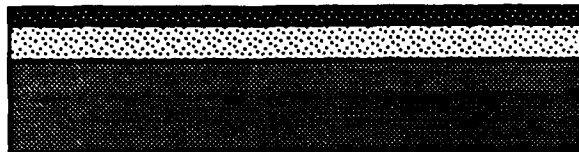
5. Using a standard mask and developing procedures, open large holes in photoresist on test wafer(s).
6. Use HF to remove exposed oxide.
7. Remove all remaining photoresist.
8. RIE test wafer.
9. Measure etched depth with Alphastep profilometer to get Si etch rate. The Si etch rate combined with the oxide etch rate will give the etch selectivity.



RCA clean and oxidize all wafers.



RIE test wafer(s) to find oxide etch rate.



Spin photoresist onto all oxidized wafers.



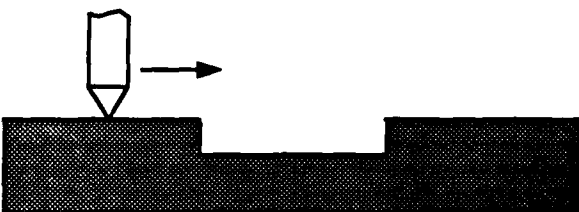
Open large holes in photoresist using a standard mask.



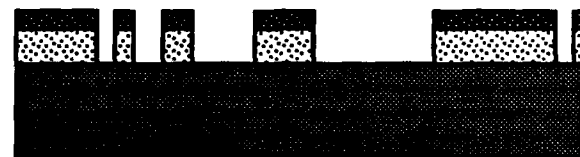
Remove exposed oxide and then photoresist.



RIE wafer.



Remove oxide and measure etch depth for Si etch rate.



Pattern remaining wafers with custom mask to make a series of openings. Remove exposed oxide and then remaining photoresist.



RIE patterned wafers and remove remaining oxide.



Reoxidize trenched wafers for passivation.

Figure 3. Preparation of trenched Si(100) wafers.

Process remaining wafers.

10. Pattern and develop remaining wafers with custom mask to produce a set of openings 2.5, 5, 10, and 20 μm wide.
11. Use HF to remove exposed oxide.
12. Remove all remaining photoresist.
13. RIE wafers taking care to stop before going through all of the oxide.
14. Use HF to remove the remaining oxide.
15. Grow thin oxide (<500 \AA) on trenched wafers for passivation.

Doping Films. Concurrently to determining the deposition uniformity, work will proceed in developing techniques to dope the ALE films. The p-type dopant employed will be aluminum from a triethylaluminum bubbler while the n-type dopant will be nitrogen supplied by ammonia. Characterization will employ the techniques of Hall mobility measurement and 4-point probe sheet resistivity determination in addition to SIMS analysis.

C. Results

Silicon wafers have been collected for producing the trenched substrates. The custom mask has been designed and ordered. Preliminary work with p-type doping of ALE deposited SiC films is underway but inconclusive at this point.

D. Future Research Plans and Goals

The immediate plans in this facet of the research initiative on this project are to pursue the stated goals outlined in this report. Once the trenched wafers are produced, a series of experiments will be carried out to explore the reaction of the material system to variations in processing parameters. This series will be aimed at developing run parameters that optimize film uniformity and deposition rate.

Once the ability to reliably dope films has been developed, diodes will be constructed for I-V analysis. As we are developing the ability to dope n and p-type, junctions in deposited films, as well as heterojunctions with n- and p-type Si substrates and n-type α (6H)-SiC substrates, will be producible. Study and development of p/n junctions formed by ALE will be an ongoing task of this research.

E. References

1. W. von Muench and I. Pfaffender, *J. Appl. Phys.* **48**, 4831 (1977).
2. W. von Muench and E. Pettenpaul, *J. Appl. Phys.* **48**, 4823 (1977).
3. N. W. Jepps and T. F. Page, "Polytypic transformations in silicon carbide" in *Progress in Crystal Growth and Characterization, Vol. & Crystal Growth and Characterization of Polytype Structures*, P. Krishna, Ed., Pergamon, NY, 1983, pp. 259-307.
4. E. A. Bergemeister, W. von Muench, and E. Pettenpaul, *J. Appl. Phys.* **50**, 5790 (1979).

5. Y. Fujii, K. Furukawa, A. Suzuki and s. Nakajima, Abstracts Autumn Meeting Japan. Soc. Appl. Phys., 328, 1990.
6. J. J. Sumakeris, L. B. Rowland, R. S. Kern, S. Tanaka and R. F. Davis, *Thin Solid Films* **225**, 219 (1993).
7. J. Sumakeris, Z. Sitar, K. S. Ailey-Trent, K. L. More and R. F. Davis, *Thin Solid Films* **225**, 244 (1993).

VIII. High Resistivity LT GaP and InGaP Films Grown by Gas Source Molecular Beam Epitaxy (GSMBE)

A. Introduction

GaAs buffer layers grown at low temperatures (LT) by molecular beam epitaxy (MBE) have received a great deal of attention as excellent alternative buffer layers to eliminate sidегating (or backgating) effects in the GaAs field-effect-transistor-based integrated circuits [1] and as insulators for high power GaAs MISFETs [2]. These new materials, usually grown at 200°C, exhibit good crystalline quality and extremely high resistivity, and thus can provide excellent device isolation. The latter is due to the excess arsenic incorporation (~1 at.%) in the layers leading to densities as high as $5 \times 10^{18} \text{ cm}^{-3}$ of As-antisite defects [3]. Annealing these materials or proceeding with the growth at a normal MBE growth temperature (600°C) causes the excess arsenic to form precipitates as indicated from transmission electron microscopy (TEM) studies [4].

Since the success of LT GaAs material, investigations have been extended not only to the LT growth of other As-based III-V compounds such as LT AlGaAs [5] and LT InAlAs [6], but also to the LT growth of P-based materials such as LT InP [7]. However, little work has been reported on LT GaP and InGaP films even though these LT films, all having a wide bandgap, are promising for device applications. In addition, LT InGaP can be extremely useful for some devices since it can be grown lattice matched to GaAs substrates. An immediate question raised on these LT films is whether excess phosphorus and phosphorus precipitates can exist and exhibit the similar properties as their arsenic counterpart. Previous efforts for LT InP did not yield semi-insulating films [8]. In this paper, we report, for the first time, on the growth and characterization of LT GaP and InGaP films by GSMBE.

B. Experimental Conditions

All the epilayers presented in this work were grown in a Riber 32RD GSMBE system. Semi-insulating (SI) GaP and GaAs (100) substrates were used for LT GaP and LT InGaP, respectively. The substrates were degreased, etched and then mounted on the Mo blocks with In solder. Elemental Ga and In sources and 100% PH₃ thermally cracked at 900–950 °C were used to grow these films. The growth chamber pressure was maintained in the 10⁻⁵ Torr range using a turbomolecular pump. The growth temperature cannot be accurately determined in our system and was estimated according to our previous calibrations using the oxide desorption temperature of GaAs (580°C) as a reference. The thermocouple reading is 60–80 °C lower than this reference temperature. Temperatures quoted in this report are the corrected values rather than the thermocouple readings. The growth rates of all GaP and InGaP epilayers were 1 and 0.5 μm/h, respectively.

The GaP and GaAs substrates were all heated at 630°C for ~5–10 min under PH₃ or AsH₃ overpressure for oxide removal before growth of GaP or InGaP films, respectively. In the case of LT GaP, several approaches were applied to the growth of LT films. When films were grown for electrical evaluations, the substrate temperature was lowered directly to the desired low temperature followed by the growth of a GaP layer (~2 μm). For structural characterization, a GaP buffer layer was grown first at 560°C followed by the LT film. GaP films were also grown at high temperature (560°C) as a reference for both the electrical and structural characterizations.

Reflection high energy electron diffraction (RHEED), cross-sectional transmission electron microscopy (XTEM), and double-crystal x-ray diffraction (DCXRD) were used to assess the crystal quality of the LT GaP and InGaP films. The *in situ* RHEED showed a streaky pattern, indicating crystalline growth of the LT InGaP films. Besides, the ultra-high resolution scanning transmission electron microscopy (STEM) was used to obtain the stoichiometry data from LT InGaP samples. All the samples used in this report had a mirror-like morphology. The resistivities of LT GaP films and the GaP substrate were obtained from the van der Pauw technique while those of LT InGaP films and the GaAs substrate from temperature-dependent Hall measurements.

C. Results and Discussion

LT GaP. TEM Analysis. LT GaP films grown at temperatures lower than 160°C were poly-crystalline as demonstrated by both the RHEED pattern and the TEM diffraction pattern. Increasing the growth temperature by ~30°C resulted in a streaky RHEED pattern and single-crystal films, as confirmed by TEM. Figure 1 shows a cross-sectional TEM dark field micrograph of multilayers of GaP epitaxial films taken under the two beam condition $g=400$ ($g,-g$). This structure has a 0.4 μm GaP buffer layer grown at 560°C, followed by a LT GaP layer grown at about 210°C (1 μm). The growth temperature was then decreased further by ~20°C without interrupting the growth to grow a second LT layer of the same thickness. All layers are single crystalline as indicated from the electron diffraction pattern. The LT films show a contrast from the one grown at high temperature which can be attributed to excess phosphorus in the lattice resulting from a deviation from stoichiometry [9]. One may also observe in Fig. 1 the presence of contrast modulations near the interface between the two LT GaP layers. This can be due to the substrate temperature fluctuations resulting from the 20°C decrease.

Using conventional imaging techniques, TEM studies on annealed samples did not show any incoherent phosphorus precipitation with defined boundaries. However, high-resolution TEM on the annealed films revealed the presence of regions having different phase contrast which suggests coherent precipitation. These coherent precipitates, indicated by the arrow in

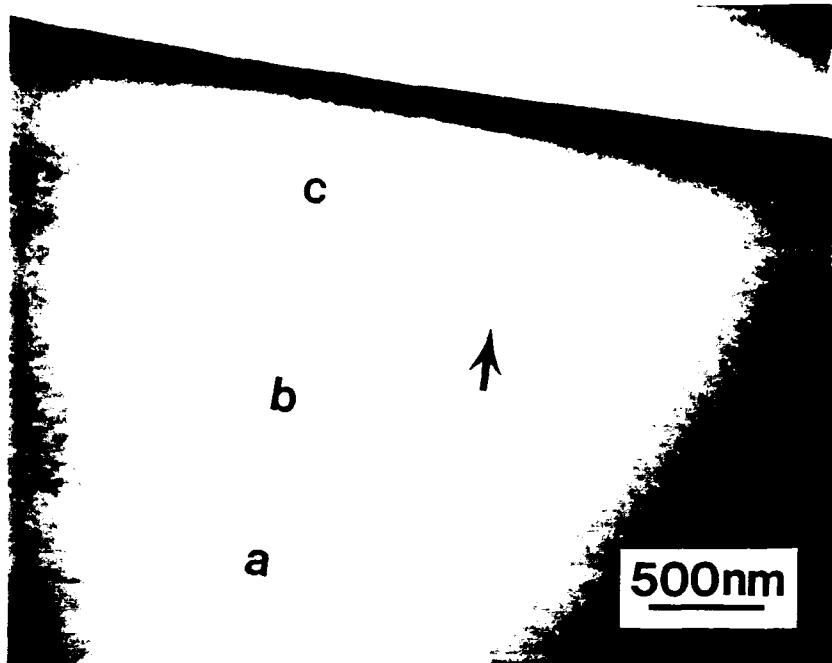


Figure 1. Cross-sectional TEM micrograph of a multilayered structure containing: (a) GaP buffer layer grown at 560°C (HT), (b) LT GaP film (1 μm) grown at 210°C and, (c) LT GaP layer (1 μm) grown at 190°C. The arrow indicates the transition region between the two LT GaP films. The contrast between LT GaP films and HT GaP film might be due to the excess phosphorus in LT films.

Figure 2(a), may become incoherent and demonstrate a phase boundary after prolonged annealing. To compare the current observations with LT arsenic-based films, a GaAsP film was grown at 200°C. The composition of this ternary alloy was determined by DCXRD to have 20% GaP (after annealing). TEM studies of this annealed LT GaAsP show pronounced incoherent arsenic precipitates as illustrated in Figure 2(b). The precipitates have been segregated to the dislocation lines and microtwin boundaries.

X-ray Diffraction. High-resolution x-ray diffraction results were obtained with a Bede 200 double-crystal diffractometer. Films grown at high temperatures show only one diffraction peak from (113) reflection planes [Figure 3(a)]. For the LT growth, two (113) reflections were observed: a substrate reflection and an epilayer reflection with a lower intensity at a lower Bragg angle, as indicated in Figure 3(b). The angular separation ($\Delta\theta$) is about 220 arc sec. Splittings as low as 40 arc sec were also observed. The splitting can be attributed to the strain in the epilayer resulting from excess phosphorus, possibly in the interstitial sites of the GaP crystal lattice, causing lattice dilatation. This splitting ($\Delta\theta$) in the DCXRD seems to increase with lower growth temperatures. Both the splitting and the change in the lattice constant in these LT GaP films are not as high as that reported for LT GaAs [10] films. This can be explained by the relative size of the arsenic and phosphorus atoms located at interstitial sites. Annealing of these LT GaP samples was carried out in a metalorganic

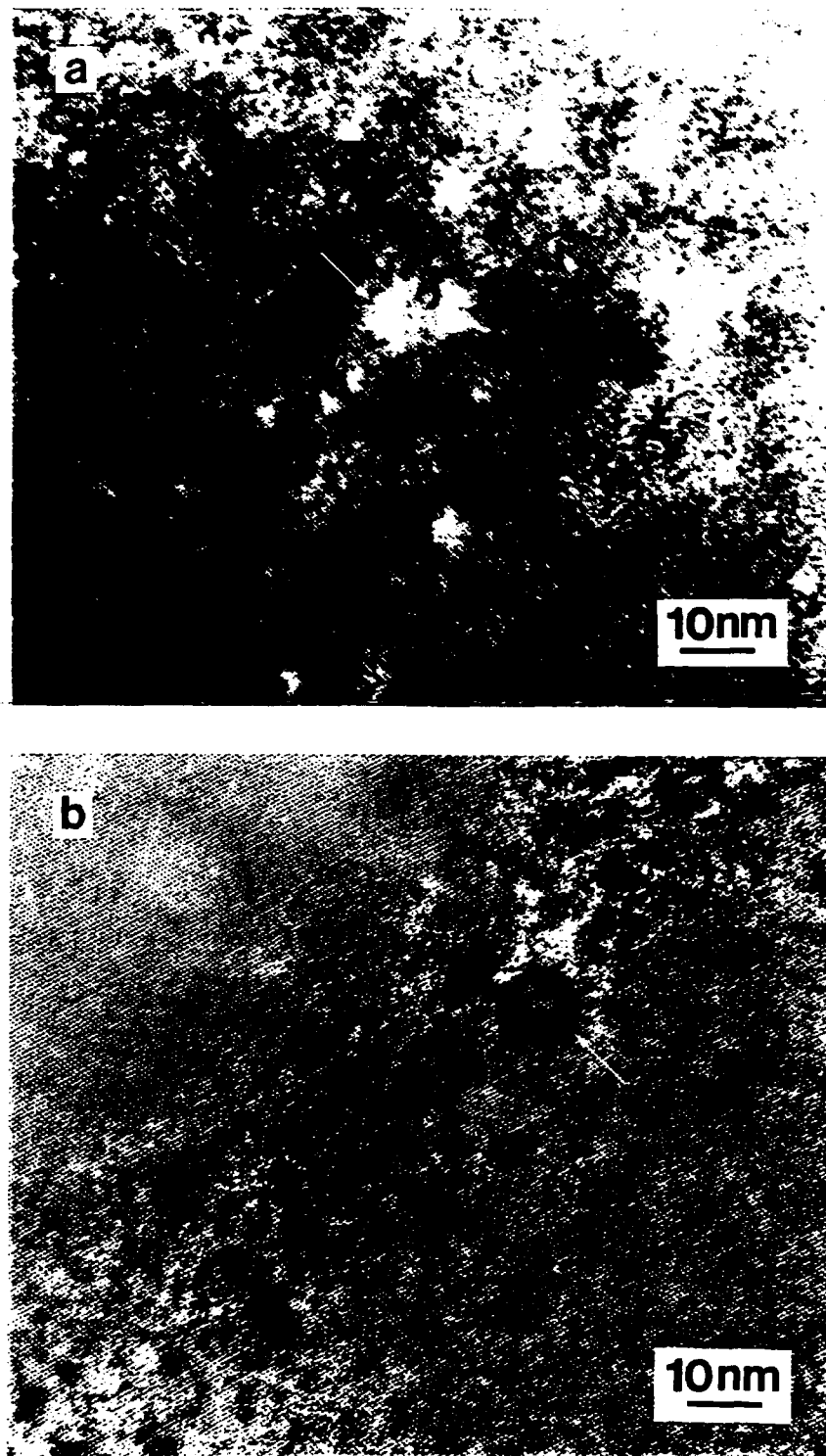


Figure 2. Cross-sectional TEM micrographs of: (a) annealed (at 650°C for 60 min) LT GaP film grown at 190°C on GaP substrate (the arrow indicates one of the coherent precipitates appearing as bright dots), (b) LT GaAsP film grown at 200°C on GaAs substrate and annealed at 650°C for 60 min (the arrow indicates a large arsenic precipitate which is surrounded by small arsenic precipitates appearing as black dots).

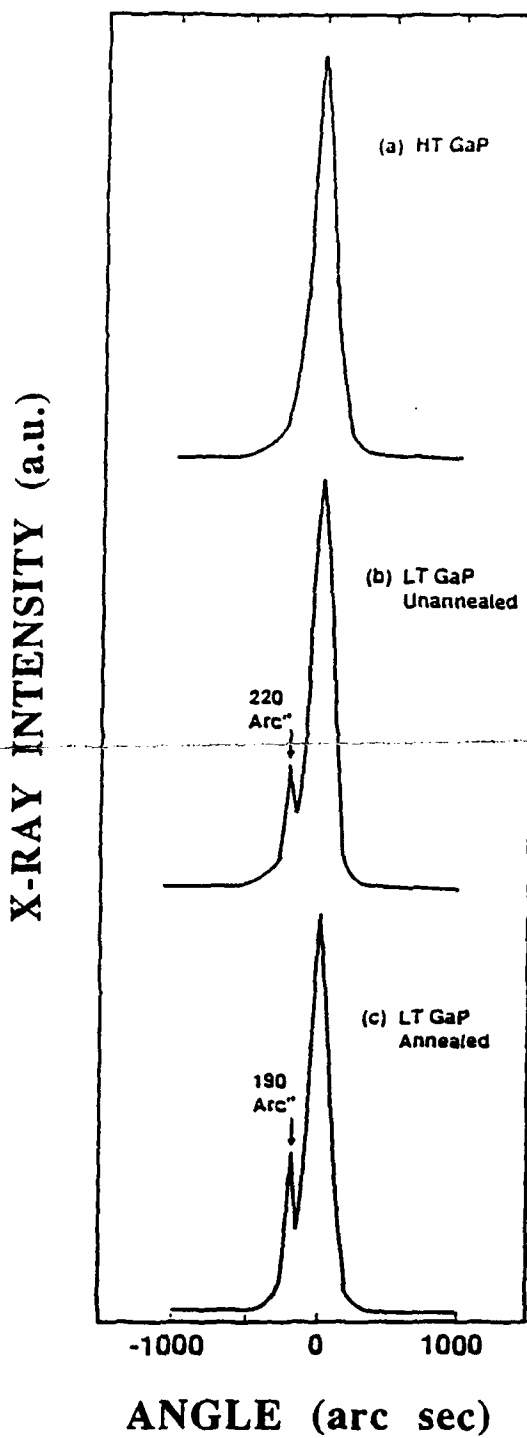


Figure 3. Double crystal x-ray diffraction from the (113) planes of: (a) GaP film grown at 560°C on GaP substrate, (b) LT GaP grown at 200°C and unannealed and, (c) LT GaP grown at 200°C and annealed at 700°C for 60 min.

chemical vapor deposition (MOCVD) reactor with PH₃ overpressure at 650 and 700 °C for 30–60 min. Annealing did not result in the complete disappearance of the lattice expansion; however, a slight reduction in $\Delta\theta$ (~30 arc sec) was observed due to the high annealing

temperature [Figure 3(c)]. We have not yet detected any consistent pattern of the effect of annealing on the splitting in the DCXRD as related to the growth temperature and the crystallinity. Further studies are currently underway.

Resistivity Measurements. Resistivity measurements were carried out with a high-impedance van der Pauw apparatus at Wright State University. In-dots alloyed at 300°C were used as contacts to the epilayers. The as-grown LT GaP (190°C) showed a resistivity of about $10^8 \Omega \text{ cm}$. The resistivity of the sample annealed at 700°C for 60 min could not be measured in darkness, however, with intense light a resistivity of $10^6 \Omega \text{ cm}$ was obtained. The resistivity of the SI GaP substrate was also too high to be measured in the dark, but had a resistivity about $10^8 \Omega \text{ cm}$ when measured under intense light. Other samples have shown resistivity in the 10^6 – $10^8 \Omega \text{ cm}$ range depending on the growth temperature. GaP films grown at high temperature showed low resistivities. Detailed electrical characterization of these LT GaP films will be reported elsewhere. The high resistivity of LT GaP is probably mainly due to excess phosphorus related defects.

Device Application. Since it is highly resistive, the strained LT GaP film could be used as an excellent passivation layer in GaAs MESFETs. Then, the gate-drain breakdown voltage (V_{BD}) of the MESFETs could be improved greatly. This has been confirmed in our lab. The details will be published elsewhere [15].

LT InGaP

X-ray Diffraction. DCXRD showed that the LT InGaP films had ~47% In. Two LT structures were grown in this work for structural characterization of LT InGaP films. The first structure had only a single LT InGaP layer (200°C, 1.5 μm) grown on a GaAs buffer layer (550°C, 80 Å). Two Bragg peaks were observed for the DCXRD (400) reflection with the epilayer peak located at a higher Bragg angle than the substrate peak, as shown in Fig. 4(a). This indicates that the LT InGaP film is not lattice matched to the GaAs substrate and its In composition is lower than the InGaP-GaAs lattice-matched composition of ~49%. The narrow full width at half maximum (FWHM) of the epilayer peak (20 arc sec) indicates the high quality of the crystalline epilayer. Annealing this sample at 600°C for 1 hr caused the angular separation between the epilayer and the substrate peaks to increase by 20 arc sec, as seen in Fig. 4(b). This observation indicates a slight reduction of the lattice parameter of the epilayer after annealing. As to the lattice relaxation as a result of annealing, this is similar to the LT GaAs case. It has been reported that annealing LT GaAs at 600°C for ~10 min results in a complete removal of the lattice mismatch. Annealing LT InGaP at the same temperature for 1 hr, however, results in only slight relaxation of the expanded lattice. This is manifested by a small peak shift of the annealed film to a higher Bragg angle. In order to compare the structural properties of the LT InGaP and the InGaP epilayers grown at higher temperatures

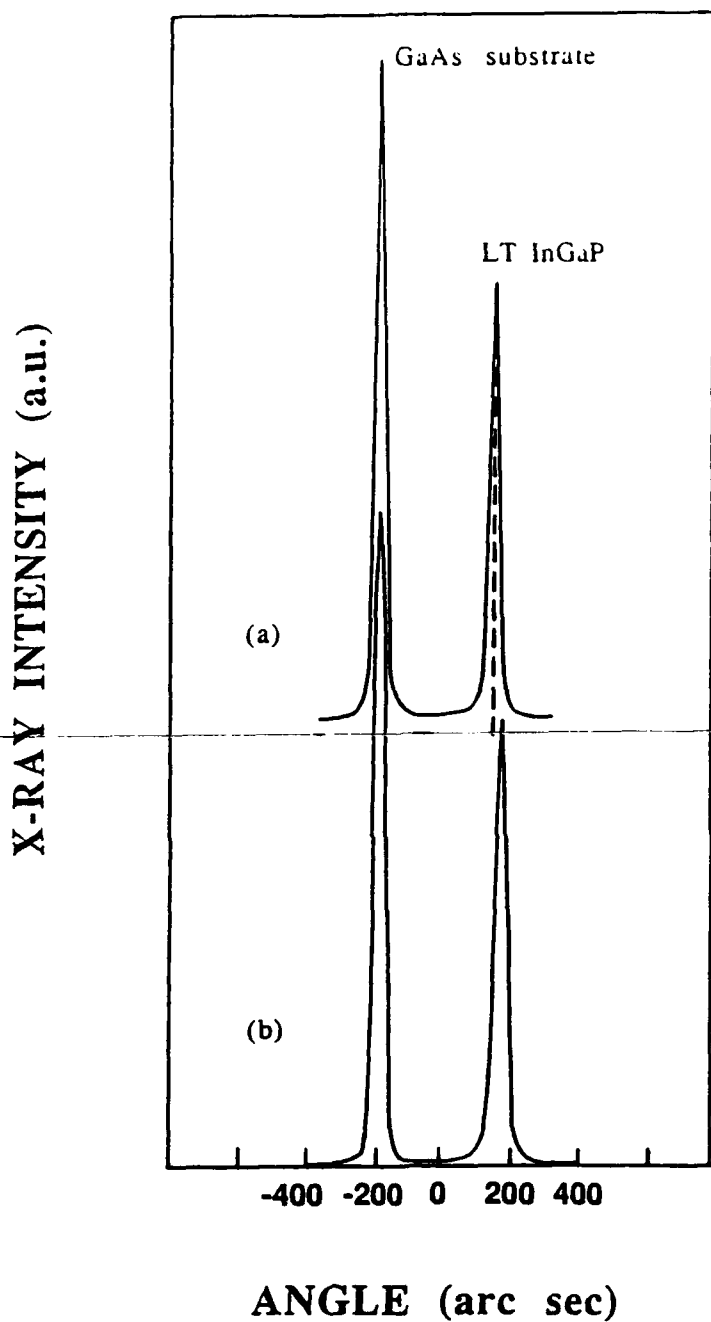


Figure 4. DCXRD from (400) reflection planes of the first structure described in the paper: (a) as-grown and, (b) annealed at 600°C for 1 hr. The LT InGaP peak was shifted to higher Bragg angle by 20 arc sec after annealing.

(~480°C, hereafter referred to as HT InGaP), a second structure was grown, as shown in Fig. 5. During the growth of both HT and LT InGaP epilayers, a fixed PH₃ flow rate of ~4 sccm was maintained. It should be noted that there was an interruption of the PH₃ flow into the growth chamber after the HT growth was ended and the substrate temperature was

LT InGaP	200°C	1 μm
HT InGaP	480°C	1 μm
GaAs buffer	550°C	1 μm
SI LEC GaAs (100) substrate		

Figure 5. Schematic of the multilayer sample with the LT InGaP film grown on top of the HT InGaP film.

lowered to ~300°C. The In compositions of the LT and HT InGaP epilayers were assumed to be identical by maintaining the same source temperatures during the layers' growth. DCXRD analyses from (400) reflection planes were performed on both the as-grown and annealed samples. For the as-grown samples, three (400) Bragg peaks were observed: the substrate, LT InGaP and HT InGaP peaks, respectively, as shown in Figure 6(a). Upon annealing at 600°C for 1 hr the LT peak was found to be the only one shifted, as shown in Fig. 6(b). The observation that the annealing did not have any effect on the HT peak position was as expected. The angular separation between the LT and HT InGaP reflections was 70 arc sec before annealing and 50 arc sec after annealing. Therefore, the angular shift of the LT peak towards the HT peak after annealing was 20 arc sec, which was in good agreement with that of the first grown structure previously discussed. This relative shift, corresponding to the incomplete removal of the lattice-mismatch by 0.01%, might be caused by redistribution of the excess P atoms in the epilayer lattice due to the annealing. The nature of the redistribution is not yet known at this time. Considering the HT InGaP as a "substrate," the LT InGaP/HT InGaP structure was found to have DCXRD characteristics similar to those of LT GaP/GaP discussed before. The fact that the LT peak was situated on the left side of the HT peak confirmed that the LT InGaP had a slightly larger lattice parameter than that of the HT InGaP (by 0.05% for the as-grown LT epilayer). This lattice expansion can be explained by the presence of the excess P incorporated into the epilayer due to the nonstoichiometric growth.

TEM Analysis. An XTEM micrograph (Figure 7(a)) from the second structure indicates the presence of phase separation in LT InGaP epilayers. This is manifested in the form of a "precipitate-like" microstructure. The precipitate-like phase separation (~800 Å in diameter for the layer grown at ~200°C) appears to decrease in volume as the growth temperature increases. Annealing, however, seems to have a slight influence on the phase separated

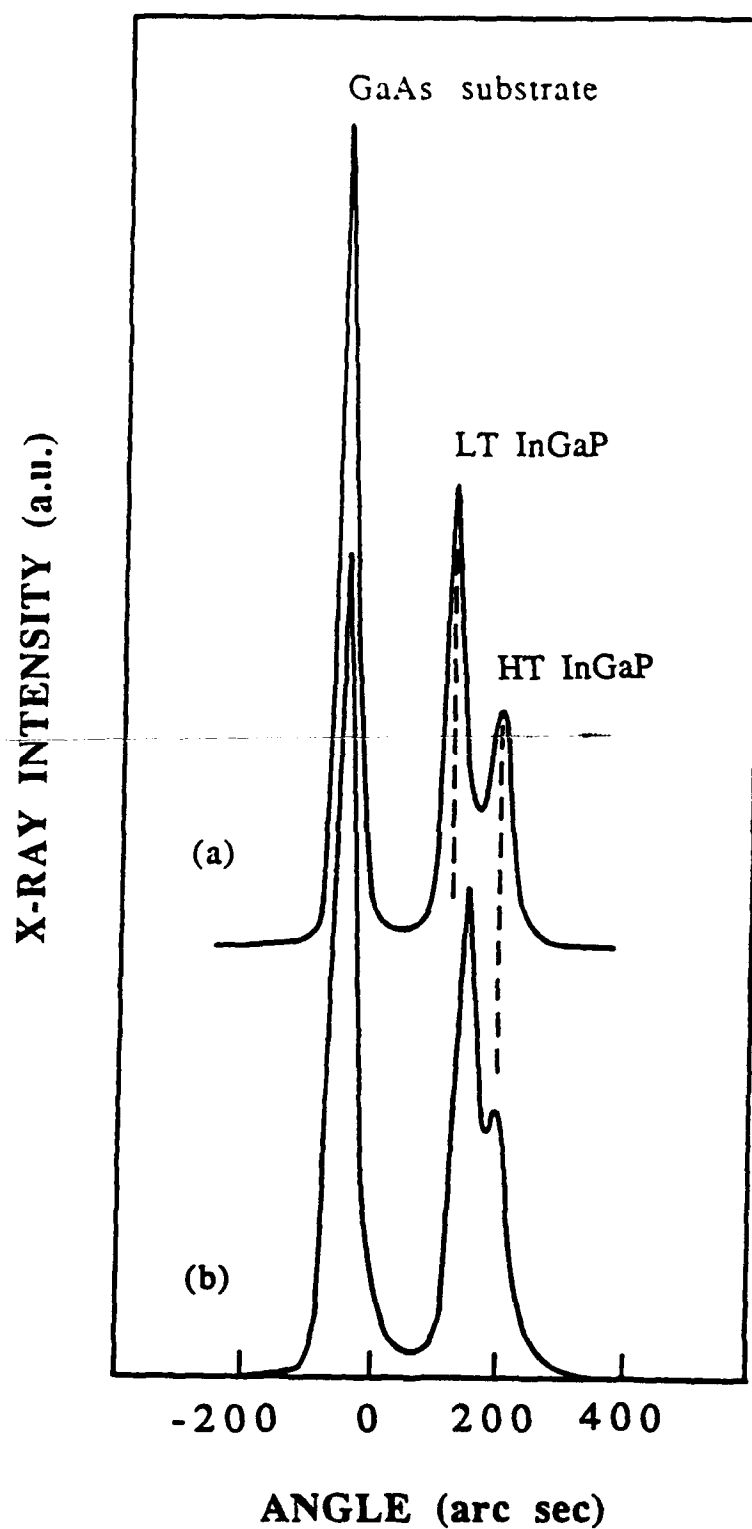


Figure 6. DCXRD from (400) reflection planes of the sample shown in Figure 5: (a) as-grown, the angular separation between the LT InGaP and the HT InGaP reflections is 70 arc sec; (b) annealed at 600°C for 1 hr, the angular separation between the LT InGaP and the HT InGaP reflections is 50 arc sec.

**THIS
PAGE
IS
MISSING
IN
ORIGINAL
DOCUMENT**

page 59

microstructure. The phase separated areas were crystalline and strained as implied by the moire fringes shown in Figure 7(b). Analytical STEM analyses performed on the LT InGaP indicated a slightly higher In composition in the phase separated areas relative to the matrix. The HT InGaP showed a distinctive feature of slight decomposition. The decomposition in the HT InGaP, as well as the phase separation in the LT InGaP, might be explained by the spinodal decomposition usually observed in liquid phase epitaxy (LPE) and MOCVD growth. Spinodal decomposition causes the appearance of a two-phase microstructure with different In compositions at the growth temperature.

STEM Analysis. We have investigated the LT InGaP group-V nonstoichiometry by using the analytical STEM approach. The structure shown in Fig. 5 was chosen to measure the small changes of P-concentration in the LT InGaP. The HT InGaP epilayer served as a reference for the LT InGaP epilayer. The analysis was performed in a TOPCON EM-002B ultra-high resolution analytical electron microscope equipped with an electron probe. The TEM facility was operated at 200 KV with the probe diameter set at 5.1 nm throughout the analysis. Several data points were taken by setting the electron probe at different locations within one layer for the analysis to be statistically accurate. The values of atomic percentage phosphorus thus obtained were averaged numerically to obtain the final result for the same epilayer. This method was employed for both HT and LT InGaP epilayers. The analysis on the sample chosen above determined that the LT InGaP had 0.5 at.% more P atoms than the HT InGaP. These excess atoms incorporated in the LT InGaP epilayer probably caused the lattice mismatch compared to the HT InGaP epilayers.

Calculation of Excess P. For verification of the excess P results, the lattice mismatch as determined by DCXRD was used to calculate the excess P incorporated in the lattice. In this approach, the lattice mismatch of the as-grown LT InGaP with respect to the HT InGaP was used to obtain the increase of the volume of the LT InGaP crystal lattice, ΔV , assuming the lattice was uniformly elastically distorted. Although this assumption may not be exact, this approach can be a good estimate since the two measured lattice parameters, namely, the perpendicular (a_{\perp}) and the parallel ($a_{//}$) referenced to the (100) plane, were fairly close if not identical. We also made the assumption that all the excess P atoms were incorporated in the interstitial positions of the LT InGaP lattice. Since both Ga and In atoms have larger atomic radii than that of P atom (1.81, 2.0 and 1.23 Å, respectively) [11], the excess P atoms can be neither on Ga nor on In substitutional positions. If that were not the case, then there would be a lattice contraction instead of the lattice expansion exhibited by the LT InGaP epilayer. The above assumptions led to a simple model in which an excess P atom acted as a misfitting particle in a uniform matrix. Let ϵ be the elastic strain of the LT InGaP lattice induced by the incorporation of the excess P atoms and δ the conventional lattice mismatch between the HT

and LT InGaP lattices. The two parameters ϵ and δ are related by the Bullough and Newman equation [12]:

$$\epsilon = \delta(1+v)/[3(1-v)],$$

where v is Poisson's ratio. Note that $v=1/3$ for almost all III-V semiconductors. Therefore, the ϵ - δ relation can be simplified as $\epsilon=(2/3)\delta$. Let δ_{mv} denote the measured value of the lattice mismatch by DCXRD, i.e., $\delta_{mv}=(a_{LT}-a_{HT})/a_{HT}$ by definition, where a_{LT} and a_{HT} are the lattice parameters of the as-grown LT InGaP and HT InGaP epilayers, respectively. In theory, this measured value δ_{mv} is composed of the elastic strain ϵ and the conventional lattice mismatch δ , i.e., $\delta_{mv}=\epsilon+\delta$. Substituting the simplified ϵ - δ relation into the above equation and solving for δ gives $\delta \approx (3/5)\delta_{mv}$. Given $a_{LT}=5.64639$ Å and $a_{HT}=5.64345$ Å as determined by DCXRD, the equation $\Delta V=(a_{LT})^3-(a_{HT})^3$ yields a value of 0.28105 (Å)³. The number of the excess P atoms per unit cell, ΔN_p , can be calculated from the equation $\Delta N_p = \Delta V/v_p$, where v_p is the volume of one P atom. Taking in consideration the elastic strain value (the δ - δ_{mv} relation), ΔN_p was corrected with the factor of $3/5$. The P atom, treated as a hard sphere, has a volume of $v_p=(4/3)\pi r_0^3$, where r_0 is the radius of the atom. Since normally there are four P atoms per unit cell, the excess P atoms per unit cell of LT InGaP can finally be calculated to be ~ 0.54 at.%. This result is in good agreement with that obtained from the analytical STEM.

Resistivity Measurements. The resistivity of a LT material serves as a practical monitor for its device applications. To measure the resistivity of LT InGaP more accurately, a special sample was designed. A 2-μm-thick LT InGaP film was grown at $\sim 200^\circ\text{C}$ on a 500-Å-thick AlAs layer grown at 610°C . The LT InGaP film was removed from the substrate by first mounting the sample face-down on a glass slide, then lapping and RIE-etching the substrate off, and finally removing the AlAs layer in HF. Hall effect measurements on the as-grown LT InGaP film revealed n-type conduction with a resistivity of 9×10^5 Ω cm and mobility of 120 cm²/V s at 296 K. To determine the activation energy of the dominant donor [13], we plotted $\ln(n/T^{3/2})$ vs. T^{-1} , as shown in Fig. 8. The slope of this plot, which is just $-E_{D0}/k$, leads to $E_{D0}=0.48$ eV, within error of what might be expected for the (0/+)-transition of the P antisite in $\text{In}_{0.5}\text{Ga}_{0.5}\text{P}$. After annealing the LT film at 600°C for 1 hr, the 296-K resistivity increased to 10^9 Ω cm but a Hall voltage could no longer be found. Nevertheless, a plot of $\ln(r)$ vs. T^{-1} , where r is the resistivity, produced an even larger activation energy, 0.8 eV. Thus, the material is stable against high-conductivity conversion. It is necessary to point out that the LT InGaP remains semi-insulating before and after annealing.

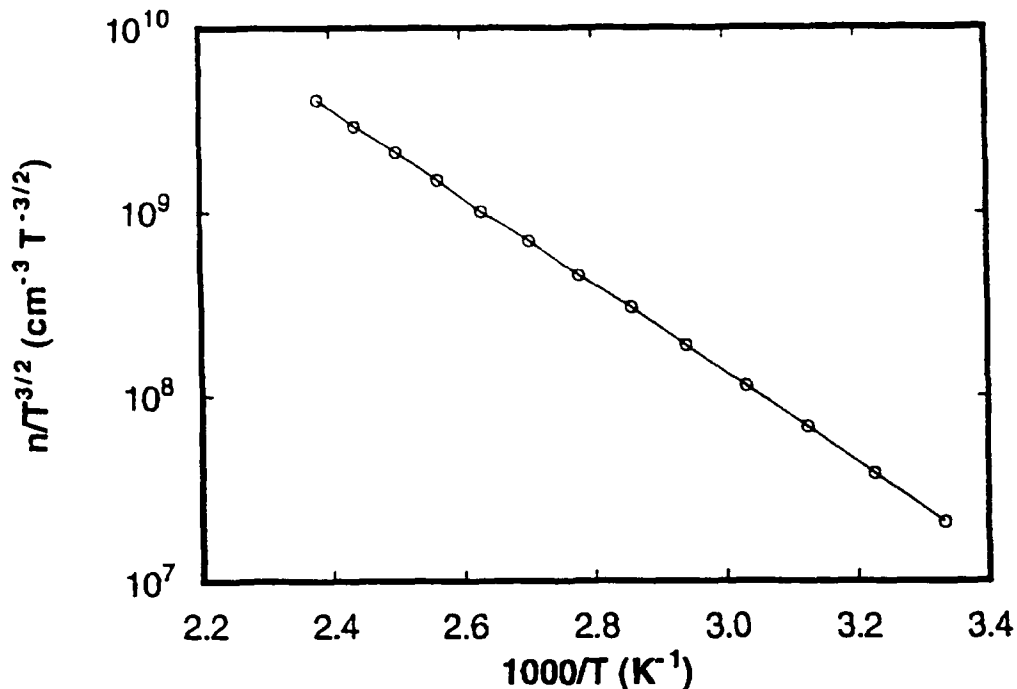


Figure 8. Plot of $\ln(n/T^{3/2})$ vs. T^{-1} for the as-grown LT InGaP film.

D. Conclusions

In conclusion, we have successfully grown GaP and $\text{In}_{0.47}\text{Ga}_{0.53}\text{P}$ at a low temperature of $\sim 200^\circ\text{C}$ for the first time. Both LT GaP and LT InGaP showed a lattice expansion of $\sim 0.05\%$, as determined by DCXRD. Unlike LT GaAs, annealing at high temperatures ($600\text{--}700^\circ\text{C}$ for 30–60 min) did not result in a total relaxation of the lattice strain, but a slight reduction of the lattice expansion. The lattice expansion can be explained by the incorporation of excess P atoms of up to 2.2 at.% in the LT GaP epilayer grown at 190°C [15] and ~ 0.5 at.% in the LT InGaP epilayer. The slight reduction of the lattice expansion after annealing may be caused by redistribution of the excess P atoms. XTEM showed no formation of P-precipitates after annealing, but did show coherent precipitation in annealed LT GaP epilayer and phase separation in as-grown LT InGaP epilayer. The latter was manifested in the form of a “precipitate-like” microstructure. This precipitate-like phase separation can be explained by the tendency of the InGaP alloys to spinodally decompose at similar compositions that are close to that which lattice matches GaAs. The HT InGaP film indicated the occurrence of slight spinodal decomposition at the growth temperature. Further structural investigation of the phase separation is currently underway. LT GaP (as-grown & annealed) is highly resistive with ρ up to $10^8 \Omega \text{ cm}$. The resistivity range is $10^8\text{--}10^6 \Omega \text{ cm}$ for LT GaP films grown at $T_s=190\text{--}230^\circ\text{C}$ range. The temperature-dependent resistivity and Hall measurements were performed on the LT InGaP film after the substrate was removed. The as-grown LT InGaP film showed a resistivity of $\sim 10^6 \Omega \text{ cm}$ at room temperature whereas the annealed film at

600°C for 1 hr exhibited at least three orders of magnitude higher resistivity. Activation energies of ~0.5 and 0.8 eV were also obtained from the Hall measurements for the as-grown and annealed LT InGaP films, respectively.

The above preliminary studies show that both LT GaP and LT InGaP films do not exactly follow the observed trends for LT GaAs films. Annealing the LT GaAs films caused lattice strain to disappear and arsenic precipitation accompanied by high resistivity films. However, in LT GaP and LT InGaP, annealing is not necessary to achieve high resistivity. The current LT GaP and LT InGaP results imply that the high resistivity is not a result of the presence of precipitates and the accompanying carriers depletion near the metal phosphorus semiconductor interfaces as in the case of LT GaAs [14]; but, rather is a result of deep levels associated with the excess phosphorus present in these LT films. This result, however, is not consistent with that previously reported on LT InP films, where both phosphorus precipitates and low resistivity films were observed [8]. Thus, it seems that more work is needed in the LT growth of phosphorus-based compounds to settle such issues.

E. Future Research Goals

LT GaP. GaP has a wide bandgap of 2.27 eV at room temperature, a high Schottky barrier of 1.3 eV for Au/GaP, and no surface Fermi level pinning. These properties are promising for device applications. Although the strained LT GaP film used as a passivation layer in GaAs MESFETs has been known to improve the device greatly with higher breakdown voltage, more work is required for further characterization of the device application of LT GaP. In addition, critical layer thickness (CLT) of LT GaP on GaAs, which is of importance for the device application, needs to be determined.

A variety of Si devices could be made possible if the highly resistive, high quality crystalline LT GaP can be grown on Si substrate successfully. Therefore, growth of LT GaP on Si is worth being given great efforts.

LT InGaP. InGaP can be grown lattice-matched to GaAs and has a relatively wide bandgap (1.92 eV) with ~49% InP composition. Furthermore, InGaP can be selectively etched to the extent of 100%. Having all these properties, the highly resistive LT InGaP can have a variety of important device applications with some of the examples given below. It can be used as a gate insulator in GaAs MISFETs. It can also be used to make a pico-second photodetector if LT InGaP has very short carrier lifetime. Therefore, further investigation is necessary for the fabrication and characterization of LT InGaP/GaAs related devices.

F. References

1. F. W. Smith, A. R. Calawa, C.-L. Chen, M. J. Manfra, and L. J. Mahoney, IEEE Electron Device Lett. **9**, 77 (1988).

2. L. W. Yin, Y. Hwang, J. H. Lee, R. M. Kolbas, R. J. Trew, and U. K. Mishra, IEEE Electron Device Lett. **11**, 12 (1990).
3. M. Kaminska, E. R. Weber, Z. Liliental-Weber, and R. Leon, J. Vac. Sci. Technol. B **7**, 710 (1989).
4. M. R. Melloch, K. Mahalingham, N. Otsuka, J. M. Woodall, and A. C. Warren, J. Cryst. Growth **111**, 39 (1991).
5. J. N. Miller and T. S. Low, J. Crystal Growth **111**, 30 (1991).
6. R. A. Metzger, A. S. Brown, W. E. Stanchina, M. Lui, R. G. Wilson, T. V. Kargodorian, L. G. McCray, and J. A. Henige, J. Crystal Growth **111**, 445 (1991).
7. J. Ch. Garcia, J. P. Hirtz, P. Maurel, H. J. Von Bardeleben, and J. C. Bourgoin, Mat. Res. Soc. Symp. Proc. **241**, 277 (1992).
8. G. N. Maracas, K. T. Shiraliagi, R. A. Puechner, F. Yu, K. T. Choi, J. S. Bow, R. Ramamurty, M. J. Kim, and R. W. Carpenter, Materials Research Society (MRS) Fall Meeting, Boston, Dec. 1991.
9. M. Kaminska, Z. Liliental-Weber, E. R. Weber, T. George, J. B. Kortright, F. W. Smith, B. Y. Tsaur, and A. R. Calawa, Appl. Phys. Lett. **54**, 1881 (1989).
10. Z. Liliental-Weber, W. Swider, K. M. Yu, J. Kortright, F. W. Smith, and A. R. Calawa, Appl. Phys. Lett. **58**, 2153 (1991).
11. "Table of Periodic Properties of the Elements" published by Sargent-Welch Scientific Company.
12. R. Bullough and R. C. Newman, Rep. Prog. Phys. **33**, 101 (1970).
13. D. C. Look, *Electrical Characterization of GaAs Materials and Devices* (Wiley, New York, 1989), p.117.
14. A. C. Warren, J. M. Woodall, J. L. Freeouf, D. Grischkowsky, D. T. McInturff, M. R. Melloch, and N. Otsuka, Appl. Phys. Lett. **57**, 1331 (1990).
15. J. Ramdani, Y. He, N. El-Masry, and S. M. Bedair, to be published.

IX. Layer-by-layer Deposition of III-V Nitrides Using an Atomic Layer Epitaxy Reactor Design

A. Introduction

The potential semiconductor and optoelectronic applications of III-V nitrides has prompted significant research in thin film growth and development. The materials of concern in this section are GaN, currently, and other III-V nitrides, for upcoming studies. Because GaN is in the wurtzite structure with a bandgap of 3.4 eV [1] forms continuous solid solutions with both AlN and InN, for example, which have bandgaps of 6.2 eV [2] and 1.9 eV [3], respectively, engineered bandgap materials could result in optoelectronic devices active from the visible to deep UV frequencies [4].

Initial attempts at ALE deposition have been suspended in favor of the more realistic layer-by-layer deposition approach. This decision was supported by metalorganic decomposition data and by actual experimentations completed thus far. Like ALE, the layer-by-layer technique deposits one monolayer of material per cycle. However, the growth rate is highly dependent on the metalorganic (MO) flux and the exposure time under the MO gas. Thus unlike ALE, the process is not self-terminating after the deposition of one monolayer.

To produce films using the layer-by-layer approach an ALE reactor design has been implemented. The equipment and experimental procedures used for the process have been discussed in an earlier report. Therefore, only modifications to the experimental procedure, new results to date, conclusions and plans for future work will be included here.

B. Experimental Procedure

The ALE reactor design being used utilizes a continuously rotating susceptor arrangement. Thus as the susceptor rotates, the substrate is alternately exposed to the me MO gas, the H₂ curtain gas and the nitrogen source gas (i.e. ammonia: NH₃) in a constant cycle. There are two growth zones per cycle: one for the column-III species and one for the column-V species. For layer-by-layer growth, one cycle will result in one monolayer of film growth.

Unlike earlier work in which rotation began from under the H₂ inlet line before the MO inlet line, recent experiments have begun with initial exposure to ammonia. Before the substrate sweeps under the ammonia inlet line, the W-filament used in cracking the ammonia into elemental hydrogen and nitrogen should be stabilized at the desired “cracking” temperature. The nitrogen source was chosen as the starting species because it was believed that initial exposure to the MO precursor was possibly aiding in the faceted growth being observed by not uniformly covering the substrate surface. It was believed that more uniform coverage would result from this and instigate the desired uniform growth. This step will be termed “nitrogenating” the substrate surface. Thus, prior to the exposure to any TEG, the substrate

was nitrogenated for 5 seconds at the start of the run. Similarly, at the end of the run the deposited film was nitrogenated for 5 seconds after the flow of TEG had been terminated.

Also in an attempt to reduce the faceted surfaces of the deposited films, the growth temperature was lowered from 640°C used in earlier runs to 500°C. By reducing the temperature, the surface mobility is reduced. Hopefully this reduction would result in a more uniform deposition and less atomic migration to the more preferred nucleation sites resulting in the undesired faceted growth.

Once rotation and deposition begins, several system variables must be monitored. They include cooling water flow, all gas flow rates, system and MO bubbler pressures, susceptor and W-filament temperatures, and rotation speed. Under normal operating procedures, these variables remain nearly constant, but because of their obvious importance, they must be monitored to maintain deposition uniformity. Table I below lists the system parameters for various deposition runs.

Table I. Deposition Parameters

System Variables	#10	#13	Run # #14	#15	#16
Substrate	Si C*	Si C**	Si C**	SiC **	SiC **
Initial Press.	1×10 ⁻⁵ torr	1.2×10 ⁻⁵	1.2×10 ⁻⁵	1.2×10 ⁻⁵	1.8×10 ⁻⁵
Run Pressure	3.6-3.8 torr	2.8-3.0	2.9-3.1	2.9-3.4	2.8-3.0
Bubbler Temp.	5.0°F	56.3	56.3	56.3	56.3
Bubbler Press.	~ 800 torr	~ 750	~ 750	~ 750	~750
TEG Part. Press.	0.414 torr	2.96	2.96	2.96	2.96
H ₂ flow	~ 325 sccm	~ 325	~ 325	~ 325	~ 325
NH ₃ flow	100 sccm	100	100	200	200
H ₂ carrier gas flow	28 sccm	28	28	28	28
TEG flow rate	0.0145 sccm	0.111	0.111	0.111	0.111
W-filament Temp.	1450°C	1450	1450	1450	1450
Susceptor Temp.	500°C	500	500	500	~640
Rotation Speed	1.6 rpm	3	8.25	8.25	8.25
Sec/zone	13.125	7	2.545	2.545	2.545
Run Time	180 minutes	200	140	140	140

* α(6H)-SiC (0001) on axis

** α(6H)-SiC (0001) 3° off-axis toward [11̄20]

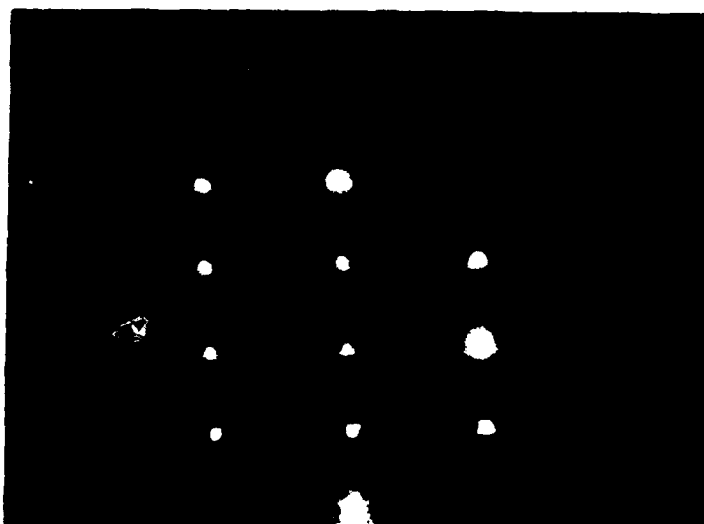
C. Results

Run #10 was the first attempt at the 500°C growth temperature. Scanning Electron Microscopy (SEM) images revealed a surface which appeared extremely smooth with no visible facets. However, the growth rate was very slow at this reduced temperature and TEG flow rate. The film was less than a 100Å thick as evident from Auger Electron Spectroscopy (AES). Increasing the TEG flow rate from 0.0145 sccm to 0.13 sccm in the next run in an effort to increase the growth rate yielded a polycrystalline film as indicated by visible rings in the reflected high energy electron diffraction (RHEED) pattern. Slightly decreasing the TEG flow rate to 0.111 sccm and increasing the rotation speed to 3 rpm (7 sec/zone) for Run #13 yielded better results. The RHEED patterns for this film (Figs. 1 & 2) appear monocrystalline.



{11 $\bar{2}$ 0} Reflection

Figure 1. RHEED pattern for Run #13 of GaN deposited on α (6H)-SiC at 500°C.



{10 $\bar{1}$ 0} Reflection

Figure 2. RHEED pattern for Run #13 of GaN deposited on α (6H)-SiC at 500°C.

However the diffraction spots are not extremely sharp, a result of the faceted surface. From measurements taken from SEM images, the facets had an approximate average diameter of 500Å. Also, as shown in the graph in Fig. 3 the growth was greater layer-by-layer. Fortunately, results show that at 500°C and a TEG flow rate of 0.111 sccm film deposition is constant at approximately 0.5 Å/sec. Thus by increasing the rotation speed and hence reducing exposure time per zone, layer-by-layer growth was achieved in Run #14 and repeated in Run #15 (Fig. 3). Transmission Electron Microscopy (TEM) on Run #14 revealed apparent columnar growth. SEM of Run #15 revealed a uniformly deposited film but also a faceted surface (Fig. 4). The approximate average facet diameter was 400Å for both Runs #14 and #15, slightly less than the facet size of Run #13. Doubling the flow rate of NH₃ from 100 sccm to 200 sccm from Run #14 to #15 caused no readily apparent improvements in film quality. Increasing the growth temperature to 640°C for Run #16 with all other parameters unchanged from Run #15 increased the deposition rate and caused a deviation from layer-by-layer growth. The average facet size of Run #16 as evident from SEM was 1200Å.

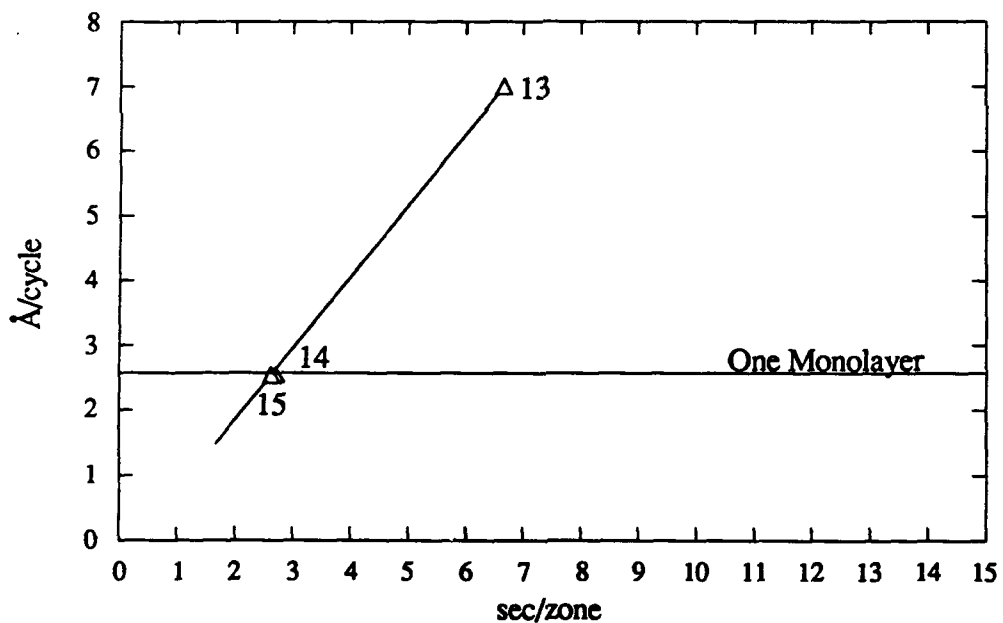


Figure 3. Deposition thickness of GaN per cycle vs. exposure time for Run #'s 13, 14 and 15. The growth temperature was 500°C and at a TEG flow rate of 0.111 sccm for each run.

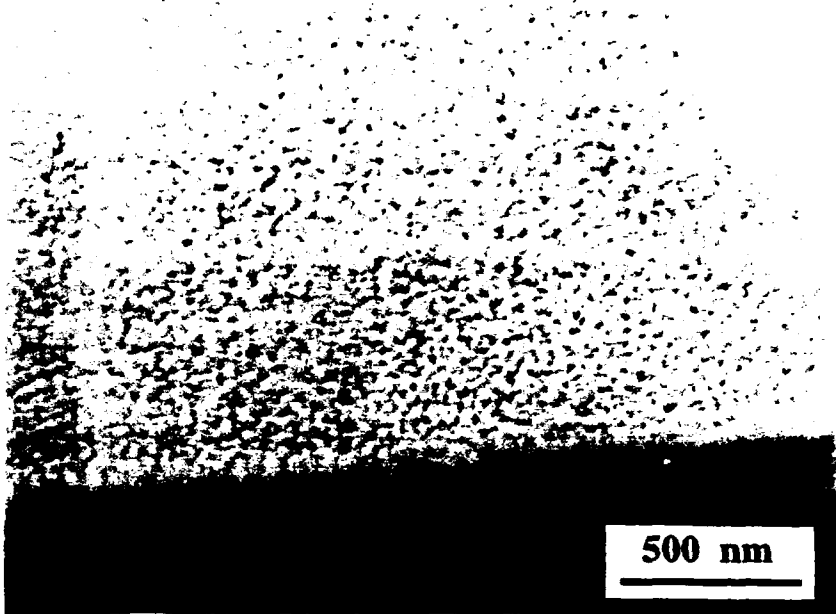


Figure 4. SEM micrograph for Run #15. Notice the uniformly faceted surface. Film thickness is \sim 3000Å and average facet size is \sim 400Å.

D. Discussion

ALE Suspension. In principle, for ALE growth to occur using metalorganic precursors as the column-III source, the MO gas must adsorb to the substrate in a self-terminating mode. For this reason the decomposition mechanisms of the MO precursors are of obvious importance for determining the viability of ALE. The following organometallics are used as source gases for GaN, AlN and InN respectively: triethylgallium (TEG) [Ga(C₂H₅)₃], triethylaluminum (TEA) [Al(C₂H₅)₃] and trimethylindium (TMI) [In(CH₃)₃].

Various experimental techniques have been used to study the decomposition mechanisms of these MO gases [5–16], with mass spectrometry and thermal desorption being the most prevalent. TE(G,A) consist of the metallic species surrounded by three ethyl (C₂H₅⁺) functional groups. Each species adsorbs as a monomer [6]. Via mass spectrometry results for the decomposition of TEG with H₂ as the carrier gas, the decomposition temperature range was 220°–330°C, with ethylene (C₂H₄) being produced [7–9]. This indicates that β -elimination is the dominant decomposition mechanism [5–7,9]. It is also interesting to note that the decomposition temperature range slightly increases (270°–380°C) when N₂ is used as the carrier gas [7]. (The decrease in the decomposition temperature contributed to the presence of H₂ carrier gas is not fully understood at present.) During β -elimination, one of the hydrogen atoms breaks its bond with the β -carbon and joins to the remaining Ga species to satisfy the charge balance. The hydrocarbon functional group re-orientates itself becoming ethylene with a total of four H atoms attached to two double bonded C atoms (Fig. 5).

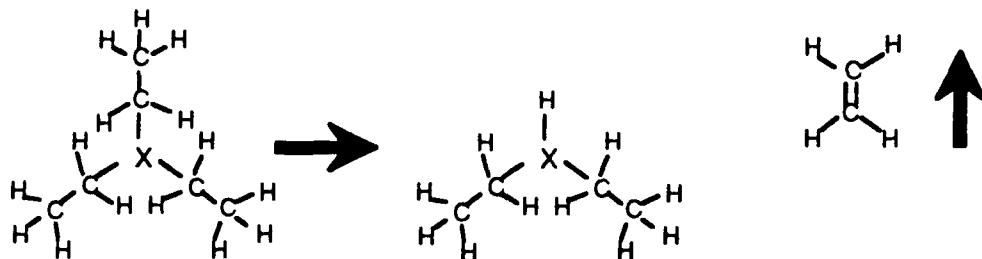


Figure 5. Schematic of the TE(G,A) gas phase decomposition showing β -elimination and the production of ethylene. X represents the column-III species.

Similarly, TEA decomposes by the same β -elimination process at apparently slightly lower temperatures [10]. And presumably to achieve, for example ALE of GaN using TEG, the MO source should only decompose to a diethyl (DEG) or possibly a monoethyl (MEG) species in order for chemisorption to be self-limiting.

TE(G,A) was chosen over TM(G,A) because of its lower decomposition temperature range and a lower carbon incorporation in the growing film during surface decomposition reactions [4]. However, for InN deposition TMI is the organometallic of choice. This results because the TEI precursor is much less thermally stable than its methyl counterpart and undergoes appreciable decomposition starting at 40°C [11] as compared to 270-300°C for TMI [12-15]. However, as expected TMI undergoes a dissimilar decomposition process than that of the triethyl species. As determined by Jacko and Price, TMI predominantly decomposes by homolytic fission and at the low pressures and high temperatures used in many growth techniques methane (CH_4) appears to be the principle reaction product [16].

Therefore, due to the relatively low temperatures necessary for the decompositions of TEG, TEA and TMI, the self-terminating growth mechanism required for ALE deposition appears improbable at the increased growth temperatures of interest. Film deposition in the temperature ranges needed for only the partial decomposition of the MO precursors necessary for self-limiting adsorption have yielded only amorphous and polycrystalline films [4]. Hence, ALE deposition has been suspended in favor of the more realistic layer-by-layer approach.

Experimentations. From experimentations the growth rate at 500°C and a TEG flow rate of 0.111 sccm is constant at approximately 0.5 Å/sec. Simply by adjusting the susceptor rotation speed and thus the exposure time layer-by-layer deposition was achieved. A constant deposition rate has not been evident at 640°C. This phenomenon can be explained as follows [17]. During the growth period in the TEG zone, TEG molecules adsorb on the surface and decompose into Ga atoms. Additional TEG molecules attached to the Ga adsorbed surface may either decompose into more Ga atoms or desorb from the surface before decomposing. At lower growth temperatures it appears that desorption of the TEG molecules is more dominant than further TEG decomposition. However, as the growth temperature increases,

the additional TEG molecules adsorbed onto the surface decompose more easily into Ga atoms rather than desorb from the surface. This finding is supported by the increased deposition rate between Run #15 and Run #16, grown at 500°C and 640°C, respectively, with all other parameters the same.

E. Conclusions

Apparent monocrystalline GaN films have been grown using a layer-by-layer deposition technique. After studying the different decomposition mechanisms of the various MO precursors, ALE was suspended in favor of the layer-by-layer approach. Earlier experimentations support this decision.

At a growth temperature of 500°C and a TEG flow rate of 0.111 sccm the deposition rate is constant at approximately 0.5 Å/sec. A constant growth rate does not exist at 640°C. This phenomenon was explained by the adsorption-decomposition model described above.

F. Future Research Plans and Goals

Deposition of GaN using GaN and AlN buffer layers will be attempted. The use of a buffer layer may reduce the effects of lattice mismatch between the SiC substrate and the depositing film and aid in the growth of more desirable, non-faceted films. Additional plots of thickness per cycle versus exposure time need to be established to investigate the layer-by-layer process at differing temperatures and MO precursor flow rates.

Layer-by-layer growth of AlN and InN is upcoming. Electrical measurements such as mobilities and carrier concentrations need to be established for the deposited III-V films. Also, attempts may be made to p-type dope GaN. A grand goal would be layered III-V nitride films and continuous solid solutions.

G. References

1. H. P. Maruska and J. J. Tietjen, *Appl. Phys. Lett.* **15**, 327 (1969).
2. W. M. Yim, E. J. Stofko, P. J. Zanzucchi, J. I. Pankove, M. Ettenberg and S. L. Gilbert, *J. Appl. Phys.* **44**, 292 (1973).
3. J. A. Sajurjo, E. Lopez-Cruz, P. Vogh and M. Cardona, *Phys. Rev. B* **28**, 4579 (1983).
4. J. Sumakeris, Z. Sitar, K. S. Ailey-Trent, K. L. More and R. F. Davis, *Thin Solid Films* **225**, 244 (1993).
5. A. J. Murrell, A. T. S. Wee, D. H. Fairbrother, N. K. Singh, J. S. Foord, G. J. Davies and D. A. Andrews, *Vacuum*, **41(4-6)**, 955 (1990).
6. T. R. Gow, F. Lee, A. L. Backman and R. I. Masel, *Vacuum* **41(4-6)**, 951 (1990).
7. M. Yoshida, H. Watanabe and F. Uesugi, *J. Electrochem. Soc.* **132(3)**, 677 (1985).
8. M. Hoshino, *J. Crystal Growth*, **110** (1991) 704.
9. W. Lee, T. R. Omstead, D. R. McKenna and K. F. Jensen, *J. Crystal Growth*, **85**, 165 (1987).
10. W. L. Smith and T. Wartik, *J. Inorg. Nucl. Chem.* **29**, 629 (1967).
11. *CVD Metalorganics for Vapor Phase Epitaxy: Product Guide and Literature Review II*, Advanced Materials, Morton International, Danvers, MA.
12. D. A. Jackson, Jr., *J. Crystal Growth* **94**, 459 (1989).

13. R. Karlicek, J. A. Long and V. M. Donnelly, *J. Crystal Growth* **68**, 123 (1984).
14. C. A. Larsen and G. B. Stringfellow, *J. Crystal Growth* **75**, 247 (1986).
15. N. I. Buchan, C. A. Larsen and G. B. Stringfellow, *J. Crystal Growth* **92**, 591 (1988).
16. M. J. Jacko and S. J. W. Price, *Can. J. Chem.* **42**, 1198 (1964).
17. N. Kobayashi, T. Makimoto and Y. Horikoshi, *Jpn. J. of Appl. Phys.* **24**, L962 (1985).

X. Deposition of Aluminum Nitride Films Via Decomposition of $\text{AlCl}_3 \times \text{NH}_3$ Complex

A. Introduction

Pure aluminum nitride, possesses a high electrical resistivity ($>10^{13}$ W-cm) and high thermal conductivity, (2W/cm-K). As such, it is a candidate material for active and passive components in electronic circuits and for substrates which carry the Si chips containing these circuits. This material also has the highest reported surface acoustic wave velocity [1] which makes it viable for many piezoelectric applications. Aluminum nitride is frequently considered for use for optical devices that can operate throughout the entire visible spectrum and into the medium ultraviolet wavelengths. The high hardness possessed by this material (1800 on knoop scale) is an indication of good mechanical strength. Because AlN is non-toxic, it is a likely candidate to supplant Beryllium Oxide in a variety of applications. Several of the above mentioned applications are still waiting for good-quality aluminum nitride single crystals. Some useful properties of AlN are summarized in Table I. For those interested in more information on aluminum nitride, many excellent reviews are available [2-5].

Table I. Some properties of aluminum nitride

Crystal structure	Wurtzite
Lattice constant	$a = 3.112 \text{ \AA}$
	$c = 4.982 \text{ \AA}$
Bandgap energy	6.2 eV (300K)
Thermal expansion coefficient [4]	$5.3 \times 10^{-6} / \text{K (c)}$ $4.2 \times 10^{-6} / \text{K (a)}$
Thermal conductivity [7]	$K = 2 \text{ W / cm K}$
Dielectric constant [4]	$\epsilon = 9.0$
Electrical resistivity	typically $>10^{13} \text{ W-cm}$
Hardness	1800 (on knoop scale)
Density	3.255 g/cm^3
Work function	5.36 eV

Due to its high melting point and its instability near the melting temperature, most AlN single crystal material has been grown from the vapor phase. For the past 20 years, two major growth techniques have dominated high quality crystal growth—chemical vapor deposition

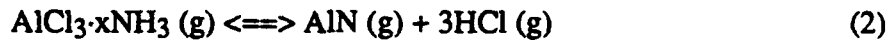
(CVD) and molecular beam epitaxy (MBE). Single crystals, 25 mm thick, were grown on SiC (0001) by Chu *et al.* via using AlCl₃ and NH₃ as precursors in the temperature range of 1200–1250 °C. Typical molar ratios of AlCl₃/NH₃ that they used were in the range of 5×10⁻⁴ to 5×10⁻³. Cox *et al.* [47] were able to obtain single crystals of AlN on C-plane of sapphire by using AlCl₃ and NH₃ at 1780 °C. Being the most common sources, AlCl₃ and NH₃ were used by Norieka and Ing [28] to grow AlN on Si substrates between 900 and 1300 °C. An orientation relationship of (0001)_{AlN} / (111)_{Si} was observed. It was reported that the growth rate decreased from 12 μm/hr at 1000°C to 4 μm/hr at 1200°C. In 1981 Morita *et al.* [17] grew epitaxial AlN films on Si (100), Si (110) and Si (111). They have employed TMA and NH₃ as sources. The films were grown at 1260°C and had rough surfaces.

As mentioned, the majority of previous research in this field was conducted using chemical vapor transport systems. The choice of precursors falls into one of two categories. The first and most widely used includes metalorganic compounds as the aluminum source (e.g. trimethylaluminum) and ammonia as the nitrogen source [11–26]. The second category uses metal halides e.g., AlCl₃ or AlBr₃ as the aluminum source and, again, ammonia as the nitrogen source [27–47].

If tricholoroaluminum and ammonia are chosen as starting materials, there are two ways to approach the growth of crystals. One is to introduce the two gases separately into the system and let them react at the substrate. The second route is to combine ammonia and the tricholoroaluminum before they reach the substrate. In the latter route, the two compounds will form an intermediate complex (adduct) represented by the following formula; AlCl₃·xNH₃, where x is between 1 and 6 [31,35,39].

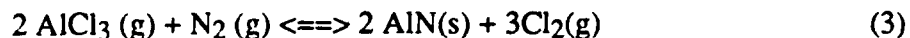
B. Experimental Procedure

As stated in the previous section, the chosen way to deposit aluminum nitride in the present studies involves the formation of a complex compound (i.e., adduct) and the decomposition of this adduct at a higher temperature. This complex was formed by mixing AlCl₃ and NH₃ at about 400 °C. This approach can be summarized best by the following chemical reactions.

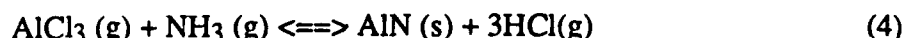


Nitrogen gas was passed over the heated AlCl₃ powder to carry it into the growth system. In the AlCl₃–NH₃–N₂ system the only gaseous species that were of concern were, AlCl₃, Al₂Cl₆, H₂, N₂ and NH₃. Al₂Cl₆ is the primary gaseous species over AlCl₃ when it is

sublimed. Al_2Cl_6 transforms to AlCl_3 at temperatures above 600 °C. The presence of the dimer form does not effect the formation of the adduct because Al_2Cl_6 is also capable of combining with NH_3 to form the complex that is of interest [39]. From K. Nickel's work [39] it can be seen that in the range of the temperature and composition that of our interest, it is not possible to nitridize AlCl_3 with N_2 . In other words, Equation 3 has a very high positive ΔG value for all temperatures of our concern.



Perhaps the following two reactions need also be considered for system of our purposes.



Although reaction (4) has a strongly negative free energy value at the temperatures where AlN is the only condensed phase, NH_3 is not stable. If NH_3 decomposes according to Equation (5) then no yield can be expected from Equation (4). However the decomposition of ammonia will never take place to the full extent. The approximated yield of reaction (4) is about 20 % [39]. Although introducing NH_3 and AlCl_3 separately into the reaction chamber has been one of most popular methods, from the above discussion it does not appear to be the most efficient way of depositing AlN . Especially for bulk material growth, a method with a higher efficiency would be more useful.

Thus, in order to obtain high deposition yields for AlN , decomposition of ammonia must be suppressed. This can be achieved in two ways. One is the choice of reactor material. It is known that metals (like Fe or Cu) favor decomposition of ammonia while the ceramic materials hinder it. The second and the more reliable way of preventing the decomposition of ammonia is to form an adduct by combining it with AlCl_3 prior to deposition. This is actually one of the more important points that was considered when the present system was designed. The adduct has a wide range of temperature stability. The minimum temperature needed to form the adduct is 340 °C and it is stable up to 700 °C. Above this temperature, the adduct will decompose according to Equation (2). Using this method, we need only concern ourselves with the decomposition of the adduct at the right temperature to ensure the formation of aluminum nitride. Temperatures higher than this yielded in homogeneous nucleation (i.e., gas phase nucleation) of AlN , which is of no use for our purposes.

Table II. Typical growth parameters

Substrate temperature	900–1100 °C
Adduct formation temperature	380–400 °C
AlCl ₃ temperature	70–90 °C
Carrier gas (nitrogen) flow rate	350 sccm
Ammonia flow rate	350 sccm

C. Results And Discussion

Polycrystalline AlN films were grown on Si(100), Si(111) and SiC(0001) substrates. Lack of control over the flow dynamics in the system has, to date, prevented the achievement of film uniformity. Both vertical and horizontal substrate holders were used. The better films were grown using the vertical substrate holder where the substrate was parallel to the gas flow. Scanning electron micrographs of the microstructures of the films grown on Si and SiC substrates are shown in Figs. 1 and 2.

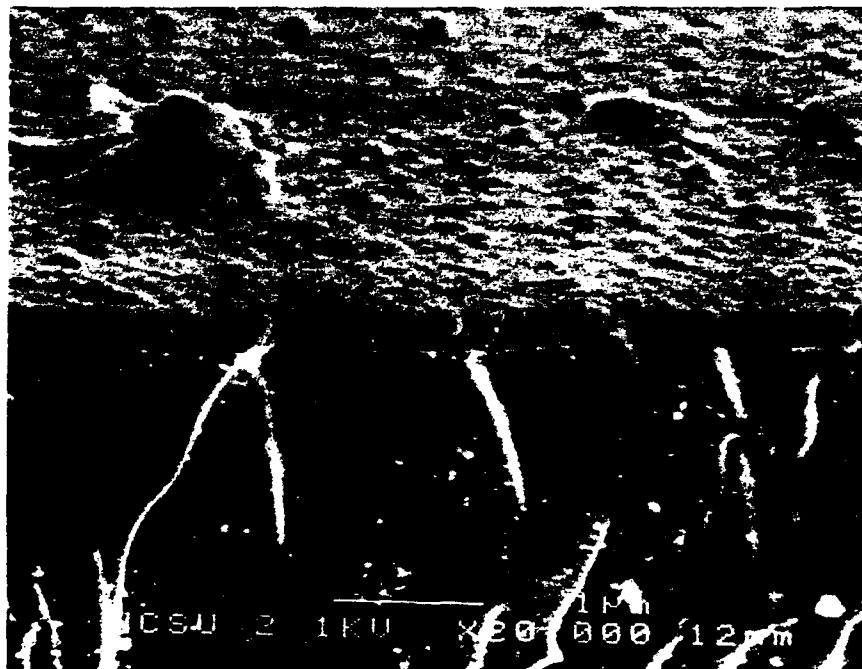


Figure 1. Polycrystalline AlN film grown on Si.



Figure 2. AlN on SiC substrate.

D. Conclusions

Results obtained from the experiments conducted to date indicate that deposition of single crystal AlN films have a high feasibility with an improved reactor design. It has been proven that the idea of preserving the 1:1 ratio of Al to N via forming an intermediate compound can be achieved. Thus, the decomposition of ammonia can be suppressed which is the major factor that reduces the yield of the process.

E. Future Research Plans

One of the major problems that was faced came from the design of the heater. Since the heater surrounds the entire reaction chamber and the aim was to heat the substrate only, the gas inside the chamber was also heated. This resulted in homogeneous nucleation of AlN. This effect was reduced by changing the substrate holder and letting the adduct flow over the substrate allowing less time for it to decompose in the gas phase and stick to the substrate. One other difficulty arises from the flow pattern of the gases in the system. More uniform coverage of the substrate must be achieved. Solving these two technical problems is the key step limiting further progress in obtaining single crystal aluminum nitride with this system, see Figs. 3 and 4.

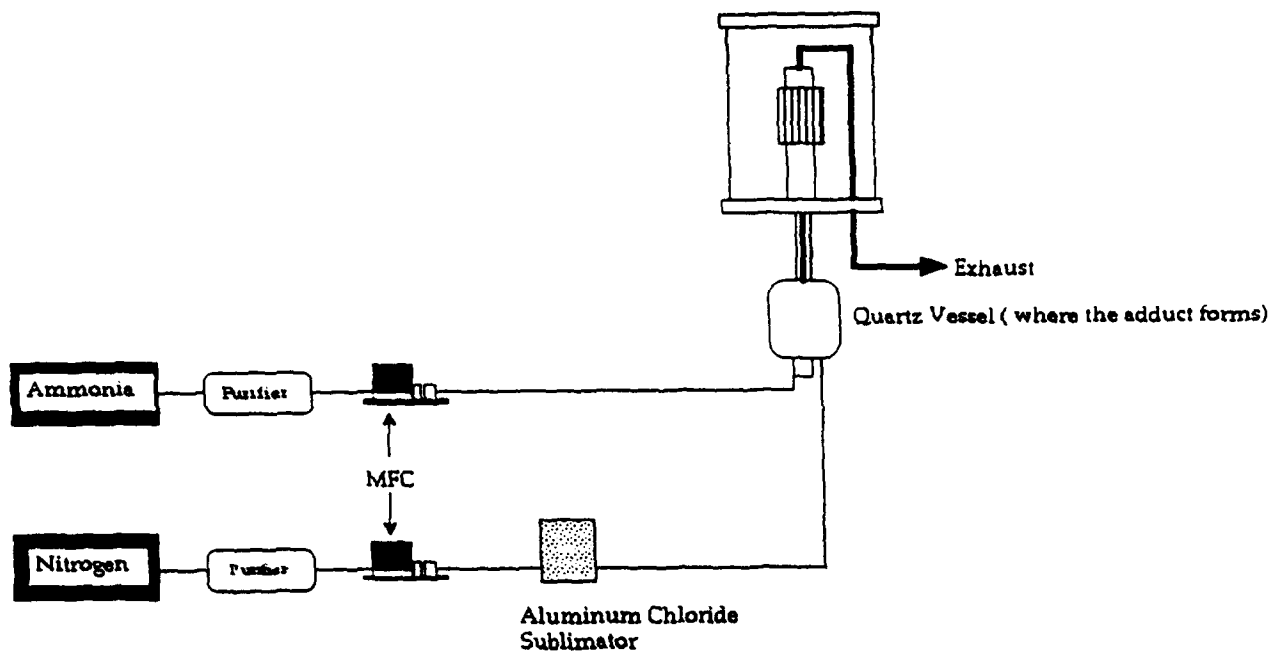


Figure 3. The system schematic.

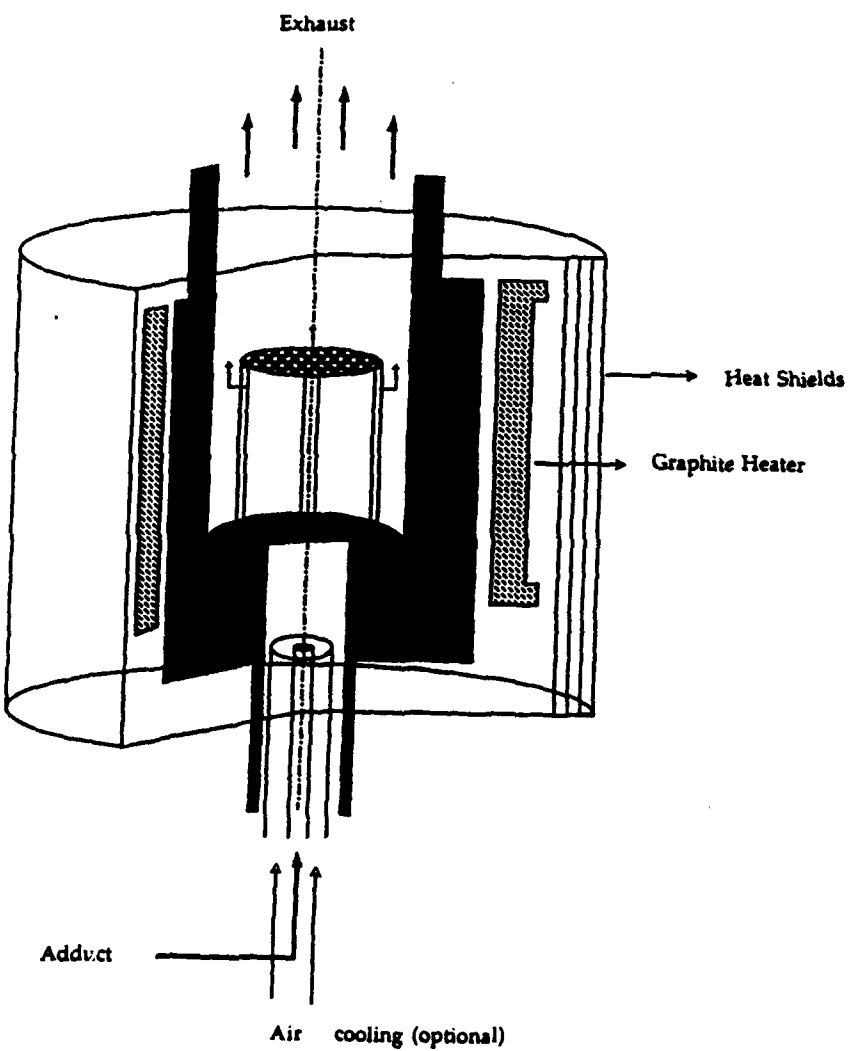


Figure 4. Cross-section of the reaction chamber.

F. References

1. G. R. Kline and K. M. Lakin, *Proc. IEEE Symp. Ultrasonics*, **14**, 340 (1983).
2. M. T. Duffy, in *Heteroepitaxial Semiconductors for Electronic Devices*, G.W. Cullen and C.C. Wang, Eds., Springer Verlag, Berlin (1978), pp. 150–181.
3. R. F. Davis, *Proc. IEEE* **79**, 702 (1991).
4. S. Strite and H. Morkoc, *J. Vac. Sci. Technol. B* **10**, (1992)
5. J. H. Edgar, *J. Mater. Res.* **7**, 235 (1992).
6. C. O. Dugger, *Mat. Res. Bull.* **9**, 331, (1974).
7. G. A. Slack and T. F. McNelly, *J. Crys. Gro.* **34**, 263, (1976).
8. G. A. Slack and T. F. McNelly, Final Technical Report, AFOSR Contract F44620-76-C-0039K, March (1978).
9. P. Bhattacharya and D. Bose, *Jap. J. Appl. Phys.* **10**, L1750, (1991).
10. S. Yoshida, S. Mizawa, Y. Fujii, S. Takada, H. Hakayama, S. Gonda, A. Itoh, *J. Vac. Sci. Tech.* **16**, 990, (1979).
11. H. M. Manasevit, F. M. Erdmann and W. I. Simpson, *Metalorganics and Semiconductor Materials*, **118**, 1864, (1971).
12. W. M. Yim, E. J. Stofko, P. J. Zanzucchi, J. I. Pankove, *J. Appl. Phys.* **44**, 359, (1973).
13. M. T. Duffy and G. D. O'Clock, Jr., *Appl. Phys. Lett.* **23**, 55, (1973).
14. F. A. Pizzarello and J. E. Coker, *J. Elect. Mat.* **4**, 25, (1975).
15. M. Morita, S. Isogai, K. Tsubouchi and N. Mikosiba, *Appl. Phys. Lett.* **38**, 1 (1981).
16. M. Morita, S. Isogai, N. Shimizu, K. Tsubouchi, N. Mikosiba, *Jap. J. Appl. Phys.* **20**, L173 (1981).
17. M. Morita, S. Isogai, N. Shimizu, K. Tsubouchi, N. Mikosiba, *Jap. J. Appl. Phys.* **21**, 728 (1982).
18. U. Rensch and G. Eichorn *Phys. Stat. Sol. (a)* **77**, 195, (1983).
19. U. Rensch and G. Eichorn *Phys. Stat. Sol. (a)* **90**, 135, (1985).
20. K. Sato, *Ultrasonics Symposium*, pp. 192 (1985).
21. L. V. Interrante, L. E. Carpenter, C. Whitmarsh, and W. Lee, *Mat. Res. Soc. Sym. Proc.* **23** (1986).
22. F. Hasegawa, T. Takahashi, K. Kubo, and Y. Nannichi, *Jap. J. Appl. Phys.* **26**, 1555, (1987).
23. R. K. Sadhir, H. E. Saunders, and W. A. Bryers, *IEEE Proc.* (1987).
24. K. Akimoto, I. Hirosawa, J. Mizuki, S. Fujieda, Y. Matsumoto and J. Matsui, *Jap. J. Appl. Phys.* **27**, 1401 (1988).
25. L. V. Interrante, W. Lee, M. McConnell, N. Lewis, and E. Hall, *J. Electrochem. Soc.* **136**, 472 (1989).
26. C. C. Amato et al., *Mat. Res. Soc. Sym. Proc.*, T. M. Besmann, B. M. Gallois. Eds. **168**, pp. 119 (1990).
27. T. L. Chu, D. W. Ing and A. J. Noreika, *Solid State Electronics*, **10**, 1023 Pergamon Press. (1967).
28. D. W. Ing and A. J. Noreika, *J. Appl. Phys.* **39**, (1968).
29. M. P. Callaghan, E. Patterson, B. P. Richards and C. A. Wallace, *J. Crystal Growth* **22**, 85, (1974).
30. T. L. Chu and R. W. Kelm, *J. Electrochem. Soc. Solid State Science and Technology*, (1975).
31. H. Arnold, L. Biste, D. Bolze, *Kristall Technik*, **11**, 17, (1976).
32. H. Arnold, L. Biste, T. Kaufman, *Kristall Technik*, **13**, 929, (1978).
33. Y. Pauleau, A. Bouteville, J. J. Hantzpergue and J. C. Remy *J. Electrochem. Soc.: Solid State Science and Technology*, (1980).
34. V. F. Funke, V. V. Kosukhin, A. A. Klement'ev, P. P. Oleinikov and D. M. Lyakov, *Neorganicheskie Materialy*, **22**, 73, (1984).
35. H. Komiyama and T. Osawa, *Jap. J. Appl. Phys.* **24**, 795, (1985).
36. M. Suzuki and M. Tanji, *Proceedings of the Tenth International Conference on CVD*, (1987).

38. Y. G. Roman and P. G. Andriaansen, Thin Films **169**, 241, (1989).
39. K. G. Nickel, R. Riedel and G. Petzow, J. Am. Ceram. Soc. **72**, 1804, (1989).
40. T. Goto, J. Tsuneyoshi, K. Kaya and T. Hirai, J. Mat. Sci. **27**, 247, (1990).
41. R. Riedel and K. Gaudi , Am. Ceram. Soc. **74**, 1331, (1991).
42. T. S. Moss, J. A. Hanigovsky and W. J. Lackey , J. Mater. Res. **7**, 754 (1991).
43. T. M. Mayer, J. W. Rogers and T. A. Michalske, Chem. Mater. **3**, 642, (1991).
44. W. Y. Lee, W. J. Lackey and P. K. Agrawal, J. Am. Ceram. Soc. **74**, 1821, (1991).
45. W. Y. Lee, W. J. Lackey and P. K. Agrawal, J. Am. Ceram. Soc. **74** [9], pp. 2136, (1991)
46. W. Y. Lee, W. J. Lackey and P. K. Agrawal, J. Am. Ceram. Soc. **74** [10] pp. 2649, (1991)
47. G. A. Cox, D. O. Cummins, K. Kawabe, and R. H. Tredgold, J. Phys. Chem. Solids **28**, 543 (1967).
48. Z. J. Yu, J. H. Edgar, A. U. Ahmed, and A. Rys, J. Electrochem. Soc. **138**, 196 (1991).
49. Z. Sitar, M. J. Paisley, B. Yan, R. F. Davis, J. Ruan, and J. W. Choyke, Thin Solid Films **200**, 311 (1991).
50. L. B. Rowland, Ph.D. dissertation, North Carolina State University, Raleigh, (1992).

XI. Development of Photo- and Cathodoluminescence System for Characterization of Wide Bandgap Semiconductor Thin Films

A. Introduction

Luminescence is the emission of photons due to excited electrons in the conduction band decaying to their original energy levels in the valance band. The wavelength of the emitted light is directly related to the energy of the transition, by $E=h\nu$. Thus, the energy levels of a semiconductor, including radiative transitions between the conduction band, valance band, and exciton, donor, and acceptor levels, can be measured [1,2].

In luminescence spectroscopy various methods exist to excite the electrons, including photoluminescence (photon excitation), and cathodoluminescence (electron-beam excitation). In each technique signal intensity is measured at specific wavelength intervals using a monochrometer and a detector. The intensity versus wavelength (or energy) plot can then be used to identify the characteristic energy bandgap and exciton levels (intrinsic luminescence) of the semiconductor, and the defect energy levels (extrinsic luminescence) within the gap [1].

Both photo- and cathodoluminescence analysis has been performed on AlN, GaN, and $\text{Al}_x\text{Ga}_{1-x}\text{N}$ semiconductors [3–8]. Much of the work has been in measuring the low temperature GaN luminescence peaks. Work on AlN has been limited by the energy gap of 6.2 eV, which corresponds to a wavelength (200 nm) that is lower than most of the optical light sources. An excimer laser using the ArF line (193 nm) can be used, but caution must be taken when operating at these wavelengths.

Few time-resolved luminescence measurements have been performed on AlN and GaN. In a time-resolved measurement, a pulsed source is used to excite the sample and the luminescence is measured at short sampling intervals after the pulse. The result is an intensity vs. time plot. Time resolved spectroscopy is useful for separating the emission bands of the investigated samples with different decay times. It is often used to measure donor-acceptor recombination rates and minority carrier lifetimes [1].

Depth-resolved information can be obtained using cathodoluminescence, since generation depth varies with beam voltage. This technique is particularly useful for studying ion implanted semiconductors and layered structures [1].

B. Future Research Plans and Goals

A combined photo- and cathodoluminescence system has been assembled and will be used to perform luminescence measurements on AlN, GaN, and $\text{Al}_x\text{Ga}_{1-x}\text{N}$ semiconductors. A schematic view is shown in Fig. 1, and a block diagram is shown in Fig. 2. The sample is in a UHV chamber, and the monochrometer and collection optics are in a vacuum environment. Each sample is attached to a cryostat from APD cryogenics, which allows for

luminescence measurements at temperatures as low as 4.2 K. The monochrometer is a McPherson model 219 vacuum monochromator. Its focal length is .5 m, with a wavelength resolution of .02 nm at 313.1 nm. This high resolution will allow for the identification of exciton and defect energy levels. A photon counter from Stanford Research (SR-400) with a Hamamatsu Photomultiplier tube is used to acquire the data, and a software package from Galactic Industries (Spectra-Calc) is used to analyze the results.

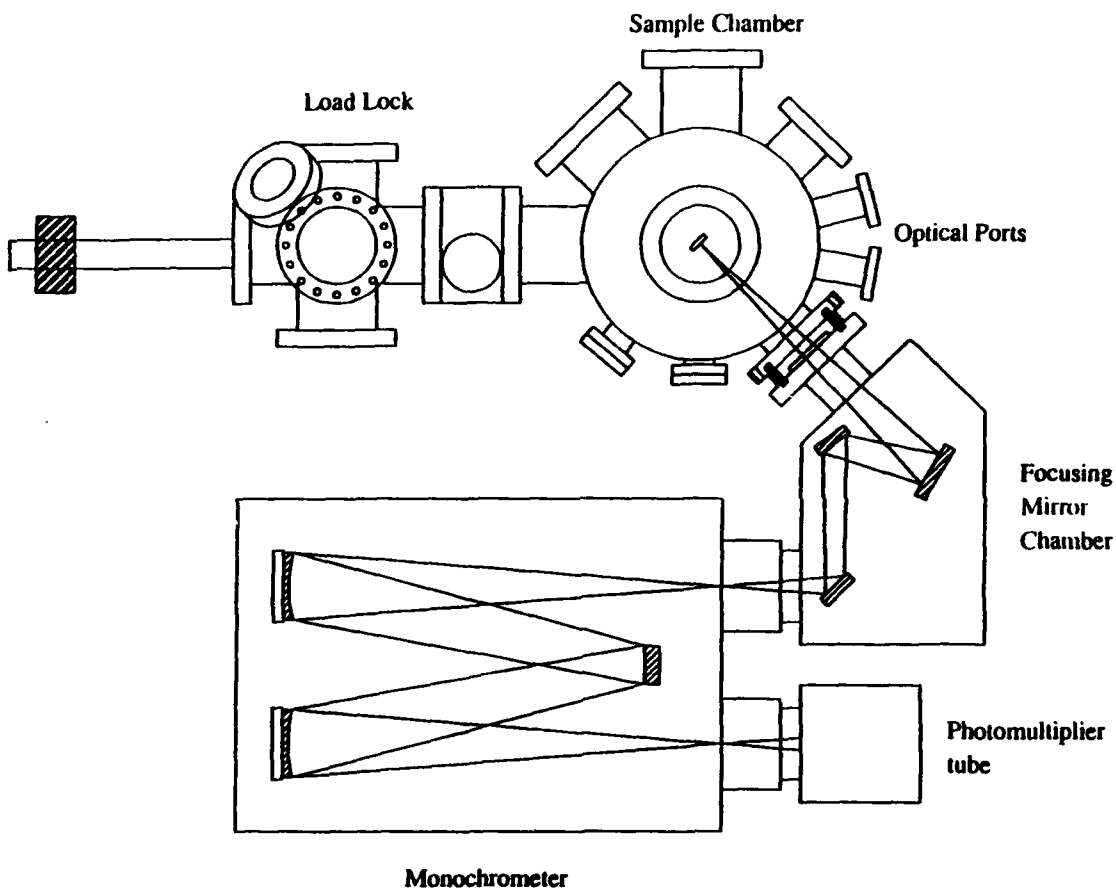


Figure. 1. Schematic of the combined photo- and cathodoluminescence system.

Two optical sources and a beam blanking electron gun are the excitation sources. One optical source is a He-Cd laser with a power of 15 mW. It is a continuous wavelength laser that operates at a wavelength of 325 nm, making it practical for testing the luminescence of GaN. A pulsed excimer laser is the other optical source; it operates at wavelengths of 193 nm (6.4 eV), 248 nm (5.0 eV), and 308 nm (4.0 eV); and so it can be used to measure the luminescence of both AlN and GaN.

The beam blanking capability of the electron gun will allow for time-resolved luminescence measurements of the semiconductors. The SR-400 will be used for data

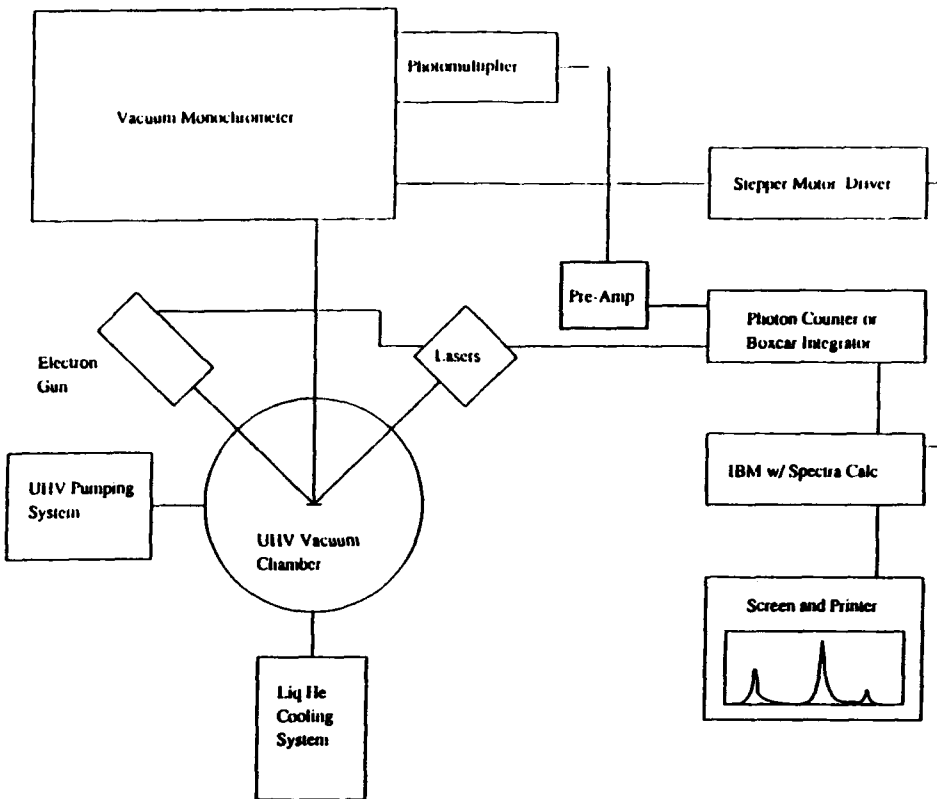


Figure 2. Block diagram of the combined photo- and cathodoluminescence system.

collection, although a boxcar integrator may also be used. The electron gun has a maximum beam voltage of 10 keV, which allows for depth-resolved spectroscopy to be performed.

Cathodoluminescence in the TEM will also be performed on the nitride films through a collaboration with Dr. Roger Graham at Arizona State University. In the TEM environment the luminescence from individual defects can be examined, and hence the source of extrinsic luminescence peaks can be identified.

C. References

1. B. G. Yacobi and D. B. Holt, *Cathodoluminescence Microscopy of Inorganic Solids*, Plenum Press, New York (1990).
2. M. D. Lumb, Ed., *Luminescence Spectroscopy*, Academic Press, New York (1978).
3. S. Strite and H. Morkoç, GaN, AlN, and InN review.
4. R. A. Youngman and J. H. Harris, *J. Am. Ceram. Soc.*, **73** [11] 3238-46 (1990).
5. S. Strite, J. Ruan, Z. Li, N. Manning, A. Salvador, H. Chen, D. J. Smith, W. J. Choyke, and H. Morkoç, "An investigation of the properties of b-GaN grown on GaAs."
6. M. A. Khan, R. A. Skogman, J. M. Van Hove, S. Krishnankutty, and R. M. Kolbas, *Appl. Phys. Lett.* **56** (13) 1257-59 (1990).
7. Z. Sitar, M. J. Paisley, J. Ruan, J. W. Choyke, and R. F. Davis.
8. V. F. Veselov, A. V. Dobrynin, G. A. Naida, P. A. Pundur, E. A. Slotsenietse, and E. B. Sokolov, *Inorganic Materials*, **25** (9) 1250-4 (1989).

XII. The Influence of Interfacial Hydrogen and Oxygen on the Schottky Barrier of Nickel on (111) and (100) Diamond Surfaces

J. van der Weide and R. J. Nemanich

Department of Physics

North Carolina State University

Raleigh, NC 27695-8202

Abstract

The Schottky barrier of thin ($<5\text{\AA}$) nickel films on natural type IIb (p-type semiconducting) diamond (111) and (100) surfaces were determined with ultraviolet photoemission spectroscopy. Prior to nickel deposition the diamond (111) surfaces were exposed to an argon plasma while heated to 350°C . This resulted in a change from a negative electron affinity surface to a positive electron affinity surface. This effect is used as an indication that a hydrogen free surface had been obtained. Deposition of a monolayer of nickel on this hydrogen free diamond (111) resulted in a Schottky barrier height of 0.5 eV. In addition, it was found that the deposition of nickel led to a negative electron affinity surface. Upon further deposition of nickel the Schottky barrier height increased by ~ 0.2 eV, and the negative electron affinity effect was reduced. When hydrogen was present on the (111) surface, an increased Schottky barrier height of ~ 1.0 eV was observed. Diamond (100) surfaces were prepared by a vacuum anneal to temperatures ranging from 500°C to 1070°C . Oxygen was present on the surface after loading, but was reduced after a 900°C , and could not be observed after a 1000°C anneal. A lowering of the electron affinity on the diamond (100) surface by ~ 1 eV, was observed as the annealing temperature was increased. This led to a negative electron affinity after the surface had been annealed to temperatures above $\sim 1000^\circ\text{C}$. After annealing, a 2×1 surface reconstruction was observed. Nickel was deposited after the various anneals, and Schottky barrier heights were found which ranged from 1.5 eV for the 545°C annealed surface, to 0.7 eV for the 1070°C annealed, reconstructed surface. The general trend for both the (100) and (111) surface is that the presence of chemisorbed species, such as hydrogen and oxygen, resulted in an increase in Schottky barrier height.

Submitted to Physical Review B

A. Introduction

Diamond exhibits unique electronic properties, such as a wide band gap (5.47 eV), high carrier mobilities ($\mu_n = 2200 \text{ cm}^2/\text{V}\cdot\text{s}$, $\mu_p = 1600 \text{ cm}^2/\text{V}\cdot\text{s}$) and a high breakdown field (10^7 V/cm), which combine to make diamond an excellent semiconductor material to be used for high speed, high temperature or high power transistors. With the development of chemical vapor deposition growth of diamond, diamond has the possibility to become an economically viable electronic material. In order to make use of these diamond for device technology, both ohmic and rectifying contacts to diamond will be needed. At present only p-type diamond can be reliably manufactured, and Schottky barriers may play an important role, as an alternative for the p-n junction. Various field effect transistors (FET) [1-5] and bipolar junction transistors [6, 7] based on diamond, have been reported.

In this paper we report Schottky barrier height measurements of nickel thin films, deposited on natural diamond (100) and (111) surfaces. The diamond (111) surfaces were exposed to an argon plasma prior to nickel deposition, while the diamond (100) surfaces were annealed to temperatures ranging from 500°C to 1070°C. The Schottky barrier heights were determined from photoemission measurements. The diamond surfaces were characterized using photoemission and Auger electron spectroscopy. The effects of surface structure and surface preparation on the Schottky barrier height of nickel thin films deposited on natural diamond (111) and (100) surfaces, is discussed and related to theoretical studies.

Because of the rapid developments in the field of diamond growth in recent years, the metal-diamond interface has been studied more intensely. A number of reports have described metal contacts on diamond [8-29]. The general trend that emerges is that the as-deposited metal contact exhibits rectifying behavior. In order to make ohmic contacts, however, the diamond surface has to be modified [15, 26, 30], or heavily doped [9, 24] before the metal is deposited. Or alternatively, if a carbide forming metal is used, a metal carbide can be formed by annealing the contact [27, 31]. After the annealing these contacts are often found to be ohmic [12, 20, 21, 27, 32]. With a few exceptions, however, these studies are limited to current-voltage measurements. The current-voltage measurements on rectifying contacts that have been analyzed indicate large ideality factors for the metal-diamond interfaces [10, 16, 18, 28, 33], which makes an accurate determination of the Schottky barrier from current-voltage measurements difficult. Actual Schottky barrier measurements have been performed with a variety of methods and have mainly focused on gold or aluminum on diamond. Using current-voltage, capacitance-voltage and photoresponse methods, Mead and McGill have found Schottky barrier heights ranging from 1.7 eV to 2.0 eV for gold on chemically cleaned surfaces, and 1.9 eV to 2.2 eV for aluminum contacts [34]. Himpsel *et al.* report Schottky barrier heights of 1.3 eV for gold and 1.5 eV for aluminum, on unreconstructed diamond (111), determined with photoemission spectroscopy

measurements [35, 36]. For gold and aluminum on chemical vapor deposited diamond films a Schottky barrier height of 1.13 eV was found by Hicks *et al.*, using internal photoemission [16]. Gold and aluminum have differing work functions (5.1 eV and 4.3 eV respectively) and differing electron negativities (2.4 and 1.5 respectively). These comparative studies therefore indicate that the Schottky barrier height of metals on diamond is only weakly dependent on the properties of the metal. Other reports concerning gold contacts include capacitance-voltage measurements by Glover who reports a value of 1.7 eV for gold on synthetic diamond (100) [14], and internal photoemission measurements indicating a Schottky barrier of 1.15 eV for gold on chemical vapor deposited diamond film by Grot *et al.* [29].

In addition to reports of these non-carbide forming metals, there have been reports of Schottky barrier height measurements of carbide forming materials. Using UV-photoemission spectroscopy van der Weide *et al.* reported a Schottky barrier height of 1.0 eV for titanium on diamond thin films, and on an argon plasma cleaned diamond (111) surface [31, 37]. Tachibana *et al.* report a value of 1.3 eV for titanium on diamond films, obtained from X-ray photoemission measurements. They also found that the Schottky barrier was reduced to 0.8 eV after annealing the contact to 430°C for 30 minutes [27]. Geis *et al.* report rectifying behavior for tungsten contacts on diamond (100) for temperatures up to 700°C. From the current-voltage measurements a barrier height of 1.3 eV was found [10]. Also using current-voltage measurements, a similar value of 1.2 eV was found by Shiomi *et al.* for tungsten on diamond films, grown epitaxially on diamond (100) and (110) surfaces. X-ray photoemission studies of gold, aluminum and titanium on reconstructed and unreconstructed diamond (100) and (111) surfaces, were performed by Tachibana *et al.* [38]. They report an increase in the downward band bending, by as much as 1 eV, as a function of metal thickness, deposited on the unreconstructed surfaces. The absolute values for the Schottky barrier heights were not obtained, but the downward band bending indicates an increase in the Schottky barrier height. Similar studies, performed on the reconstructed (111) and (100) surfaces did not show any significant change in the band bending. The difference between the reconstructed, and unreconstructed surfaces is attributed to Fermi level pinning at the surface by the surface states associated with the reconstruction. The various Schottky barrier heights mentioned above, are summarized in Figure 1.

Nickel and copper have an FCC crystal structure, with lattice constants that closely match the lattice constant of diamond ($a(\text{dia})=3.567\text{\AA}$, $a(\text{Ni})=3.523\text{\AA}$, $a(\text{Cu})=3.615\text{\AA}$). There have been attempts to use this close lattice match to obtain heteroepitaxial growth of diamond on these metals [39-44]. Although it is possible to grow nickel epitaxially on diamond (111) and (100) surfaces [18, 45, 46], heteroepitaxy of diamond grown on nickel has not been reported to date. There have been, however, reports of oriented growth on nickel substrates seeded with diamond particles, which are oriented with respect to the nickel surface [47, 48].

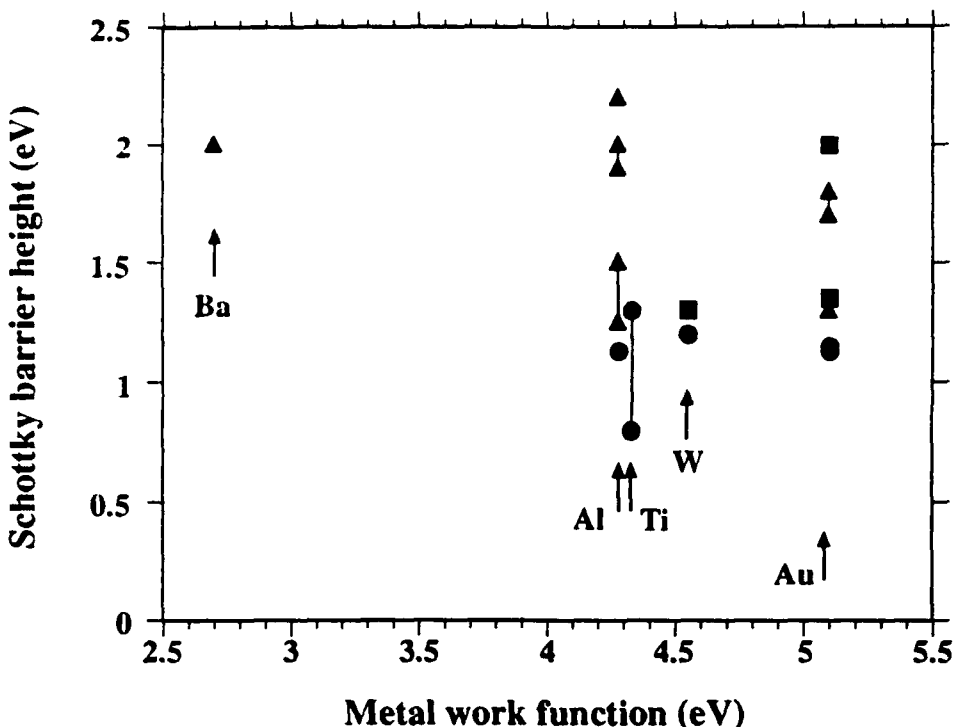


Figure 1. Summary of Schottky barrier heights reported in the literature, and listed in the text. The triangles represent data obtained from (111) surface, the squares represent data from (100) surfaces, and the circles are Schottky barrier heights on diamond film.

Theoretical investigations of the diamond-nickel interface have been performed by Erwin and Pickett [49-53]. Their calculations are focused on two different structures for nickel on both the (111) and the (100) surfaces. These structures are shown in Figure 2. For both the (111) and the (100) surface a Schottky barrier of less than 0.1 eV is found, for the most stable configurations. It should be noted, however, that these calculations are focused on nickel deposited on idealized diamond surfaces, and the presence of chemisorbed species is not taken into account. Calculations on the effects of hydrogen on the Schottky barrier height have been performed by Lambrecht on the copper-diamond (111) interface [54]. For copper on the hydrogen free diamond surface Lambrecht reports a Schottky barrier height of less than 0.1 eV, which is similar to the results found by Erwin and Pickett for nickel on the diamond (111) surface. Lambrecht found, however, that the presence of interfacial hydrogen resulted in an increased Schottky barrier height of ≥ 1.0 eV.

After *ex situ* preparations of the surfaces, the diamond (111) surface is typically found to be terminated by hydrogen [55-58] with one hydrogen atom bonded to each surface carbon atom. The presence of this hydrogen is found to lower the work function of the surface, which causes the diamond (111) surface to exhibit a negative electron affinity [56, 58]. This means that electrons that are at the conduction band minimum have sufficient energy to overcome the work function. The presence of a negative electron affinity can be detected

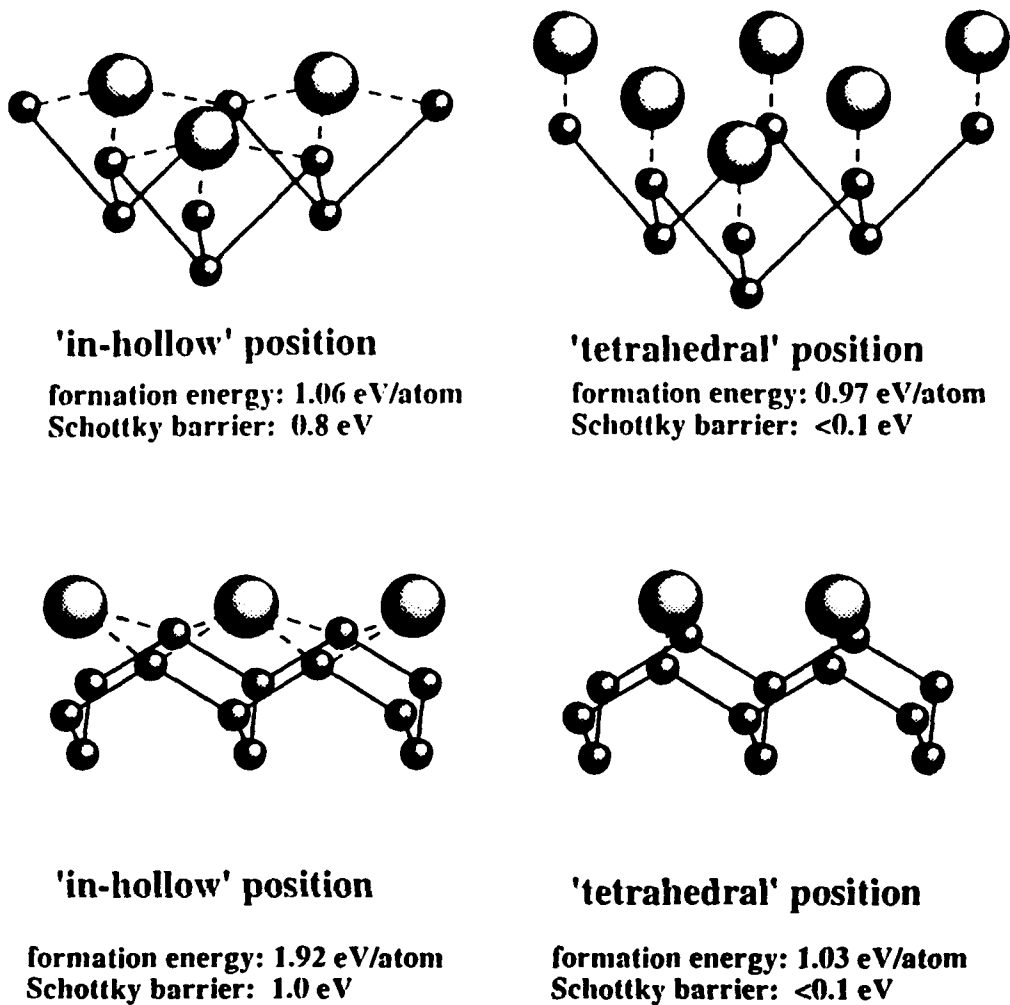
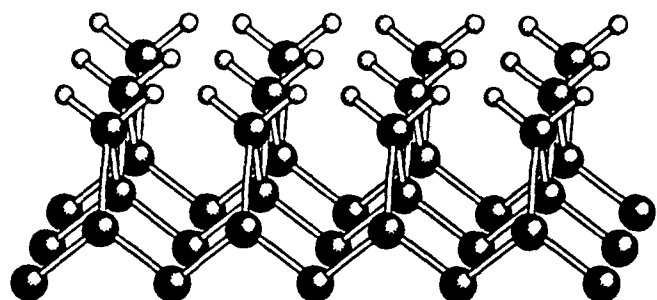


Figure 2. Ball-and-stick models of the various configuration of nickel on diamond (111) and (100)as studies by Erwin and Pickett [49-51, 53].

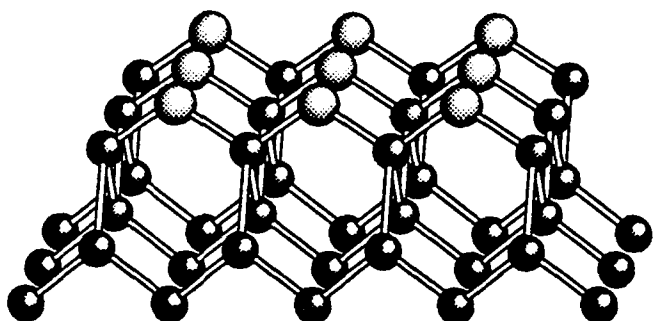
with photoemission spectroscopy, since secondary electrons that are thermalized to the conduction band minimum appear as a sharp peak in the spectra [35, 36, 56-62]. The hydrogen can be removed from the diamond (111) surface, by annealing the surface to $>950^{\circ}\text{C}$. This annealing process typically leads to a $2\times 1/2\times 2$ reconstructed surface, which exhibits a positive electron affinity.

Electron stimulated desorption time-of-flight measurements, reported by Hamza *et al.* [63] suggest that the unreconstructed diamond (100) surface is terminated by a dihydride, as illustrated in Figure 3(a). Hydrogen and oxygen desorption and adsorption studies performed by Thomas *et al.* suggest, however, that a partial oxygen termination may be also occur [64]. Two possible structures were proposed for an oxygen terminated surface, as shown in Figure 3(b) and (c). Both Hamza *et al.* and Thomas *et al.* report that the unreconstructed surface is observed to reconstruct after the surface has been annealed to $\sim 1000^{\circ}\text{C}$. Electron stimulated desorption time-of-flight measurements, performed by Hamza *et al.*, indicate that there is still

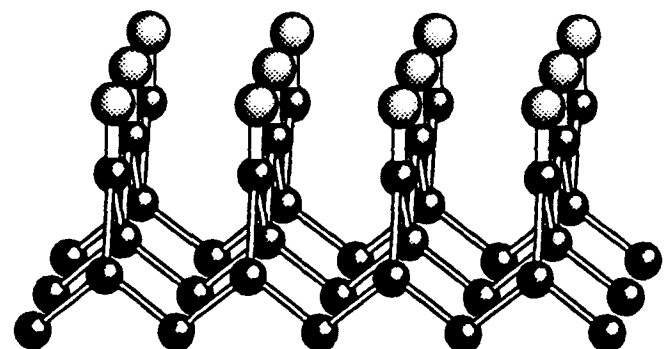
hydrogen present at the reconstructed surface [63]. It is therefore suggested that the 2x1 reconstructed surface is terminated by a monohydride.



(a) Diamond (100) 1x1:2H Dihydride structure



(b) Diamond (100) 1x1:O Bridging structure



(c) Diamond (100) 1x1:O Double-bonded structure

Figure 3. Ball-and-stick models of dihydride (a) [63] and oxygen (b and c) [64] terminated diamond (100) surfaces, resulting in an 1x1 surface structure.

B. Experimental

The experiments described here, were performed in the vacuum system depicted in Figure 4. The system consists of four chambers, connected by a vacuum transfer system. This system allows the use of a variety of analysis techniques and sample preparation techniques without exposing the samples to air. The four chambers include a plasma chamber, a LEED/AES chamber, an angle resolved ultraviolet photoemission spectroscopy (ARUPS) chamber, and a molecular beam epitaxy (MBE) chamber. A load lock allows the introduction of samples, without corrupting the vacuum.

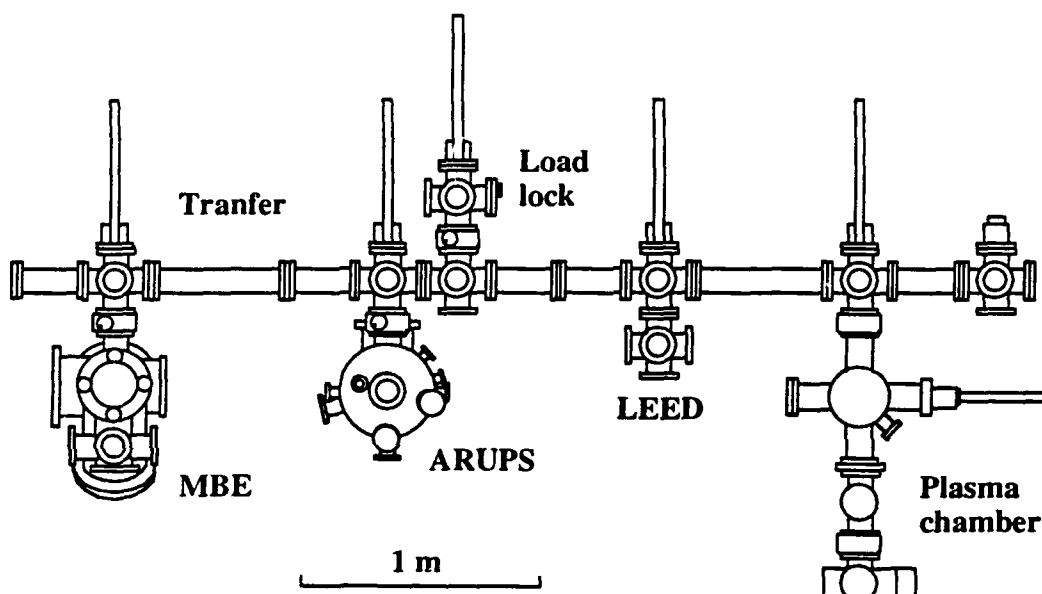


Figure 4. Schematic of the vacuum equipment used in the experiments.

A central feature of the transfer system is a glider, which can hold up to three sample holders. The glider is mounted on four Teflon™ bearings and moves on two rails. It can be pulled back and forth by a stainless steel wire. Sample holders are loaded on the glider or introduced into the chambers, by magnetic push rods. Transfers between the various chambers can be typically performed in less than 5 minutes. The base pressure of the transfer system is 2×10^{-9} Torr.

The plasma chamber is used to generate both hydrogen and argon plasmas. These gasses are introduced into the plasma chamber through a 25 mm diameter quartz tube. A 12 turn coil around the tube is used to couple RF power inductively into the plasma. The gas pressure in the chamber is regulated by a turbo pump backed throttle valve. Samples face the plasma region, and are located at ~40 cm from the end of the quartz tube. Samples are heated by a

tungsten filament in close proximity to the back of the sample while they are exposed to the plasma.

Photoemission spectroscopy is performed in the ARUPS chamber. Photoemitted electrons are excited by ultraviolet radiation, generated in a differentially pumped noble gas discharge lamp. In this study the lamp is operated with helium gas, and the discharge is optimized for HeI radiation which has an energy of 21.21 eV. The photoemitted electrons are analyzed with a 50 mm hemispherical electron analyzer, with an angular resolution of 2°. The analyzer is mounted on a double goniometer, and can be tilted with respect to the surface of the sample in any direction. For the experiments described here the analyzer is positioned normal to the surface, and is operated with an energy resolution of 0.15 eV. The sample is mounted on a heating stage, with a tungsten filament in close proximity to the back of the sample. In the experiments the diamond substrate was mounted on a molybdenum disk. The temperature of the heater is measured at the back of the molybdenum disk with a tungsten-rhenium thermocouple. This temperature measurement is used during experiments to regulate the temperature of the heater. Due to the thermal resistance of the molybdenum disk the actual temperature of the diamond sample is less than the temperature determined with the thermocouple. The thermocouple temperatures were therefore converted to the actual temperatures, as determined by an optical pyrometer. The sample stage is electrically isolated from the rest of the chamber, and can be biased. Bias voltages of up to 1 V were applied in order to allow low energy electrons to overcome the work function of the analyzer. The base pressure in the ARUPS chamber is 5×10^{-10} Torr, which rises to 5×10^{-9} Torr when the discharge lamp is operated.

The MBE chamber contains two electron beam evaporation sources that can be used to evaporate a variety of materials. Each source is equipped with a crystal rate monitor which is used to monitor evaporation rates and film thicknesses. The base pressure of this chamber is 1×10^{-10} Torr which rises to $\sim 1 \times 10^{-8}$ Torr during evaporation.

The diamond substrates used in this study were commercially supplied natural diamond, obtained from Dubbeldee Harris. It was found necessary to use the p-type semiconducting variety of diamond (type IIb), since non-conducting diamond samples (type IIa) did not yield a signal. This is attributed to charging. The diamond substrates measured $3 \times 3 \times 0.5$ mm³ or $4 \times 4 \times 0.5$ mm³, with typical resistivities on the order of 10^4 Ω-cm. The surfaces of two of these substrates were oriented to within 4° of the (111) planes, while the other two surfaces were (100) oriented to within 2°. The wafers were polished with 0.1 μm diamond grit and chemically cleaned before every experiment. The chemical clean consisted of a 10 minute etch in boiling sulfuric acid to remove wax and residues from the polishing. This was followed by 30 minutes in boiling chromic acid to remove graphitic carbon from the surface. The clean was concluded with a de-ionized water rinse, a 10 minute etch in boiling aqua

regia to remove metallic traces, and a final de-ionized water rinse. Just before the wafers were loaded into the vacuum they were given a final hand polish with dry lens paper. The diamonds were fastened to a 1.6 mm thick, 25.4 mm diameter molybdenum disk with tantalum wire.

Once in vacuum the diamond (111) wafers were annealed to temperatures up to 850°C for 10 min. in order to desorb contaminants. After the anneals the wafers were exposed to an argon plasma in the plasma chamber to remove hydrogen bonded to the surface [65] and to obtain a clean surface. The gas flow was kept at 9 sccm while the pressure was held at 14 mTorr. The plasma was excited with 20 W of RF power. The samples were exposed for a duration of 10 minutes at a time. During each exposure the sample was kept at a temperature of ~350°C. After each plasma exposure the sample was transferred into the ARUPS chamber. The absence of a peak, associated with a negative electron affinity surface was used to determine whether the plasma had removed the hydrogen from the surface. The diamond (100) surfaces, which do not show a negative electron affinity after chemical cleaning, were annealed to temperatures ranging from 500°C to 1070°C, before nickel was deposited.

Nickel was deposited in the MBE chamber. Typical evaporation rates were ~10 Å/min. After each deposition the samples were transferred to the ARUPS chamber. The nickel films were deposited at room temperature, and epitaxial growth is not expected to occur, based on growth studies of nickel on diamond (111) and (100) surfaces [46]. In one experiment, however, the film deposited on a (100) surface was annealed to ~370°C for 30 minutes after deposition, which did result in epitaxial growth. Both SEM and STM measurements were attempted on the completed films, to determine whether growth had occurred uniformly. These measurements did not yield significant results, however, apparently due to the fact that the substrates were too resistive for these measurements.

Photoemission spectroscopy is commonly used to measure Schottky barrier heights by determining the relative positions of the valence band edge and the Fermi level of the metal. For the diamond (111) surface the valence band edge can be determined by linear extrapolation of the onset of emission to zero, as depicted in Figure 5. In addition to a clear onset of emission, the diamond (111) surface has been shown to exhibit a negative electron affinity when the surface is hydrogen terminated [56, 58]. The work function of the surface is therefore such, that the energy position of the conduction band edge lies above the energy position of the vacuum. This allows electrons, thermalized at the conduction band minimum to escape from the surface. These electrons appear as a sharp peak, labeled ' E_c ' in Figure 5, at the low energy end of the spectrum. Instead of being determined by the work function, the low energy cut off of the spectrum is now determined by the conduction band edge. The energy position of the valence band edge, labeled ' E_v ' in Figure 5, can be determined from the position of the peak labeled ' E_c '. The onset of emission occurs at $E_v + h\nu$, where $h\nu$ is

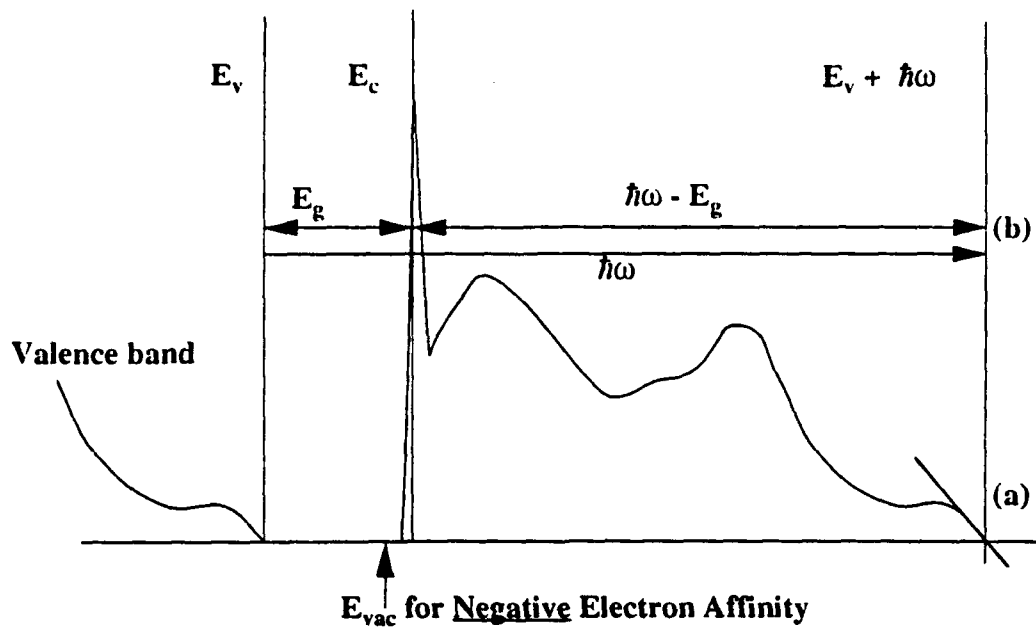


Figure 5. Determination of the valence band edge position ($E_v + h\nu$) in a diamond (111) spectrum by linear extrapolation of the onset of emission (a) and based on the emission from the conduction band edge (b). Emission from the conduction band edge is possible since the surface has a negative electron affinity which puts the vacuum level below the conduction band edge. The emission appears as a sharp peak at the low energy end of the spectrum.

the energy of the light. The conduction band minimum E_c is also related to the valence band edge since $E_c = E_v + E_g$, where E_g is the energy gap in the diamond. The onset of emission should therefore occur at $h\nu - E_g$ above the peak ' E_c ' in the spectrum. The onset of emission, and the peak at ' E_c ' due to the negative electron affinity are therefore two independent means of determining the position of the valence band edge.

The Schottky barrier height can be determined from photoemission spectra, by locating the valence band edge of the semiconductor, and the Fermi level of the metal in the spectra. The determination of the Schottky barrier height from UV photoemission measurements, relies on the fact that features of both the metal and the underlying semiconductor are visible in one spectrum, as shown in Figure 6. Experiments are therefore limited to thin metal films with a thickness on the order of the mean free path of the electrons (~5 Å). Even at metal coverages less than the mean free path, it is not always possible to determine the position of the valence band edge accurately from the spectra, since emission from the metal Fermi level obscures the relatively weak semiconductor valence band emission. In our experiments the valence band edge was determined from the spectrum of the diamond (111) surface before metal deposition and related to a stronger emission feature at 8.2 eV below the valence band edge, labeled 'A' in Figure 6. The spectra of the diamond (100) surfaces do not exhibit a

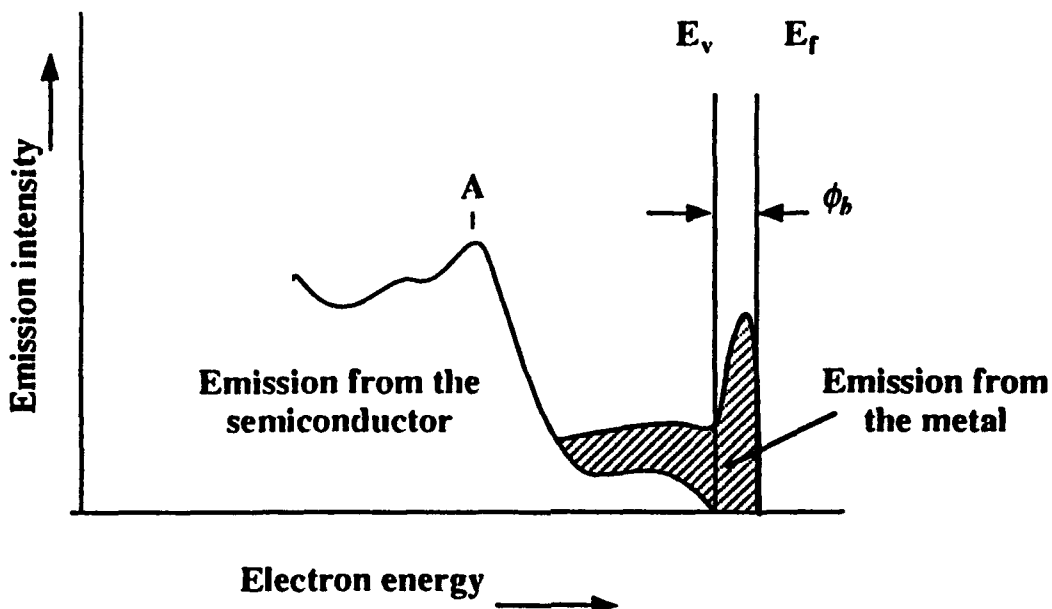


Figure 6. Diagram illustrating how the Schottky barrier height is determined from the photoemission spectra by determining the relative position of the Fermi level of the metal, and the valence band edge of the semiconductor. If the valence band edge can not be resolved directly, it is determined indirectly from the position of stronger features, such as 'A'.

clear onset of emission corresponding to the valence band edge. The spectra do, however, exhibit the feature at 8.2 eV below the valence band edge which is also present in the spectra of the (111) surfaces. The position of this feature on the (100) surface, relative to the valence band edge, was confirmed from spectra of the 2x1 reconstructed diamond (100) surface, which exhibited a negative electron affinity, as discussed below. For both the (111) and the (100) surface this peak remained clearly visible for metal thicknesses on the order of 5 Å. For each spectrum, the position of this peak was found by fitting a Gaussian curve to a selected range of data points. The position of the valence band was then determined from the position of this peak.

In order to measure the Schottky barrier height, the position of the Fermi level of the metal overlayer has to be determined as well. At low coverages the onset of emission is not abrupt as for complete metal films. The Fermi level is therefore determined by linear extrapolation of the onset of the emission intensity to zero.

C. Results

Nickel on diamond (111). A photoemission spectrum, obtained from an argon plasma cleaned diamond (111) surface, is shown in Figure 7. The low energy cut off of the spectrum is positioned ~0.3 eV above the position of the conduction band minimum. The surface exhibits, therefore, a 0.3 eV positive electron affinity. In contrast, a spectrum, obtained from a surface which exhibited a negative electron affinity, as evidenced by a sharp peak at low electron energies, is also shown in Figure 7. The presence of the negative electron affinity effect is attributed to hydrogen chemisorbed onto the surface.

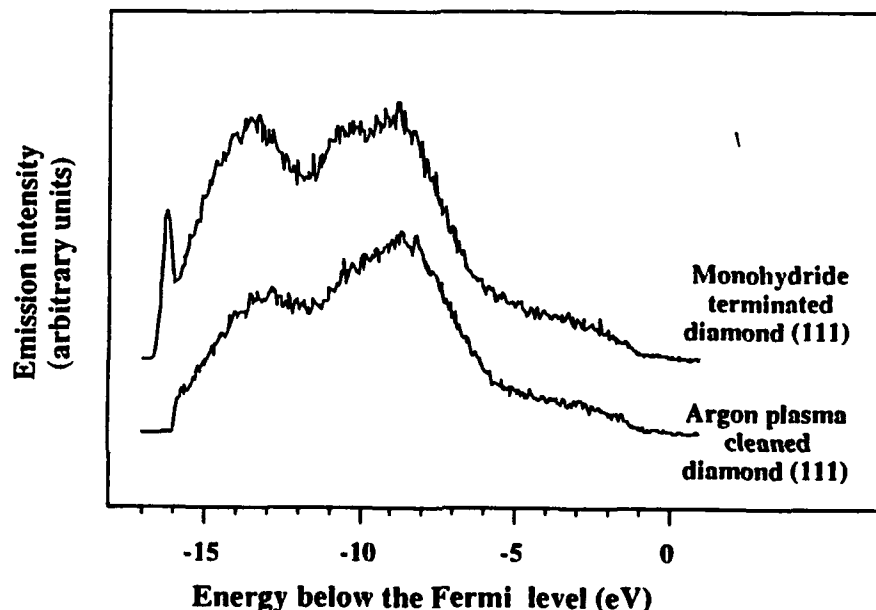


Figure 7. Photoemission spectra of a hydrogen free diamond (111) surface with a positive electron affinity (bottom curve) and hydrogen terminated surface with a negative electron affinity (top curve) resulting in a sharp peak due to emission from the conduction band edge.

Nickel was deposited while the samples were at room temperature. Figure 8 shows typical spectra of the argon plasma cleaned diamond (111) surface, before and after nickel deposition. The spectra obtained after nickel deposition show the emerging Fermi edge of the nickel as the thickness of the nickel film increases. In addition, a peak at the low energy end of the spectrum appears, which is an indication that the surface has a negative electron affinity. The peak reaches a maximum for a film thickness of 1 Å. At that thickness a clear onset of emission due to the Fermi edge of the nickel film can be discerned. Upon nickel deposition a shift of ~0.4 eV towards lower energies is observed in the spectrum of the underlying diamond. In contrast, nickel deposited on the surface that exhibited a negative electron affinity prior to deposition, resulted in a reduction of the negative electron affinity peak, as can be seen in Figure 9.

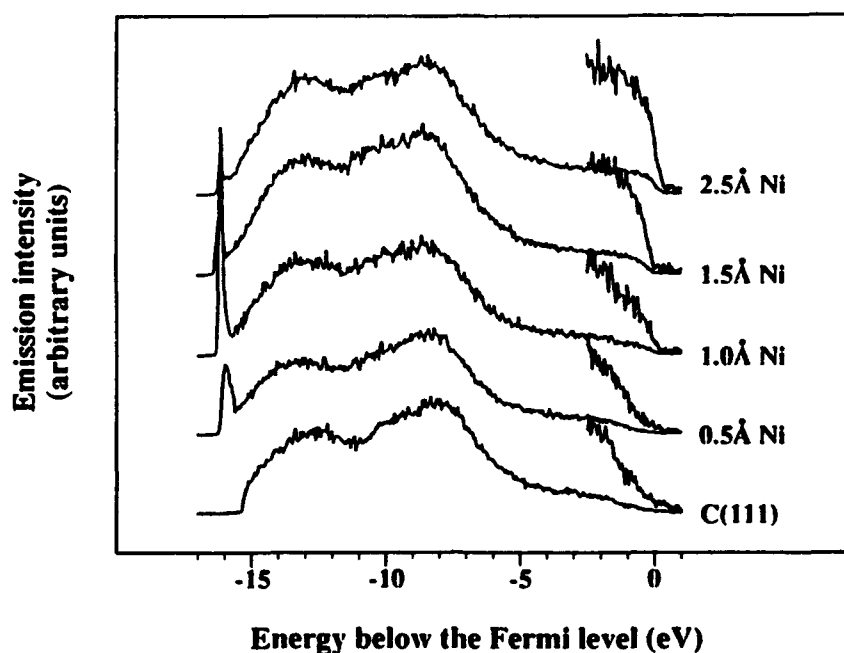


Figure 8. Photoemission spectra of nickel on a hydrogen free diamond (111) surface. A clear Fermi level can be discerned after 1\AA of nickel. The diamond surface exhibits a negative electron affinity after deposition of the first 0.5\AA Nickel, as evidenced by a sharp peak at the low energy end of the spectrum.

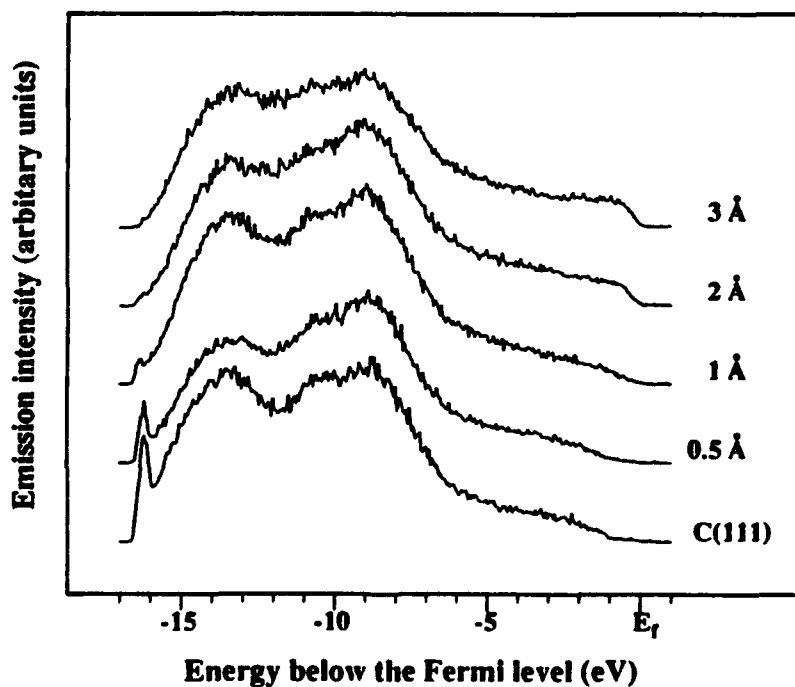


Figure 9. Photoemission spectra of nickel deposited on a hydrogen terminated diamond (111) surface. The negative electron affinity of the original surface is reduced upon nickel deposition.

Schottky barrier heights were determined from the photoemission spectra, and plotted as a function of film thickness in Figure 10. This Figure shows two distinctly different results. The upper data set was obtained from the surface that exhibited a negative electron affinity prior to nickel deposition, and a ~1.0 eV Schottky barrier height is found for nickel on this surface. Nickel deposited on the argon plasma cleaned surface, however, resulted in a ~0.5 eV Schottky barrier height for the first monolayer of nickel. This Schottky barrier height was seen to increase to ~0.7 eV upon further nickel deposition.

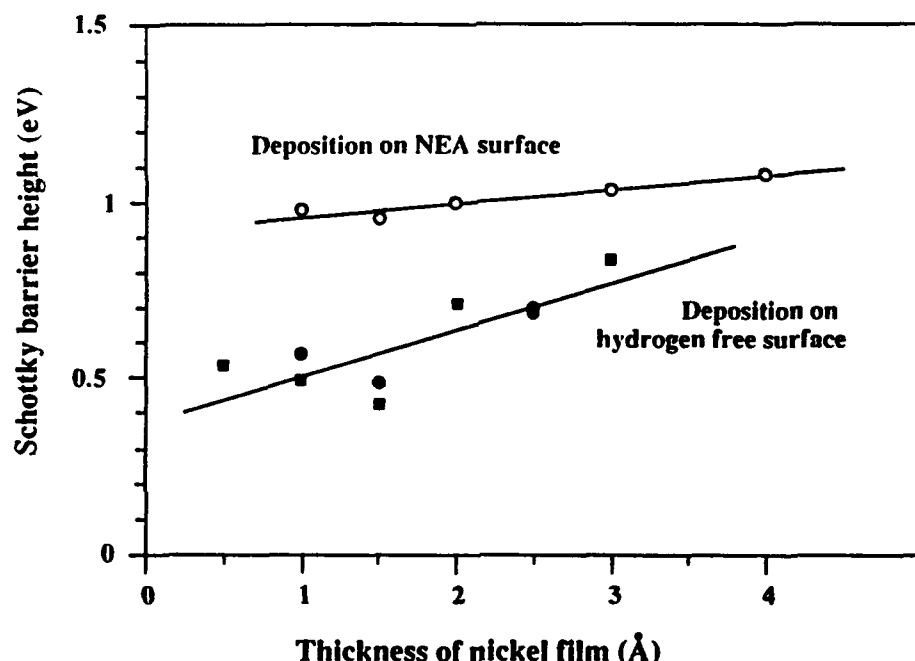


Figure 10. Schottky barrier height of nickel on the diamond (111) surface, as a function of metal thickness. The data in the upper curve was obtained from a hydrogen exposed surface, while the data in the lower curve is associated with a hydrogen free surface.

Nickel on diamond (100). Diamond (100) surfaces were polished and etched, and annealed to temperatures ranging from 500°C to 1070°C. As is shown in Figure 11, auger spectra obtained from the as-loaded surface exhibit a feature indicative of oxygen, which remains present after a 500°C anneal. After a 900°C anneal a reduction in the oxygen feature can be observed, however, in agreement with desorption studies performed by Thomas [64]. After the 900°C anneal the onset of a 2x1 reconstruction is observed, as determined by LEED. Further annealing to 1050°C resulted in a reduction of the amount of oxygen on the surface to below the detection limit of the Auger system, while the LEED pattern of the 2x1 reconstruction is observed to sharpen. It should be mentioned, that Auger spectroscopy measurements are not sensitive to hydrogen, and the presence of hydrogen on the surface is anticipated.

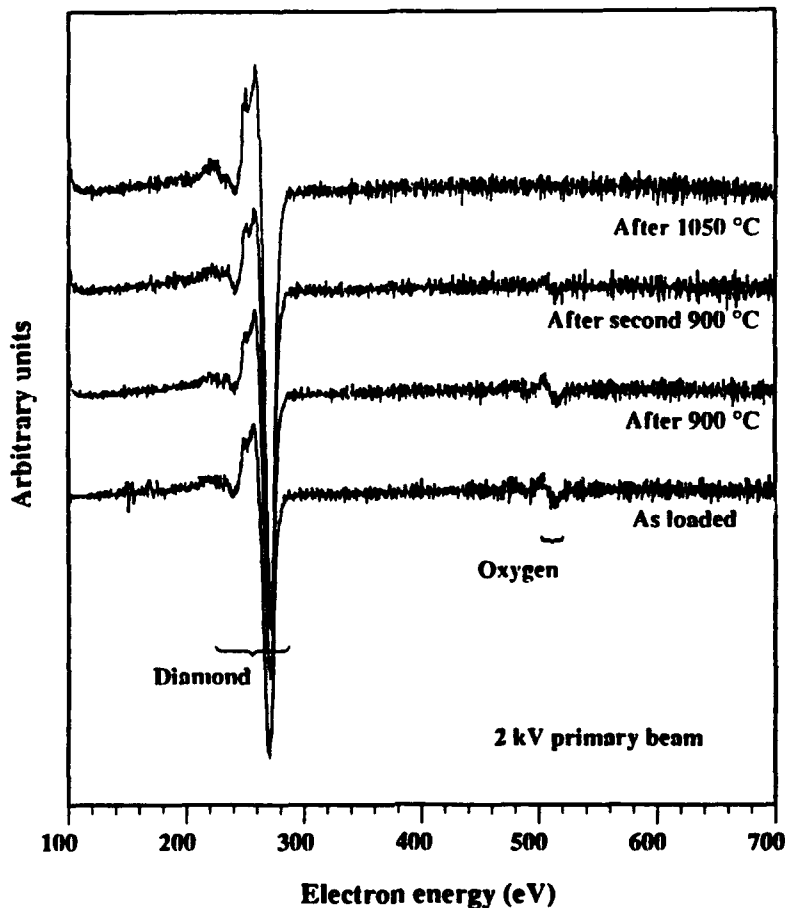


Figure 11. Auger spectra, obtained from the diamond (100) surface, as a function of annealing temperature. The oxygen is observe to evolve at ~900°C.

Photoemission spectroscopy spectra of the diamond (100) surface were obtained from a separate sample, and are shown in Figure 12. The spectra shown in the figure exhibited small, but inconsistent shifts in energy on the order of 0.2 eV, and are therefore aligned with respect to the feature at ~9 eV below the Fermi level. As can be seen in the figure the back edge of the spectra shifts ~1 eV towards lower energies as the diamond (100) is annealed to higher temperatures. This signifies a lowering of the work function, and consequently a lowering of the electron affinity. After a 1035°C anneal a peak appears in the spectra at low electron energies, indicative of a negative electron affinity surface. The peak increased in height upon further annealing to 1070°C.

Nickel was deposited on surfaces that had been annealed to temperatures ranging from 545°C to 860°C, and photoemission spectra were obtained after each deposition. A typical series of spectra is shown in Figure 13. Although the back edge of the spectra is observed to shift towards lower energies, the negative electron affinity effect was not observed to appear upon Nickel deposition. In addition, nickel was deposited on a 2x1 reconstructed surface, obtained by annealing the surface to 1070°C. After each deposition of nickel on this surface,

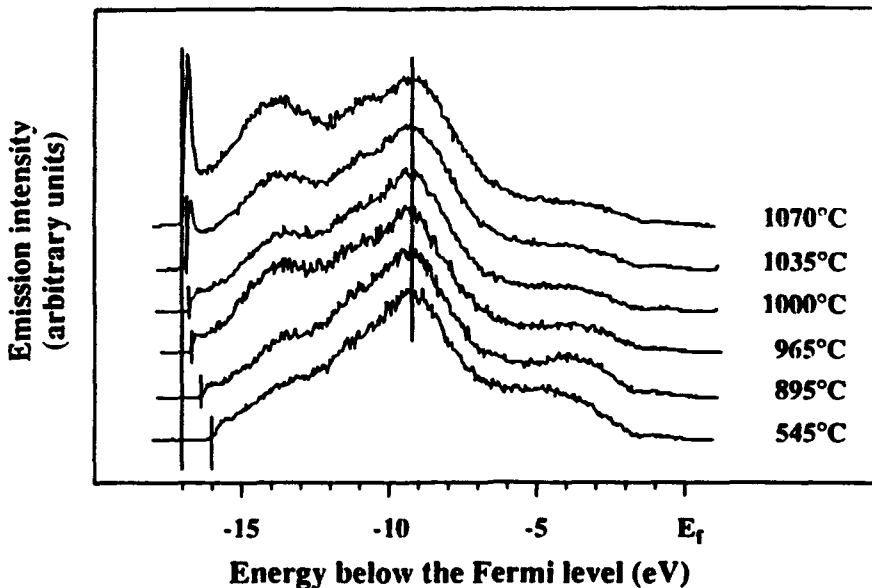


Figure 12. Photoemission spectra showing the effects of annealing on the diamond (100) surface. The shift in the back edge is indicative of a lowering of electron affinity, and is associated with a change of the surface from a dihydride to a monohydride terminated surface. A faint 2x1 reconstruction was observed after the 1000°C anneal, which became sharper after the 1070°C anneal. The spectra have been lined up according to peak at ~9 eV below the Fermi level.

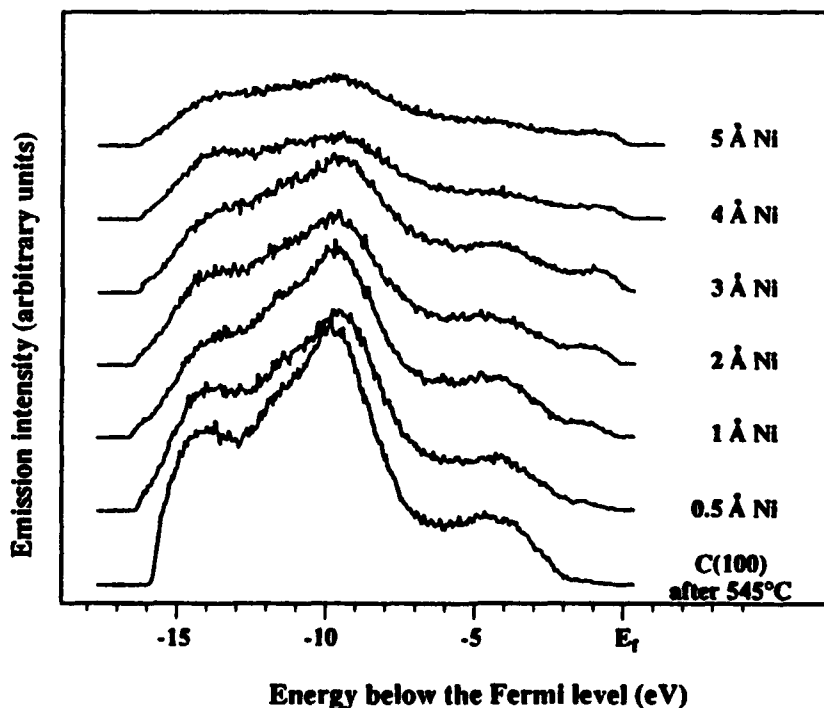


Figure 13. Photoemission spectra of nickel deposited on diamond (100) after the surface had been annealed to 545°C. Upon nickel deposition the work function of the surface is reduced, resulting in a shift of the low energy cut-off of the spectrum.

the film was annealed to $\sim 370^{\circ}\text{C}$. As is displayed in Figure 14, the negative electron affinity peak was slightly reduced, but remained visible after 2 Å of nickel had been deposited. After further nickel deposition the peak disappears. After ~ 35 Å of nickel had been deposited, the sample exhibited a (100) 1x1 LEED pattern, indicating that the film was grown epitaxially. Schottky barrier heights of the nickel-diamond (100) interface were determined from the photoemission spectra, and are plotted as a function of film thickness, in Figure 15. As can be seen, the Schottky barrier height is reduced from ~ 1.5 eV for nickel on the 545°C annealed surface, to ~ 0.7 eV for nickel on the 1070°C annealed surface. It is of interest to note that the change in Schottky barrier height corresponds to a change in the electron affinity of the surface prior to the nickel deposition.

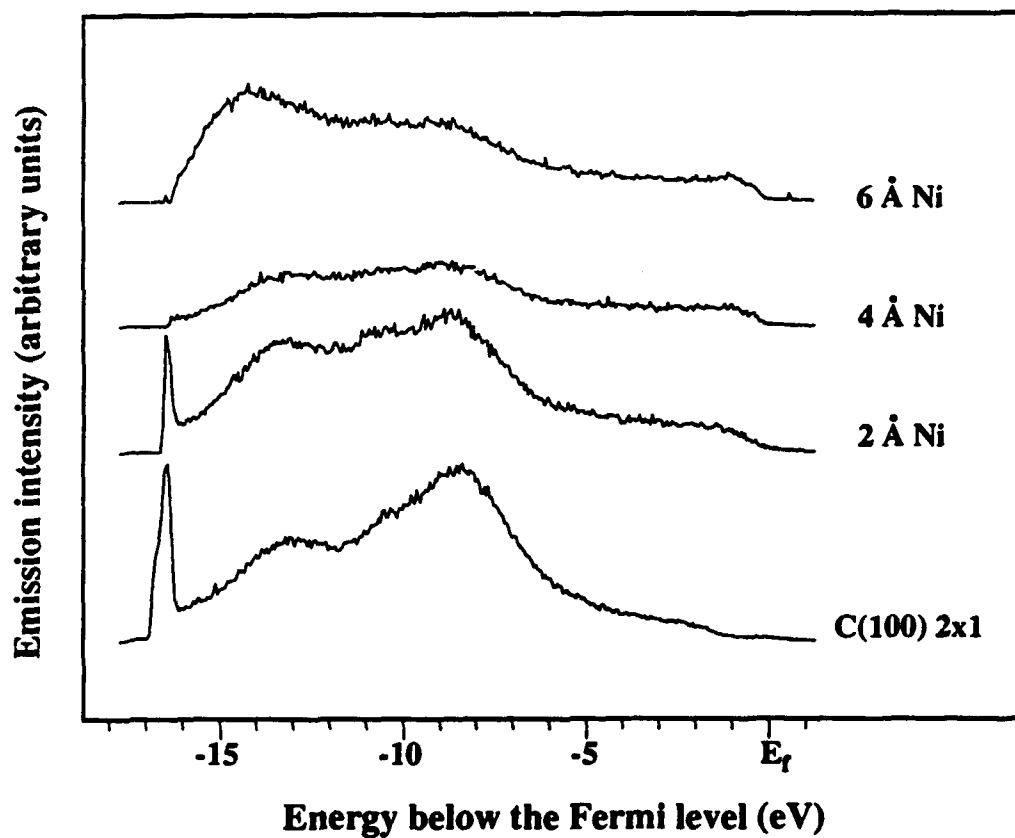


Figure 14. Photoemission spectra of nickel deposited on 2x1 reconstructed diamond (100).

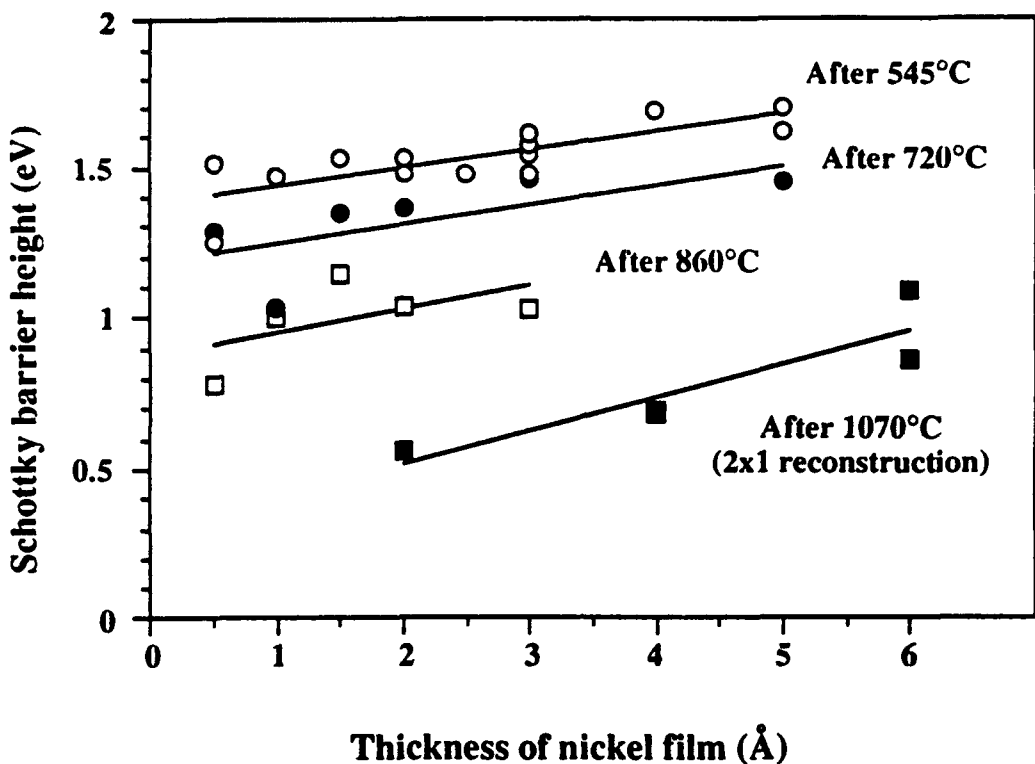


Figure 15. Schottky barrier height of nickel on diamond (100) as a function of metal thickness. The different data sets were obtained after the substrates had been annealed to the temperatures indicated in the figure.

D. Discussion

Nickel on diamond (111). From the results presented here, the Schottky barrier height for nickel on the hydrogen-free diamond (111) surface was found to be ~0.5 eV. Theoretical calculation performed by Erwin and Pickett indicate, however, that the interface structure with the lowest formation energy, nickel in the ‘tetrahedral’ position, results in a Schottky barrier height of <0.1 eV. It should be noted, however, that the formation energy of the ‘tetrahedral’ structure (0.97 eV/atom) is almost identical to the formation energy of the ‘in-hollow’ structure (1.06 eV/atom). There is, however, a significant difference between the calculated Schottky barrier heights for nickel in these two structures. For the ‘tetrahedral’ position, which is energetically the most favorable, a Schottky barrier height of <0.1 eV is found, while the ‘in-hollow’ position leads to a predicted Schottky barrier height of 0.8 eV. Since nickel does not grow epitaxially at room temperature on the (111) surface [46], and in light of the fact that the two proposed formations are so close in formation energy, we suggest the possibility that both formations could occur at the interface. That would result in an effective Schottky barrier height between <0.1 eV and 0.8 eV, which is in general agreement with our experimental value of 0.5 eV.

The influence of interfacial hydrogen on the Schottky barrier has been studied by Lambrecht [54], who performed calculations on the copper-diamond (111) interface. Copper, like nickel has an FCC lattice, that closely matches the lattice of diamond, and the two elements are expected to behave in a very similar fashion. This is borne out by the fact that the calculations of Lambrecht for copper on diamond (111) lead to very similar results as the ones done on nickel by Erwin and Pickett. Lambrecht finds a nearly zero Schottky barrier height for copper in the ‘tetrahedral’ position, while a Schottky barrier height of ~ 0.5 eV is found for the ‘in hollow’ position. His calculations of copper on hydrogen terminated (111) diamond, however, result in a theoretical Schottky barrier of more than 1 eV. This agrees with our results, which suggest that the presence of hydrogen at the surface leads to a higher Schottky barrier.

The possibility was considered that the negative electron affinity observed after the nickel deposition was the result of a lowering of the work function of the surface due to the nickel. A similar effect has been reported for titanium on the diamond (111) surface [37]. In order for this to occur the sum of the Schottky barrier height and the work function has to be less than the bandgap of the semiconductor, as illustrated in Figure 16. With a Schottky barrier height of 0.5 eV and a bandgap of 5.47 eV that would mean that the nickel work function would have to be less than 5.0 eV. The reported value for the nickel work function of crystalline films is 5.15 ± 0.1 eV [66]. It is of interest to note, however, that the presence of carbon contamination tends to lower the work function of the nickel [67]. This suggests the

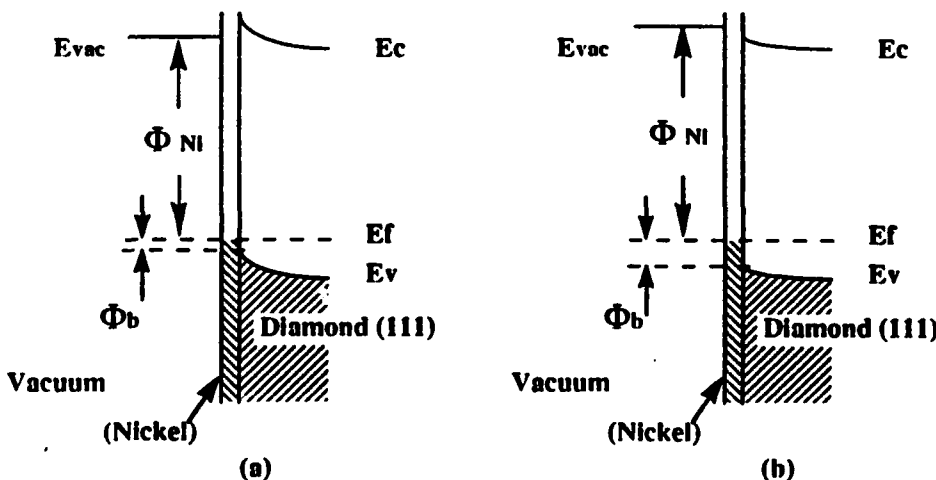


Figure 16. Band diagrams of the nickel-diamond interface. In (a) the sum of the Schottky barrier height and work function for nickel on diamond are less than the band gap of diamond, resulting in a negative electron affinity, while in (b) the sum is larger than the band gap, resulting in a positive electron affinity.

possibility that the carbon from the diamond substrate affects the work function of the first layer of nickel. For the nickel deposited on the hydrogen terminated (111) surface, a Schottky barrier height of ~1.0 eV was found, which, according to our model, would result in a 0.5 eV positive electron affinity. This is in agreement with the observed disappearance of the negative electron affinity feature upon nickel deposition, as can be seen in Figure 9.

Nickel on diamond (100). As discussed in the introduction, the unreconstructed diamond (100) surface can be obtained by terminating the surface with either a dihydride or with an oxide. Oxygen is observed on the (100) surface and is stable for annealing temperatures of at least 500°C. It is, therefore, unlikely that the oxygen is adsorbed on the surface in the form of a molecule, such as O₂ or H₂O. When oxygen is desorbed after a 900°C anneal, the surface is observed to reconstruct. We, therefore, suggest that this oxygen is chemically bonded to the surface, in one of the two structures proposed by Thomas *et al.* (see Figure 3(b) and (c)). The presence of a dihydride phase, illustrated in Figure 3(a) can not be ruled out however, since Auger is not sensitive for hydrogen, and we suggest that both phases occur at the surface. We attribute the lowering of the work function of the diamond (100) surface as a function of annealing temperature, to the desorption of the adsorbed species. The negative electron affinity, observed on the 2x1 reconstructed surface, is attributed to a monohydride terminated surface structure, based on the results reported by Hamza *et al.* [63]. This is supported by preliminary pseudo-potential calculations, performed by Zhang *et al.* which indicate that the 2x1 monohydride terminated surface exhibits a 0.62 eV negative electron affinity [68]. We assign, therefore, a Schottky barrier height of ~1.5 eV to nickel on a hydrogen/oxygen terminated diamond (100) surface, with the possibility that a dihydride phase is present on the surface as well. A Schottky barrier height of ~0.7 eV is assigned to the nickel on 2x1 reconstructed, monohydride terminated diamond (100). The Schottky barrier, for both the nickel on the reconstructed, and the unreconstructed surface, is too large to induce an negative electron affinity. The measured Schottky barriers, of the nickel-diamond (100) interface, do not agree with theoretical calculations performed by Erwin and Picket, which predict a zero Schottky barrier height [49-52]. Their calculations, however, are based on a ideal hydrogen free diamond (100) surface. To our knowledge there are no theoretical studies on the effects of hydrogen on the Schottky barrier height of metals on the diamond (100) surface.

E. Conclusions

Using photoemission spectroscopy we have investigated the nickel-diamond interface. An argon plasma was used to obtain a hydrogen free diamond (111) surface, and a Schottky barrier height of ~ 0.5 eV was found after deposition of a monolayer of nickel. After the nickel deposition the surface exhibited a negative electron affinity. Further nickel deposition

resulted in a slight increase in the Schottky barrier height to ~0.7 eV. A model is presented to account for the observed negative electron affinity effect. When hydrogen was present on the surface, an increased Schottky barrier height of 1.0 eV was observed. This agrees with theoretical calculations performed on the copper-diamond (111) interface. Diamond (100) surfaces were subjected to various anneals, which resulted in a reduction of oxygen and hydrogen, bonded to the surface, and a lowering of the electron affinity as the annealing temperature was increased. After the diamond (100) surface had been annealed at temperatures above 1000°C, the surface was reconstructed and exhibited a negative electron affinity. Schottky barrier heights for nickel on the diamond (100) surface were observed to vary from ~1.5 eV for the 545°C annealed unreconstructed surface, to ~0.7 eV for the 1070°C reconstructed surface. These variations were attributed to different amounts of oxygen and hydrogen, bonded at the metal-diamond interface.

F. References

1. H. Shiomi, Y. Nishibayashi and N. Fujimori, Jap. J. Appl. Phys. **28**, L2153 (1989).
2. H. Shiomi, Y. Nishibayashi and N. Fujimori, Jap. J. Appl. Phys. **29**, L2163 (1990).
3. G.S. Gildenblat, S.A. Grot, C.W. Hatfield and A.R. Badzian, IEEE Electr. Dev. Lett. **12**, 37 (1991).
4. W. Tsai, M. Delfino, D. Hodul, M. Riaziat, L.Y. Ching, G. Reynolds and C.B. Cooper III, IEEE Electr. Dev. Lett. **12**, 157 (1991).
5. H. Kiyota, K. Okano, T. Iwasaki, H. Izumiya, Y. Akiba, T. Kurosu and M. Iida, Jpn. J. Appl. Phys. **30**, 2015 (1991).
6. J.F. Prins, Appl. Phys. Lett. **41**, 950 (1982).
7. Y. Tzeng, T. H. Lin, J. L. Davidson and L. S. Tan, *1987 University/Government/Industry Microelectronics Symposium*, p. 290
8. K. Das, V. Venkatesan, K. Miyata, D. L. Dreifus and J. T. Glass, Thin Solid Films **212**, 19 (1992).
9. F. Fang, C. A. Hewett, M. G. Fernandes and S. S. Lau, IEEE Trans. Electr. Dev. **36**, 1783 (1989).
10. M.W. Geis, D.D. Rathman, D. J. Ehrlich, R. A. Murphy and W. T. Lindley, IEEE Electr. Dev. Lett. **8**, 341 (1987).
11. G. S. Gildenblat, S.A. Grot, C.R. Wronski, A.R. Badzian, T. Badzian and R. Messier, Appl. Phys. Lett. **53**, 586 (1988).
12. G. S . Gildenblat, S. A. Grot, C. W. Hatfield, A. R. Badzian and T. Badzian, IEEE Electr. Dev. Lett. **11**, 371 (1990).
13. J. W. Glesener, A. A. Morrish and K.A. Snail, J. Appl. Phys. **70**, 5144 (1991).
14. G. H. Glover, Solid-State Electr. **16**, 973 (1973).
15. S.A. Grot, G.S. Gildenblat, C.W. Hatfield, C.R. Wronski, A. R. Badzian, T. Badzian and R. Messier, IEEE Electr. Dev. Lett. **11**, 100 (1990).
16. M.C. Hicks, C.R. Wronski, S. A. Grot, G. S. Gildenblat, A. R. Badzian, T. Badzian and R. Messier, J. Appl. Phys. **65**, 2139 (1989).
17. P.R. de la Houssaye, C. Penchina, C. A. Hewett, R. G. Wilson and J. R. Zeidler, *New Diamond Science and Technology*, edited by R. Messier, J. T. Glass, J. E. Butler and R. Roy (Materials Research Society, Pittsburgh, 1991), p. 1113
18. T. P. Humphreys, J. V. LaBrasca, R. J. Nemanich, K. Das and J. B. Posthill, Jap. J. Appl. Phys. A **30**, L 1409 (1991).
19. M. Marchywka, J. F. Hochedez, M. W. Geis, D. G. Socker, D. Moses and R. T. Goldberg, Appl. Opt. **30**, 5011 (1991).

20. K. L. Moazed, R. Nguyen and J. R. Zeidler, IEEE Elect. Dev. Lett. **9**, 350 (1988).
21. K. L. Moazed, J. R. Zeidler and M. J. Taylor, J. Appl. Phys. **68**, 2246 (1990).
22. K. L. Moazed, J. R. Zeidler and M. J. Taylor, Mat. Res. Soc. Symp. Proc. **162**, 347 (1990).
23. Y. Mori, H. Kawarada and A. Hiraki, Appl. Phys. Lett. **58**, 940 (1991).
24. J. F. Prins, J. Phys. D **22**, 1562 (1989).
25. H. Shiomi, H. Nakahata, T. Imai, Y. Nishibayashi and N. Fujimori, Jap. J. Appl. Phys. **28**, 758 (1989).
26. T. Tachibana, B. E. Williams and J. T. Glass, Phys. Rev. B **45**, 11968 (1992).
27. T. Tachibana, B. E. Williams and J. T. Glass, Phys. Rev. B **45**, 11975 (1992).
28. G. Zhao, T. Stacy, E. J. Charlson, E. M. Charlson, C. H. Chao, M. Hajsaid and J. Meese, Appl. Phys. Lett. **61**, 1119 (1992).
29. S.A. Grot, S. Lee, G. S. Gildenblat, C. W. Hatfield, C. R. Wronski, A. R. Badzian, T. Badzian and R. Messier, J. Mat. Res. **5**, 2497 (1990).
30. M. W. Geis, M. Rothschild, R. R. Kunz, R. L. Aggarwal, K. F. Wall, C. D. Parler, K. A. McIntosh, N. N. Efremow, J. J. Zaykowski, D. J. Ehrlich and J. E. Butler, Appl. Phys. Lett. **55**, 2295 (1989).
31. J. van der Weide and R. J. Nemanich, *Applications of diamond films and related materials*, edited by Y. Tzeng, M. Yoshikawa, M. Murakawa and A. Feldman (Elsevier, Amsterdam, 1991), p. 359.
32. C. A. Hewett, J. R. Zeidler, M. J. Taylor, C. R. Zeisse and K. L. Moazed, *New Diamond Science and Technology*, edited by R. Messier, J. T. Glass, J. E. Butler and R. Roy (Materials Research Society, Pittsburgh, 1991), p. 1107.
33. D. G. Jeng, H. S. Tuan, R. F. Salat and G. J. Fricano, J. Appl. Phys. **68**, 5902 (1990).
34. C. A. Mead and T. C. McGill, Phys. Lett. A **58**, 249 (1976).
35. F. J. Himpel, D. E. Eastman and J. F. van der Veen, J. Vac. Sci. Technol. **17**, 1085 (1980).
36. F. J. Himpel, P. Heimann and D. E. Eastman, Solid State Comm. **36**, 631 (1980).
37. J. van der Weide and R. J. Nemanich, J. Vac. Sci. Technol. B **10**, 1940 (1992).
38. T. Tachibana, J. T. Glass and R. J. Nemanich, J. Appl. Phys. **73**, 835 (1993).
39. D. N. Belton and S. J. Schmieg, J. Appl. Phys. **66**, 4223 (1989).
40. D. N. Belton and S. J. Schmieg, Thin Solid Films **212**, 68 (1992).
41. S. Kasi, H. Kang and J. W. Rabalais, Phys. Rev. Lett. **59**, 75 (1987).
42. Y. H. Lee, K. J. Bachmann, J. T. Glass, Y. M. LeGrice and R. J. Nemanich, Appl. Phys. Lett. **57**, 1916 (1990).
43. S. T. Lee, S. Chen, J. Agostinelli and G. Braunstein, Appl. Phys. Lett. **60**, 2213 (1992).
44. Y. Saito, K. Sato, S. Matsuda and H. Koinuma, J. Mater. Sci **26**, 2441 (1991).
45. P. G. Lurie and J. M. Wilson, Surf. Sci. **65**, 453 (1977).
46. P. Pavlidis, Thin Solid Films **42**, 221 (1977).
47. W. Zhu, P. C. Yang and J. T. Glass, submitted to Appl. Phys. Lett. (1993).
48. P. C. Yang, W. Zhu and J. T. Glass, Submitted to: J. Mater. Res. (1993).
49. S. C. Erwin and W. E. Pickett, Surf. Coat. Technol. **47**, 487 (1991).
50. S. C. Erwin and W. E. Pickett, Solid State Commun. **81**, 891 (1992).
51. W. E. Pickett and S. C. Erwin, Phys. Rev. B **41**, 9756 (1990).
52. W. E. Pickett and S. C. Erwin, Superlat. Microstruct. **7**, 335 (1990).
53. W. E. Pickett, M. R. Pederson and S. C. Erwin, Mater. Sci. Eng. B. **14**, 87 (1992).
54. W. R. L. Lambrecht, Preprint (1993).
55. A. V. Hamza, G. D. Kubiak and R. H. Stulen, Surf. Sci. **206**, 1 (1988).
56. B. B. Pate, M. H. Hecht, C. Binns, I. Lindau and W. E. Spicer, J. Vac. Sci. Technol. **21**, 364 (1982).
57. B. B. Pate, Surf. Sci. **165**, 83 (1986).
58. B. B. Pate, B. J. Waclawski, P. M. Stefan, C. Binns, T. Ohta, M. H. Hecht, P. J. Jupiter, M. L. Shek, D.T. Pierce, N. Swanson, R.J. Celotta, G. Rossi, I. Lindau and W.E. Spicer, Physica B **117 & 118**, 783 (1983).

59. F. J. Himpel, J. A. Knapp, J. A. van Vechten and D. E. Eastman, Phys. Rev. B **20**, 624 (1979).
60. F. J. Himpel, J. F. van der Veen and D. E. Eastman, Phys. Rev. B **22**, 1967 (1980).
61. B. B. Pate, W. E. Spicer, T. Ohta and I. Lindau, J. Vac. Sci. Technol. **17**, 1087 (1980).
62. B. B. Pate, P. M. Stefan, C. Binne, P. J. Jupiter, M. L. Shek, I. Lindau and W. E. Spicer, J. Vac. Sci. Technol. **19**, 349 (1981).
63. A. V. Hamza, G. D. Kubiak and R. H. Stulen, Surf. Sci. **237**, 1 (1990).
64. R. E. Thomas, R. A. Rudder and R. J. Markunas, J. Vac. Sci. Technol. A **10**, 2451 (1992).
65. J. van der Weide and R. J. Nemanich, Appl. Phys. Lett. **62**, 1878 (1993).
66. D. E. Eastman, Phys. Rev. B **2**, 1 (1970).
67. C. Weiser, Surf. Sci. **20**, 143 (1970).
68. Z. Zhang, M. G. Wensell and J. Bernholc, Personal communication (1993).

XIII. Ohmic and Schottky Contacts to n-type Alpha (6H) Silicon Carbide

A. Introduction

Metal-semiconductor interfaces are critical components of any electronic device. For efficient operation of electronic devices, it is necessary to fabricate both rectifying contacts with low leakage currents and ohmic contacts with low contact resistance. These characteristics require high and low Schottky barrier heights (SBH), respectively.

Although SiC devices have been used for high-power, -temperature, -speed, -frequency, radiation hard, and opto-electronic applications for several years, little is known about the science of controlling metal/SiC contact properties. In this research project several metal/SiC systems are being studied in terms of interfacial chemistry, structure, and electronics. This report discusses electrical properties and high resolution transmission electron microscopy results of four metal contacts before and after annealing.

B. Experimental Procedure

Vicinal single crystal, nitrogen-doped, n-type ($\sim 10^{18} \text{ cm}^{-3}$) substrates of 6H-SiC containing 0.5–0.8 μm thick, nitrogen-doped ($\sim 10^{16} \text{ cm}^{-3}$ unless otherwise noted) homoepitaxial films were provided by Cree Research, Inc. The Si-terminated (0001) surface, tilted 3° – 4° towards [1120] was used for all depositions and analyses.

The substrate surfaces were cleaned in sequence using a 10 min. dip in either 10% HF in deionized water or a (10:1:1) solution of ethanol / HF / H_2O followed by a 15 min. thermal desorption at 700°C in ultra-high vacuum (UHV). The metals were deposited on chemically cleaned, unheated substrates by electron beam evaporation (base pressure $< 2 \times 10^{-10} \text{ Torr}$). For films less than or equal to $\sim 10 \text{ nm}$, a deposition rate of $\sim 1 \text{ nm/min.}$ was used. For thicker films the rate was increased to $\sim 2 \text{ nm/min.}$ after deposition of the first 10 nm.

For electrical characterization the metals were deposited through a Mo mask in contact with the SiC surface, leaving a patterned metal film. Schottky diodes were fabricated using a mask with 500 μm and 750 μm diameter holes. A large area backside contact served as the ohmic contact.

For the purpose of measuring the specific contact resistance of ohmic contacts, the metal was deposited through a different Mo mask. In this case the epitaxial SiC layer had a carrier concentration of $\sim 10^{18} \text{ cm}^{-3}$. The design of the mask follows the Transmission Line Model (TLM) discussed by Berger [1]. The contact resistance is calculated by comparing the total resistances between contacts of various separations.

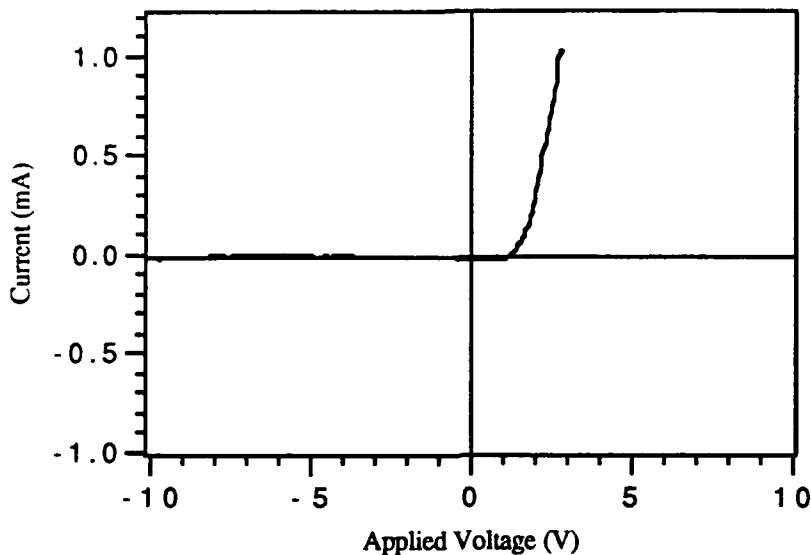
Current-voltage (I-V) measurements were taken with a Rucker & Kolls Model 260 probe station in conjunction with an HP 4145A Semiconductor Parameter Analyzer. Capacitance-

**THIS
PAGE
IS
MISSING
IN
ORIGINAL
DOCUMENT**

*Pages 108
thru 119*

where A^* is the effective Richardson constant for the semiconductor; for this parameter, a value for low-mobility n-GaAs was used (3×10^4 A/m²K²). For the Pt on n-GaN samples, ideality factors ranged from $n=1.7$ to 2.0 and barrier heights from $\phi_b=1.03$ to 1.09 V.

(a)



(b)

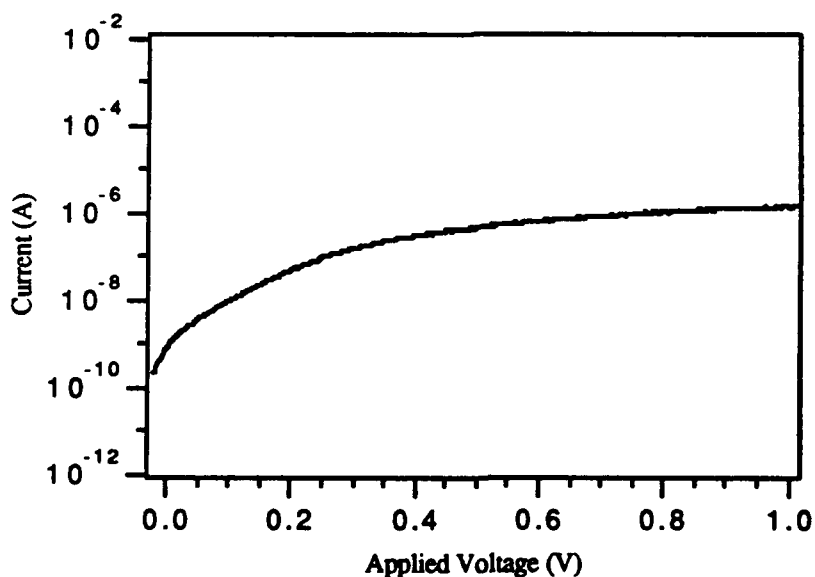


Figure 1. Typical (a) current-voltage and (b) log current-voltage measurements of Pt/n-GaN contacts taken using a small dot-back plane contact combination.

Platinum contacts deposited on p-type GaN did not exhibit ohmic behavior in the as-deposited state. Current-voltage measurements taken across pairs of top contacts and through the back-plane contact revealed less-than-ideal, "leaky" rectifying behavior. Since an ohmic I-V relationship did not exist across the contact interface, it was not possible to take contact resistance measurements using the TLM pattern.

D. Discussion

Platinum contacts deposited on both n-type and p-type GaN were found to be rectifying in the as-deposited state. The nonideality of the I-V and log I-V relationships indicates that a variety of current transport mechanisms were at work. The fact that the Pt/p-GaN contact was rectifying, despite a work function relationship that was favorable to ohmic contact formation, indicates the presence of a potential barrier at the interface.

Experimentally it has been found that the barrier height for a given metal-semiconductor interface is not very dependent on the choice of metal. The presence of additional electron states at the interface can significantly change the junction's electron energy structure; the origins of and mechanisms behind these states are not yet completely understood. Over twenty years ago Kurtin *et al.* described the correlation between the ionicity of a semiconductor's atomic bonding—*i.e.* the relative difference in electronegativity between the elements in a compound—and its surface and interface behavior [12]. The lattice electronegativity differences for GaN and AlN are 1.23 and 1.43, respectively, which correspond to bond ionicities of approximately 32% and 40%. These properties make GaN and AlN significantly more ionic in nature than the more conventional semiconductors; consequently, it is hoped that GaN and AlN will be more sensitive to metal work function differences than the more covalent semiconductors have been.

It has been observed that improving the chemical and morphological abruptness of an interface and making a close match of thermal and mechanical properties is helpful for improving the performance of rectifying contacts. By the same token, extending a gradation of composition and properties at the interface generally improves ohmic contacts. A thin layer of Ti, capped with a thicker layer of Au and then subsequently annealed, is an ohmic contact system that has met with success on a variety of n-type semiconductors over the years, and presents itself as a likely candidate for study. In this study, the next experimental step is to investigate the effects of annealing treatments on the properties of the contacts, in addition to depositing different materials and combinations of materials. Depositions of TiN on both n- and p-type GaN will be conducted shortly.

E. Conclusions

In the as-deposited state, Pt contacts deposited on n-type and p-type GaN have been found to be rectifying in both cases. The I-V and log I-V measurements of the contacts yielded high ideality factor values, indicative of the presence of a variety of current transport mechanisms, and barrier heights of just over 1 eV. These experiments are the first steps in a systematic study of ohmic and Schottky contact formation to GaN and AlN, in which a variety of contact materials will be investigated and a variety of processing and characterization strategies will be brought to bear.

F. Future Plans and Goals

Annealing treatments will be conducted to study the effects of temperature, diffusion, and chemical reactions on the contact interfaces. The thermal stability of a contact is an important characteristic that may place restrictions on device processing parameters and materials selection; in some cases annealing treatments are required to achieve better device characteristics, and in other cases heating steps can cause serious degradation of properties. Electrical characterization of samples by means of I-V and log I-V measurements, capacitance-voltage (C-V) measurements, and Hall effect measurements will be performed. Band structures will be studied by means of electrical measurements, luminescence techniques, and ultraviolet photoelectron spectroscopy (UPS). Structural and chemical characterization will be accomplished by means of high resolution scanning electron microscopy (SEM), X-TEM, XPS, and Auger electron spectroscopy (AES).

Aside from further study of the Pt/GaN and TiN/GaN systems, there are a number of other metalization choices that will be investigated. Titanium-gold and AuGe/Au layered structures are examples of ohmic contact strategies that have been applied with some success to GaAs and other compound semiconductors, and will be examined as likely candidates. Other metals besides Pt, such as Au, Ni, W, Ru, and Re are possible candidates for Schottky contacts. Khan *et al.* recently reported the fabrication of a GaN metal semiconductor field effect transistor (MESFET), using annealed Ti/Au layers as the ohmic source and drain contacts and Ag for the gate Schottky contact [13]. The development of the III-V nitrides as semiconductor device materials is a field that is beginning to move rapidly, and the current literature will be studied closely to keep abreast of any new findings.

G. References

1. M. Murakami, Materials Science Reports (5) 273 (1990).
2. A. Piotrowska and E. Kaminska, Thin Solid Films 193/194 511 (1990).
3. T. C. Shen, G. B. Gao, H. Morkoç, J. Vac. Sci. Technol. B 10(5) 2113 (1992).
4. J. Ding, Z. Liliental-Weber, E. R. Weber, and J. Washburn, Appl. Phys. Lett. 52(25) 2160 (1988).
5. G. Myburg and F. D. Auret, Appl. Phys. Lett. 60(5) 604 (1992).

6. J. Foresi, *Ohmic Contacts and Schottky Barriers on GaN*, M.S. Thesis, Boston University (1992).
7. H. K. Henisch, *Semiconductor Contacts*. (Clarendon Press, Oxford, 1984).
8. E. H. Rhoderick, *Metal-Semiconductor Contacts* (Oxford University Press, New York, 1988).
9. H. H. Berger, Solid State Electronics **15**(2-A) 145 (1972).
10. G. K. Reeves and H. B. Harrison, IEEE Electron Device Lett. **EDL-3** 111 (1982).
11. Sze, *Physics of Semiconductor Devices*, 2nd ed. (John Wiley and Sons, New York, 1981).
12. S. Kurtin, T. C. McGill and C. A. Mead, Phys. Rev. Lett. **22**(26) 1433 (1969).
13. M. Asif Khan, J. N. Kuznia, A. R. Bhattachari, and D. T. Olson, Appl. Phys. Lett. **62**(15) 1786 (1993).

XV. Reactive Ion Etching of GaN and AlN

A. Introduction

Semiconductor devices are the principle components of electronic and telecommunications systems [1]. In order to densely pack these microscopic components, unidirectional, or anisotropic, etching techniques are required to produce a fine network of lines. Wet etching processes found in many semiconductor manufacturing steps produce a multi-directional, or isotropically, etched material. This is undesirable for microcircuitry since the goal is to produce the smallest devices possible. Therefore, plasma-assisted processes, such as reactive ion etching (RIE), combine the physical characteristics of sputtering with the chemical activity of reactive species to produce a highly directional feature. RIE has the added advantage of providing a more uniform etch and a higher degree of material etch selectivity.

RIE has been employed to etch a wide variety of semiconductor materials including silicon-based materials [2–11], metals, like aluminum [3, 12–18] and III-V compounds, such as GaAs and InP [19–21]. However, plasma-assisted etching of newer III-V compounds, such as GaN and AlN, has been attempted by few investigators [20, 21, 37]. There has been wide spread interest in using these nitrides for semiconductor device applications requiring visible light emission, high temperature operation and high electron velocities [20]. Since these materials possess wide bandgaps and optical emissions spectra in the blue to near ultraviolet range, they are prime candidates for ultraviolet detection devices.

The objectives of this report are to discuss recent progress made in the field of reactive ion etching of gallium and aluminum nitride and to describe the reactive ion etching system. A long term goal is to develop and characterize suitable processes for the anisotropic etching of these nitrides. In the following sections, a brief review of pertinent literature on plasma-assisted etching of gallium and aluminum compounds is provided along with a brief description of the reactive ion etching system.

B. Literature Review

Reactive Ion Etching of GaN. Since GaN is a direct transition material with a bandgap ranging from 3.4–6.2 eV at room temperature, it is an ideal candidate for the fabrication of shortwave length light emitters [20, 22]. High quality GaN films have been successfully grown by MOVPE [22], ECR-MBE [23, 24], MOCVD [25] and a layer-by-layer process [26] on a number of substrate. In order to fabricate complete device structures, reliable etching processes need to be developed. Since GaN is nearly inert to most wet etching solutions, with the exception of highly concentrated hot NaOH and H₂SO₄ [27], RIE may prove to be an effective method for the production of fine line patterning in semiconductor materials.

There have been a few reports of etching GaN by plasma-assisted processes [20, 21, 37]. Foresi [21] investigated fabrication techniques for ohmic contact and schottky barriers on GaN. One of the highlights of his work was the successful etching of GaN on sapphire substrate in Freon 12 (CCl_2F_2) and in hydrogen atmospheres operating at about 10 mTorr and 40 and 60 W of RF power. Results from SEM photographs showed that in the CCl_2F_2 plasma, GaN had been completely removed from areas that were not covered by photoresist, and that the sapphire substrate was nearly unetched. Foresi was able to obtain an etch rate of approximately 140 Å/min in the CCl_2F_2 plasma at 60 W, while the hydrogen plasma produced insignificant etching results. Etch selectivity between the GaN and photoresist was found to be 3:1. In another investigation, conducted by Tanaka *et al.* [20] reactive fast atom beam etching was employed to etch GaN on sapphire in a Cl_2 plasma at substrate temperatures ranging between 80–150°C. Etch rates of 1000–1200 Å/min produced relatively smooth surfaces and a well defined pattern of elongated rectangular bars on the sapphire substrate. More recently, S. J. Pearton *et al.* [37] have produced smooth, anisotropically etched GaN and AlN in low pressure ECR discharges of BCl_3/Ar , $\text{CCl}_2\text{F}_2/\text{Ar}$ and $\text{CH}_4/\text{H}_2/\text{Ar}$. The etch rates of these nitrides was highly dependent on the DC bias voltage and ranges of 25–175 Å/min and 0–100 Å/min were reported for GaN and AlN, respectively. It is noted that hydrogen was added to the chlorine plasmas to facilitate removal of hydrogen from the surfaces of the nitride samples, thus producing smoother features.

Reactive Ion Etching of AlN. Aluminum nitride is a candidate material for optoelectronic devices because it possesses a high electrical resistivity, high thermal conductivity, low dielectric constant and has a direct transition bandgap of 6.3 eV [28]. AlN films have been grown by several techniques including CVD, MBE and ALE, and on a variety of substrate materials including sapphire, silicon, spinel, silicon carbide and quartz [29]. Etching fine features in the AlN films is an important step in the fabrication of such devices. Though, only one report of etching of AlN is available in the open literature at this time [37], much work has been conducted on etching of metallic aluminum thin films [3, 12–18]. As a result, analogies to well established data for etching of aluminum are made. Although aluminum and AlN are very different materials, the chemistry and reactions in the plasma may be similar. So, it is proposed that reactive ion etching may also be an effective means for the application of fine line patterning of AlN.

A review of the literature shows that there are two primary methods employed for etching aluminum. Bruce and Malafsky [12] employed a parallel plate configuration (RIE) to investigate the effects of Cl_2 on aluminum. They found that two processes are involved, namely, the removal of the oxide layer and etching the metal below it. For those experiments, it was hypothesized that BCl_3 gas was necessary for the removal of the oxide layer because it was responsible for the initiation of a reduction reaction with the oxide. In the RIE etching

configuration, aluminum etched with a chlorinated gas is a purely chemical reaction with little contribution from ion bombardment. This conclusion was made as a result of the insensitivity of RF power to the etch rate [12]. Therefore, anisotropic etching was thought to have been the result of a sidewall passivation mechanism whereby a protective layer is formed on the vertical walls of the trench by reaction of H₂O or carbon containing species with the aluminum. Since ion bombardment is normal to the surface, the walls remained unetched. This mechanism was produced by the addition of CHCl₃ to the mixture of gases. Feature widths of 2.25 μm were produced by a gas mixture of Cl₂, BCl₃, CHCl₃ and He at about 1.2 mTorr. Helium gas was added to the mixture to reduce the amount of erosion of the photoresist.

The combination of an isotropic flux of reactive species with a highly directional beam of energetic ions, so called ion beam assisted etching (IBAE), has been employed for the anisotropic etching of aluminum by many investigators [13–15, 18]. For IBAE, the aluminum oxide layer can be physically removed by sputtering with Ar⁺ or Xe⁺ ions, whereas with RIE the oxide is removed chemically [13]. However, etching takes place again by chemical reaction of Cl₂ with the aluminum as determined by the lack of dependence of the etch rate on the ion energy and current [14, 15]. From a mechanistic point of view, Cl₂ adsorbs onto and diffuses into the aluminum resulting in the formation of aluminum chlorides. Al₂Cl₆ is the dominant etch product at lower temperatures (33°C), while AlCl₃ was observed at higher temperatures (210°C) [15]. Saturation of the etched surface with chlorine atoms occurs prior to desorption of AlCl₃.

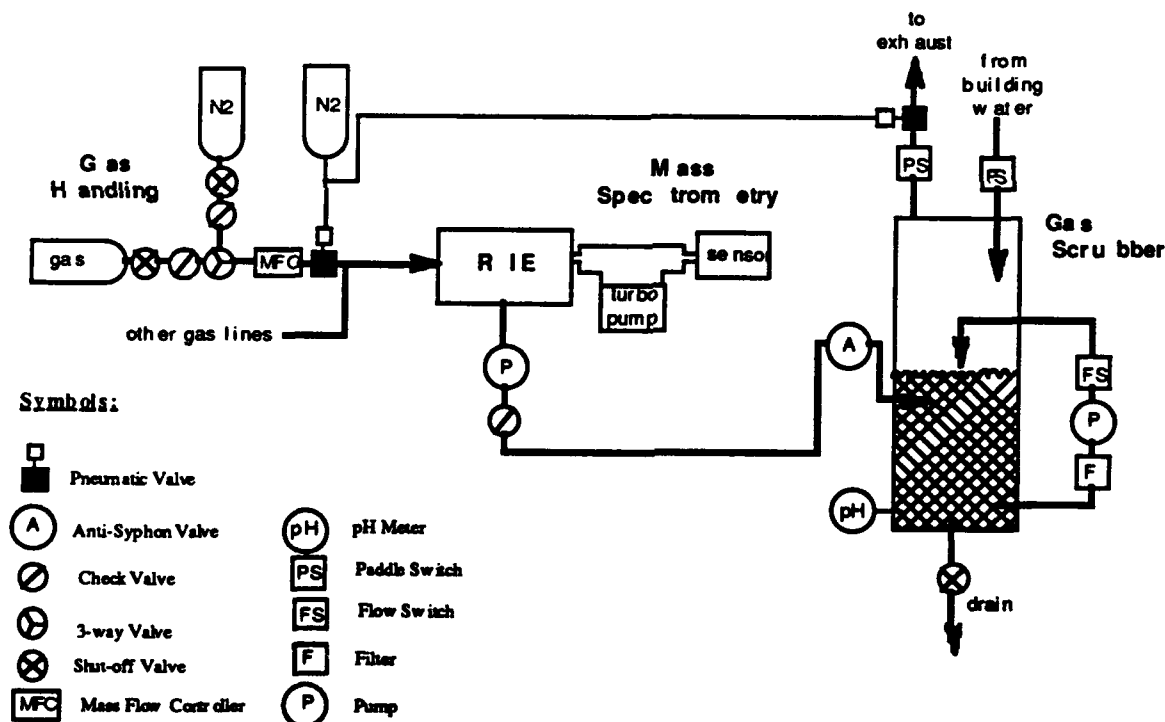
The etch rate is dependent upon several parameters including the presence of residual gases in the chamber, substrate temperature, Cl₂ flux, ion beam and the presence of carbon containing species. Impurity gases in the chamber (i.e. H₂O, O₂, N₂, etc.) can react with the aluminum films and impede the etching process by leaving a residue on the etched surface. This reduces the amount of Cl₂ available for reaction and consequently lowers the etch rate [13]. The substrate temperature is another parameter that affects the etch rate of aluminum. Efremow *et al.* [13] observed a two-fold increase in the etch rate by heating the substrate from 0° to 100°C. It was hypothesized that the increase in temperature led to a higher evaporation rate of the product AlCl₃. In addition, they found that an increase in the Cl₂ flux produced a significant amount of undercutting due to the nondirectional flow of the Cl₂ gas. A higher degree of anisotropy was achieved by the combination of ion beam and Cl₂ flux. Efremow *et al.* suggested that sidewall passivation (by reaction of H₂O with the aluminum) was partly responsible for the production of the very fine features in their samples. Submicrostructures of 80 nm wide lines were etched into a 100 nm thick aluminum film with 0.3 mTorr Cl₂ gas and 0.1 mA, 1 keV Ar⁺ beam. Lastly, Parks *et al.* [14] found that chemisorption of the halocarbon gas molecules, such as CCl₄ and CBr₄, onto the aluminum

surface formed halogenated alum-inum species along with an aluminum carbide. Therefore, a significant reduction in the etch rate was observed due to the difficulty encountered in removing the carbide from the surface.

C. Proposed Research

Experimental Apparatus. Since the date of the last report [38], the design of the RIE system has been changed in the interest of constructing a more cost-effective, reliable and safe system. Since toxic gases, such as BCl_3 and Cl_2 , may be used to etch GaN and AlN, the system is designed for safe shutdown in the event of a power or water failure and/or inadvertent shutdown of the exhaust systems in the building. The main components of the system include gas handling/storage, etcher, gas scrubber and mass spectrometer. A schematic of the RIE system is shown in Fig. 1.

Figure 1. Schematic Diagram of the Reactive Ion Etching System



The gas handling/storage sub-system consists of the gas storage cabinet(s), gas bottles, bottle regulators and necessary valves and tubing. Dry nitrogen will be used to purge the gas lines before and after every run to remove moisture and chlorine from the lines, thus reducing the probability of corrosion of the gas lines. Mass flow controllers will be employed for accurate control of the process gases. In addition, pneumatic valves will be installed as a safety precaution. In the event of a power failure, interruption of the water supply or

shutdown of the exhaust system, the solenoid actuated pneumatic valves will isolate the gas lines from the etch chamber.

The design of the etcher is based on that of the standard parallel-plate diode configuration in which the bottom electrode is powered by a RF power supply (see for example Ref. 10). The etcher, a Technics 85 series RIE, consists of an anodized aluminum chamber with an anodized aluminum water-cooled, driven lower electrode. A 350 Watt, 13.56 MHz RF generator with auto impedance matching network produces the power required to maintain a glow discharge in the chamber. Safety interlocks are supplied by Technics to disable the power when the system is vented or a panel is removed. The chamber pressure is measured by a corrosion-resistant capacitance manometer (absolute pressure) which is mounted to the underside of the chamber. The two channels of process gas (made from stainless steel tubing) are isolated from the injection manifold by means of air-operated electrically actuated isolation valves. In addition, an 11 CFM two-stage corrosive-series direct drive rotary vane pump is supplied with the etcher.

Residual process gases and reaction by-products from the etcher will pass through a wet scrubber which is equipped with water inlet and water recirculation lines. These lines are monitored by flow switches, and the exhaust line is monitored by a paddle switch. Interruption of the water flow or inadequate ventilation will trip the pneumatic valves and close the gas lines. An anti-siphon valve is incorporated into the design to ensure there is no backflow of water from the scrubber into the pump exhaust. In addition, the pH level of the scrubber water will be tested and monitored prior to waste disposal.

Lastly, a mass spectrometer may be employed in the future for the detection and characterization of chemical species produced by the etching processes. It could also be used as a kind of end-point detection device. It is further hoped that this analytical instrumentation could provide necessary information for the determination of the success of the etching processes and could provide a basis for an understanding of the etching mechanisms.

Choice of Process Gases. There are a number of process gases that can be used to produce anisotropically etched features. For GaN and AlN, fluorine plasmas are impractical because involatile fluorides are formed at the surfaces, therefore limiting desorption of reaction species from the surface [35]. Chlorine plasmas, on the other hand, have been used extensively for etching these compounds, see Section B above.

In etching GaN, the gases used by Tanaka [20], Foresi [21] and S. J. Pearton *et al.*[37] namely CCl_2F_2 , Cl_2 and BCl_3 will be employed first since those investigators reported successful results. Experimentation with other combinations of gases is likely in order to obtain anisotropic features and reasonably high etch rates. As for AlN, chlorine containing gases with additions of O_2 , carbon containing gases and or noble gases (i.e. Ar, He, etc.) are likely candidate gases. Though, somewhat of a trial and error methodology will be followed

until success is achieved. It is noted that for RIE, sidewall passivation may be an important mechanism for anisotropic etching of AlN and may produce relatively large features. On the other hand, ion beam assisted etching, or similar techniques, are likely to produce smaller features in these nitrides.

D. Future Research

Future plans include installation of the RIE system and development and characterization of suitable etching processes for aluminum and gallium nitride materials.

E. References

1. *Plasma Processing of Materials: Scientific Opportunities and Technological Challenges, Panel on Plasma Processing of Materials*, National Research Council (National Academy Press, Washington, D.C., 1991).
2. J. W. Palmour, R. F. Davis, T. M. Wallett and K. B. Bhasin, *J. Vac. Sci. Technol.*, **A4**, 590 (1986).
3. D. L. Smith, P. G. Saviano, *J. Vac. Sci. Technol.* **21**, 768 (1982).
4. D. L. Smith and R. H. Bruce, *J. Electrochem. Soc.* **129**, 2045, (1978).
5. C. J. Mogab, A. C. Adams and D. L. Flamm, *J. Appl. Phys.* **49**, 3796 (1978).
6. S. Matsuo, *J. Vac. Sci. Technol.* **17**, 587 (1980).
7. L. M. Ephrath, *Solid State Technol.*, July 1982, p. 87.
8. Y.H. Lee and M. M. Chen, *J. Appl. Phys.* **54**, 5966 (1983).
9. L. M. Ephrath, *J. Electrochem. Soc.*, August 1979, p. 1419.
10. A. J. van Roosmalen, *Vacuum* **34**, 429 (1984).
11. M. Zhang, J. Z. Li, I. Adesida and E. D. Wolf, *J. Vac. Sci. Technol.* **B1**, 1037 (1983).
12. R. H. Bruce and G. P. Malafsky, *J. Electrochem. Soc.* **136**, 1369 (1983).
13. N. N. Efremow, M. W. Geis, R. W. Mountain, G. A. Lincoln, J. N. Randall and N. P. Economou, *J. Vac. Sci. Technol.* **B4**, 337 (1986).
14. S. Park, L. C. Rathburn and T. N. Rhodin, *J. Vac. Sci. Technol.* **A3**, 791 (1985).
15. H. F. Winters, *J. Vac. Sci. Technol.* **B3**, 9 (1985).
16. D. A. Danner and D. W. Hess, *J. Appl. Phys.* **59**, 940 (1986).
17. R. J. A. A. Janssen, A. W. Kolfschoten and G. N. A. van Veen, *Appl. Phys. Lett.*, **52**, 98 (1988).
18. Y. Ochiai, K. Shihoyama, T. Shiokawa, K. Toyoda, A. Masuyama, K. Gamu, S. Namba, *J. Appl. Phys.* **25**, L527 (1986).
19. G. Smolinski, R. P. Chang and T. M. Mayer, *J. Vac. Sci. Technol.* **18**, 12 (1981).
20. H. Tanaka, *Optoelectronics - Devices and Technologies* **6**, 150 (1991).
21. J. S. Foresi, *M. S. Thesis*, Boston University, Boston, MA, 1992.
22. I. Akasaki and H. Amano, "Conductivity control of AlGaN, fabrication of AlGaN/GaN multi-heterostructure and their application to UV/Blue light emitting devices," July 1992 MRS conference.
23. C. Eddy, *Ph.D. Thesis*, Boston University, Boston, MA, 1990.
24. T. Lei and T. D. Moustakas, *J. Appl. Phys.* **71**, 4933 (1992).
25. Z. J. Yu, B.S. Sywe, A. U. Ahmed, J. H. Edger, *J. Electr. Mater.* **21**, 782 (1992).
26. J. Sumakeris, Z. Sitar, K. S. Ailey-Trent, K. L. Moore and R. F. Davis, "Layer-by-Layer Epitaxial Growth of GaN at Low Temperatures," (to be published in *Thin Solid Films*).
27. *CRC Handbook of Metal Etchants*, eds. P. Walker and W. H. Tarn (CRC Press, Boca Raton, LA, 1991).
28. E. S. Dettmer, B. M. Romenesko, H. K. Charles Jr., B. G. Carkhuff and D. J. Merrill, *IEEE Transactions - Components, Hybrids, Manuf. Technol.*, **12**, 543 (1989).

29. L. B. Rowland, Ph.D. Thesis, North Carolina State University, Raleigh, NC, 1992.
30. D. Suryanarayana, J. Am. Cer. Soc. **73**, 1108 (1990).
31. A. D. Katnani and K. I. Papathomas, J. Vac. Sci. Technol. **A5**, 1335 (1987).
32. A. Abid, R. Bensalem and B. J. Sealy, J. Mater. Sci. **21**, 1301 (1986).
33. T. Sato, K. Haryu, T. Endo and M. Shimado, J. Mater. Sci. **22**, 2277 (1987).
34. D. Suryanarayana, L. J. Matienzo and D. F. Spencer, IEEE Transactions - Components, Hybrids, Manuf. Technol. **12**, 566 (1989).
35. V. M. Donnelly and D. L. Flamm, Solid State Technol., April 1981, p. 161.
36. G. S. Oehrlein, in *Handbook of Plasma Processing Technology*, eds. S.M. Rossnagel, J. J Cuomo and W. D. Westwood, (Noyes Publications, Park Ridge, New Jersey, 1990).
37. S. J. Pearton, C. R. Abernathy, F. Ren, J. R. Lothian, P. W. Wisk, A. Katz and C. Constantine, Semiconductor Sci. Technol. **8**, 310 (1993).
38. R. F. Davis, K. S. Ailey-Trent, D. Kester, R. Patterson, W. Perry, L. Smith, C. Wang, W. Weeks, K. Webber, "Nitride Semiconductors for Ultraviolet Detection," Annual Report, December 1992, p. 44.

XVI. Distribution List

Mr. Max Yoder Office of Naval Research Electronics Division, Code: 1114SS 800 N. Quincy Street Arlington, VA 22217-5000	3
Administrative Contracting Officer Office Of Naval Research Resident Representative The Ohio State University Research Center 1960 Kenny Road Columbus, OH 43210-1063	1
Director, Naval Research Laboratory ATTN: Code 2627 Washington, DC 20375	1
Defense Technical Information Center Bldg. 5, Cameron Station Alexandria, VA 22314	2